

# LBNE Case Study Report

## 200 kt Water Cherenkov Far Detector

**v4.0**

October 20, 2011



# Contents

<b>Contents</b>	<b>i</b>
<b>1 Executive Summary</b>	<b>1</b>
<b>2 Physics Goals</b>	<b>5</b>
<b>3 Depth Requirements</b>	<b>9</b>
<b>4 Detector Reference Design</b>	<b>11</b>
4.1 Introduction . . . . .	11
4.2 Detector Elements . . . . .	11
4.3 Cavern Size and Shape . . . . .	12
4.4 Photodetectors . . . . .	17
4.5 PMT Implosion Mitigation . . . . .	22
4.6 Readout electronics . . . . .	24
4.7 Water fill, recycling, and cooling . . . . .	25
4.8 Fiducial volume definition . . . . .	26
4.9 Veto . . . . .	26
4.10 Calibrations and monitoring . . . . .	27
4.11 Overall Underground Layout and Facility Resource Requirements . . . . .	28
4.12 Conventional Facilities . . . . .	28
4.13 Installation . . . . .	32
<b>5 Experimental Approach</b>	<b>35</b>
5.1 The LBNE Beam Design and Simulation . . . . .	35
5.2 Detector Simulation . . . . .	37
5.3 Reconstruction . . . . .	38
5.3.1 Super-K based reconstruction tools . . . . .	42
5.3.2 LBNE based reconstruction tools . . . . .	43
5.3.3 Future Work . . . . .	45
5.4 Calibrations . . . . .	45
<b>6 Long-Baseline Neutrino Physics</b>	<b>49</b>
6.1 Long-Baseline $\nu_\mu \rightarrow \nu_e$ Oscillations . . . . .	50
6.1.1 Sensitivity to $\theta_{13} \neq 0$ . . . . .	51

6.1.2	$\nu_e$ Appearance if $\theta_{13} = 0$ . . . . .	52
6.1.3	Mass Hierarchy . . . . .	54
6.1.4	CP Violation . . . . .	56
6.1.5	Future Improvements . . . . .	58
6.2	Beam Upgrades . . . . .	60
6.3	$\nu_\mu$ and $\bar{\nu}_\mu$ Disappearance . . . . .	60
6.3.1	Resolving the $\theta_{23}$ Octant . . . . .	63
6.3.2	$\nu_\tau$ Appearance . . . . .	63
6.4	Neutrino Physics Beyond Standard Mixing . . . . .	65
6.4.1	Non-standard Interactions . . . . .	65
6.4.2	Long Range Lepton Flavor Interactions . . . . .	67
6.5	Variation of Physics Sensitivities with Baseline . . . . .	68
6.6	Summary of Long-Baseline Physics Capabilities . . . . .	68
<b>7</b>	<b>Proton Decay</b> . . . . .	<b>73</b>
7.1	Motivation and Scientific Impact of Future Measurements . . . . .	73
7.2	Sensitivity of Reference Configurations . . . . .	75
7.3	Proton decay to $e^+\pi^0$ . . . . .	77
7.4	Proton decay to $\nu K^+$ . . . . .	78
<b>8</b>	<b>Supernova Burst Neutrinos</b> . . . . .	<b>81</b>
8.1	Motivation and Scientific Impact of Future Measurements . . . . .	81
8.2	Supernova Neutrino Interaction Rates . . . . .	82
8.3	Mass Hierarchy Sensitivity . . . . .	84
<b>9</b>	<b>Atmospheric Neutrinos</b> . . . . .	<b>87</b>
9.1	Introduction and Physics Motivation . . . . .	87
9.1.1	Confirmatory Role . . . . .	87
9.1.2	PMNS Matrix Measurements . . . . .	88
9.2	Evaluation of Physics Sensitivities . . . . .	89
9.2.1	Method and Tools . . . . .	89
9.2.2	Physics Sensitivities . . . . .	94
9.3	Comments on Configuration Options . . . . .	94
<b>10</b>	<b>Detector Enhancements</b> . . . . .	<b>95</b>
10.1	High Coverage/Low Threshold . . . . .	95
10.2	Gadolinium Loading . . . . .	96
10.2.1	Low Energy Reconstruction and Neutron Tagging . . . . .	97
10.3	Scintillator Fill . . . . .	99
<b>11</b>	<b>Physics with Enhanced Scenarios</b> . . . . .	<b>101</b>
11.1	High PMT Coverage and Solar Day/Night . . . . .	101
11.2	Gadolinium and Supernova Bursts . . . . .	103
11.3	Gadolinium and Relic Supernova Neutrinos . . . . .	104

11.4	DAE $\delta$ ALUS . . . . .	110
11.5	Physics in a Scintillator Fill . . . . .	112
11.5.1	Proton Decay in a Scintillator Fill . . . . .	112
11.5.2	Reactor Antineutrinos . . . . .	113
11.5.3	Geoneutrinos . . . . .	114
	<b>Bibliography</b>	<b>116</b>



# 1 Executive Summary

We present here the characteristics and physics program of a fourth-generation, 200 kt water Cherenkov detector. The detector would be located underground with an overburden of 4300 meters water equivalent, and have an effective photocathode coverage of roughly the equivalent of the Super-Kamiokande II detector.

One of the biggest mysteries of the new physics of the lepton sector is why the mixing is so different than in the quark sector. While small mixing in the quark sector ‘makes sense’—the weak flavor eigenstates are nearly the same as the strong eigenstates—neutrinos are a perplexing mix of two large and one small angle. A  $\nu_3$ , for example, is nearly an equal mixture of  $\nu_\mu$  and  $\nu_\tau$ , at odds with our intuition that the hierarchy of neutrino mass eigenstates should ‘look like’ the charged flavor eigenstates. A major future goal of the neutrino program is to determine how fundamental the differences between the mixing in the quark and lepton sectors really are, and whether this can help point us toward a more complete theory of flavor.

We have therefore focused LBNE on the area of neutrino mixing that is least known. The primary physics is aimed at  $\nu_e$  appearance measurements, with the highest priority being a search for a Standard Model-like CP-violating asymmetry in the oscillation  $\nu_\mu \rightarrow \nu_e$ , with a beam originating at Fermi National Accelerator Laboratory. Other beam-related  $\nu_e$  appearance measurements include a resolution of the neutrino mass hierarchy, precision measurement of  $\theta_{13}$ , and observation of the matter effect. (These beam-related measurements can all be made at much shallower depth than 4300 m.w.e.). We anticipate that in five years of running a 700 kW beam in neutrino mode, and five years of running in antineutrino mode, we will be able to make a  $3\sigma$  discovery of CP violation, for 50% of all  $\delta_{CP}$  values, for values of  $\sin^2 2\theta_{13} > 0.03$ . If the value of  $\theta_{13}$  is below the sensitive range of experiments such as T2K, NO $\nu$ A, or the reactor antineutrino experiments such as Daya Bay, we expect in the normal hierarchy scenario to be sensitive to values of  $\sin^2 2\theta_{13} \sim 0.002 - 0.008$ , depending on the value of  $\delta_{CP}$ . For a 2 MW beam, like that discussed for Project X, we push both the 50% CP coverage point and the three sigma resolution of the mass hierarchy down to values near  $\sin^2 2\theta_{13} = 0.01$ . The  $3\sigma$  discovery point for non-zero  $\theta_{13}$  moves down to  $\sin^2 2\theta_{13} \sim 0.001 - 0.004$  in the 2 MW beam scenario.

The large mass and depth of the water Cherenkov detector will also allow a search for proton decay, which in  $e^+\pi^0$  mode would push the lifetime sensitivity to nearly  $10^{35}$  years in 10 years of running. Supernova burst neutrinos can also be observed should such an event happen during the detector's lifetime, with a total event count above threshold expected to be  $\sim 30,000$  for a supernova within a 10 kpc radius of Earth. Observation of such supernova neutrinos could also provide sensitivity to neutrino parameters: just a few thousand events are likely to be enough to distinguish the mass hierarchy at the  $3\sigma$  level. We expect a handful of events for a supernova as distant as the Andromeda galaxy.

A rich program of additional neutrino physics and astrophysics is possible with a large water Cherenkov detector located deep underground, as demonstrated by experiments like SNO and Super-Kamiokande. Remarkably, the dynamic range of the physics accessible in these detectors extends from a few MeV to hundreds of TeV. With enhancements to the detector such as increased photocathode coverage and a consequent lowering of the energy threshold, we would expect the experiment to be able to make the first  $3\sigma$  observation of the day/night asymmetry in the solar neutrino flux, a 'smoking gun' signature of the matter effect. Loading the water with a nucleus that has a high neutron capture cross section, such as Gd, could also enable an observation of the relic supernova neutrino background, and possibly allow observation of other low-energy antineutrino sources. A Gd-loaded water detector could also be used as a target for lower-energy antineutrino beams, like those that could be produced by stopped pions created by low-cost cyclotrons. Lastly, as the SNO+ experiment has shown, water Cherenkov detectors can be converted to liquid scintillator detectors allowing even lower energy neutrino measurements like the flux of geoneutrinos, or precision neutrino measurements using small modular reactors.

Table 1-1 is a partial summary of the wide-ranging physics capabilities of this detector, including the reach possible with marginal detector enhancements. The water Cherenkov detector provides a unique opportunity for an experiment with a broad physics impact that will be both scientifically compelling and internationally competitive.

The long experimental record of large water Cherenkov experiments significantly reduces the risk of both the design and the physics extraction from the detector. Members of the LBNE collaboration come from nearly every large-scale Cherenkov experiment ever built—IMB, Kamiokande, Super-Kamiokande, SNO, MiniBooNE, Auger, and ICECUBE. There are just three major challenges in constructing the 200 kt detector we envision here: the excavation and maintenance of a large cavity, ensuring the photomultiplier tube array is robust against implosion failure, and a reasonable cost.

Physics	Sensitivity	Workable Depth	Additional Requirements	Marginal Det. Cost
Beam $\nu_e$ appearance with 200 kt/700kW (2 MW), 5 + 5 years livetime				
$\theta_{13} \neq 0$	$\sin^2 2\theta_{13} > 0.007(0.004)$ $3\sigma$ , all $\delta_{CP}$	800 ft	None	0
Mass Hierarchy	$3\sigma$ resolution all $\delta_{CP}$ , for $\sin^2 2\theta_{13} > 0.04(0.01)$	800 ft	None	0
CP Violation	$3\sigma$ discovery for 50% $\delta_{CP}$ range $\sin^2 2\theta_{13} > 0.03(0.01)$	800 ft	None	0
Beam $\nu_\mu$ disappearance with 200 kt/700kW, 5 + 5 years livetime				
$\delta(\Delta m_{32}^2)$	$\leq 0.013 \times 10^{-3} \text{ eV}^2 (\nu)$ $\leq 0.015 \times 10^{-3} \text{ eV}^2 (\bar{\nu})$	800 ft	None	0
$\delta(\sin^2 2\theta_{23})$	$\leq 0.005 (\nu)$ $\leq 0.007 (\bar{\nu})$	800 ft	None	0
Non-Accelerator, 200 kt, 10 years livetime				
Proton Decay ( $e^+\pi^0$ )	$0.6 \times 10^{35}$ years	4300 ft	None	0
Supernova Bursts	30,000 events at 10 kpc	3850 ft	None	0
Solar $\nu$ Day/Night	0.5% on $A_{DN}$	4300 ft	1.5 $\times$ PMT coverage	\$50M
Supernova Bursts	IBD tagging	3850 ft	2 $\times$ PMT Coverage Gd loading	\$120M
Relic Supernova $\bar{\nu}s$	9-50 events/yr 40 event bkd	4300 ft	2 $\times$ PMT coverage Gd loading	\$120M
$\delta_{CP}$ (Daedalus [1])	$3\sigma$ discovery for 100% $\delta_{CP}$ range $\sin^2 2\theta_{13} > 0.004$	4300 ft	2 $\times$ PMT coverage Gd loading	\$120M
Proton Decay ( $K^+\bar{\nu}$ )	$1.0 \times 10^{35}$ years	4300 ft	100kt scintillator	\$100M
Geoneutrinos	3770 events/year	4300 ft	100kt scintillator 1.5 $\times$ PMT coverage	\$150M

Table 1-1: Summary of sensitivities for primary physics and for additional physics made possible with enhancements to the detector configuration. Marginal cost column refers detector enhancement costs for each physics topic (they are not additive). Additional physics such as atmospheric neutrinos are not shown. Possible cost savings by going to a shallower depth have not been evaluated or



## 2 Physics Goals

The primary physics goal of LBNE is to measure the oscillations of accelerator-generated neutrinos. Oscillations occur due to the quantum mechanical mixing between the flavor states of the neutrinos ( $e, \mu, \tau$ ) and the mass states. Although to date all experimental results are satisfactorily described by the independent mixing of two flavors, the simplest explanation for neutrino flavor transformation is to borrow the three-flavor mixing structure already seen in the quark sector. The new scenario thus adds at least seven new parameters to the Standard Model, or nine if neutrinos turn out to be Majorana particles.

The three flavor-mixing scenario for neutrinos can be described by three mixing angles ( $\theta_{12}, \theta_{23}$  and  $\theta_{13}$ ) and one CP-violating phase ( $\delta_{CP}$ ). The probability for neutrino oscillation also depends on the difference in the squares of the masses,  $\Delta m_{ij}^2 = m_i^2 - m_j^2$ ; with three neutrinos, there are two independent mass squared differences ( $\Delta m_{21}^2$  and  $\Delta m_{32}^2$ ). Oscillations of a muon neutrino beam over a long baseline can be studied to measure  $\theta_{23}, \theta_{13}, \delta_{CP}$  and  $\Delta m_{32}^2$ . In fact, all the neutrino oscillation parameters can be studied in a large water Cherenkov detector, as  $\theta_{12}$  and  $\Delta m_{21}^2$  can be explored with solar neutrinos.

The entire complement of all neutrino experiments to date has measured just four of the mixing parameters: two angles,  $\theta_{23}$  and  $\theta_{12}$ , and two mass differences,  $\Delta m_{21}^2$  and  $\Delta m_{32}^2$ . The sign of  $\Delta m_{21}^2$  is known, but not that of  $\Delta m_{32}^2$ . Limits have been placed on the third mixing angle,  $\theta_{13}$ , which is much smaller than the others, and therefore the mixing is quantitatively quite unlike the quark sector. A major future goal of the neutrino program is to determine how fundamental the differences between the mixing in the quark and lepton sectors really are, and whether this can help point us toward a more complete theory of flavor.

Observation of  $\nu_\mu \rightarrow \nu_e$  oscillations are the key to measuring  $\theta_{13}$  and determining the mass hierarchy (the sign of  $\Delta m_{32}^2$ ). The signature of CP violation is a difference in the probability for  $\nu_\mu \rightarrow \nu_e$  and  $\bar{\nu}_\mu \rightarrow \bar{\nu}_e$  transitions. The signal for  $\nu_\mu \rightarrow \nu_e$  oscillations is an excess of  $\nu_e$ -like interactions over the background expected from beam  $\nu_\mu$  and  $\nu_e$ .

The study of the disappearance of  $\nu_\mu$  probes  $\theta_{23}$  and  $|\Delta m_{32}^2|$ . Experiments suggest that  $\theta_{23}$  is very close to maximal ( $\sin^2(2\theta_{23}) > 0.92$  at 90% confidence level). A precision test of whether  $\theta_{23}$  is significantly different from maximal can also be done with LBNE.

One of the key predictions of Grand Unified Theories (GUTs) is a finite nucleon lifetime. The primary requirements for a proton decay search are detector mass and livetime. In addition, a low background rate and significant detection efficiency are desirable. There are two important modes that will be studied:  $p \rightarrow e\pi^0$  and  $p \rightarrow \nu K^+$ . These are the generic decay modes predicted by many models.

In a water Cherenkov detector, the signature for the  $e^+\pi^0$  channel is 3 electron-like rings—1 from the positron and 2 from the decay of the  $\pi^0$  into two gammas. The current limit on this decay mode set by Super-Kamiokande is  $1.2 \times 10^{34}$  years at the 90% confidence level [2,3]. The detection efficiency ( $\sim 37\%$ ) for this mode is dominated by pion absorption in the nucleus and cannot be significantly improved. An order of magnitude improvement in this mode by Super-Kamiokande, which currently has no nucleon decay candidates, can only be achieved by running Super-Kamiokande for an additional 30–40 more years. The sensitivity would be extended by a larger water Cherenkov detector at Homestake.

The  $K^+\bar{\nu}$  channel is more difficult to observe in a water Cherenkov detector, as neither of the final state particles are visible — the  $K^+$  is produced with a momentum that is below the Cherenkov threshold. The kaon decays with a lifetime 12.4 ns by  $K^+ \rightarrow \mu^+\nu_\mu$  or  $K^+ \rightarrow \pi^+\pi^0$ . When a proton bound in an oxygen atom decays, it produces a nitrogen ion in an excited state that decays about a third of the time via a detectable photon of  $\sim 6$  MeV. The signature of this decay in a water Cherenkov detector is the delayed coincidence between the proton decay tagged by the 6 MeV photon and the kaon decay. Thus the energy threshold, which depends on the photocathode coverage, must be low enough to detect the 6 MeV gamma. Super-Kamiokande used this method to set a limit of  $2.3 \times 10^{33}$  years [4]. The  $K^+\bar{\nu}$  mode could also be explored further with a detector at Homestake if adequate phototube coverage can be implemented.

A large water Cherenkov detector for LBNE would have the potential to study neutrinos from natural sources, for example:

- Supernova neutrinos — Studying the neutrinos emitted during a supernova could provide significant insight into these events. A nearby supernova would produce a large burst of neutrino events in a large-scale water Cherenkov detector, providing detailed timing and spectral information. There is a precedent for the detection of neutrinos from supernova bursts — 19 events were seen in water Cherenkov detectors (IMB and Kamiokande) from SN1987A.
- Relic supernova antineutrinos (also called the diffuse supernova neutrino background) — Since nearby supernovae are rare, identifying the antineutrinos from far away supernovae might provide the best chance to study them. The shape of the supernova relic neutrino spectrum will provide a test of the uniformity of neutrino emissions in core-collapse supernovae. Super-Kamiokande has set the best limit on the flux of supernova relic neutrinos [84], but the measurement is background limited. Reducing background

and lowering the energy threshold are key to observing these neutrinos. The Super-Kamiokande limit is very close to theoretical predictions, and thus the discovery of relic supernova neutrinos is within reach.

- Solar neutrinos—Study neutrino oscillations ( $\theta_{12}$ ,  $\Delta m_{21}^2$ ) and get a better understanding of the solar neutrino spectrum. One important goal is the search for the as yet unobserved day/night asymmetry of solar neutrinos, a signature prediction of the MSW or matter effect. Predictions based on the best-fit values of the mixing parameters (in the ‘LMA’ region) show that the asymmetry should be detectable if a measurement can be made with a statistical precision better than 1%, and a large-scale water Cherenkov detector with a low energy threshold would make this possible.
- Atmospheric neutrinos — Atmospheric neutrinos are unique among sources used to study oscillations: the oscillated flux contains neutrinos and antineutrinos of all flavors, matter effects may play a significant role, and the oscillation phenomenology plays out over several decades in energy and path length. These characteristics of the atmospheric flux make it an ideal source for studying a wide range of oscillation and mixing effects. The large size of the water Cherenkov detector aids in the study of these events, because even at very high energies the events can be contained within the detector volume.



### 3 Depth Requirements

In 2008, the LBNE science collaboration undertook a detailed study of the depth requirements for the main physics topics of interest with large detectors [5]. The topics considered were accelerator-generated neutrinos, supernovae, solar and atmospheric neutrinos, and nucleon decay. The requirement on the depth of the detector is guided by the rate of the desired signals and the rate of backgrounds from cosmic rays over a very wide range of energies from solar neutrino energies of 5 MeV to high energies in the range of hundreds of GeV.

To meet the requirements for the neutrino beam physics, a water Cherenkov detector does not need to be deeper than about 1000 meter water equivalent (mwe). The small duty cycle of beam events means that the integrated beam-gated livetime of the experiment is just 100 sec per year or so ( $10\mu\text{sec}/\text{pulse} \times 10^7$  pulses/year) and therefore the background from cosmic ray events is negligible. At 1000 mwe, the number of cosmic ray events in a 200 kt water Cherenkov detector is about equal to the number of charged current events (see Table 3-1) and can be eliminated from topological considerations (even without a full veto). At the 4850L, the number of cosmic ray events is negligible.

Table 3-1: The rate of cosmic ray muons in a 65 m height/diameter detector assuming a  $\cos^2\theta$  distribution (there will be a small correction at the deepest levels). The second column is the number of cosmic rays in 10-microsecond-long pulses for  $10^7$  pulses, corresponding to approximately one year of running, versus depth in meters-water-equivalent (mwe). The 4850L is equivalent to 4290 mwe.

Rate(Hz)	In-time cosmic/yr	Depth (mwe)
3600 Hz	360,000	265
188 Hz	18,800	880
5.0 Hz	500	2300
1.4 Hz	140	2960
0.58 Hz	58	3490
0.47 Hz	47	3620
0.16 Hz	16	4290

Table 3–2 shows the overburden required for different physics processes for the water Cherenkov detector.

Table 3–2: Depth requirements for physics measurements. The depth requirements in meters-water-equivalent (mwe) for different physics measurements. Given the average rock density of about  $2.7 \text{ t/m}^3$  at Homestake,  $1 \text{ mwe} \sim 1 \text{ ft. overburden}$ .

Physics	WCh depth
Long-Baseline Accelerator	800
$p \rightarrow e^+\pi$	$>3,000$
$p \rightarrow K^+\nu$	$>3,000$
Day/Night $^8\text{B}$ Solar	$\sim 4,300$
Supernova Burst	3,500
Relic Supernova	4,300
Atmospheric $\nu$	2,400

The rock (“Yates formation” or amphibolite) at the 4850L is extremely competent and very well suited for the excavation of large caverns. This level of the Homestake mine has access to both the Ross and Yates Shaft and other infrastructure at the 4850L. Hence the broad physics program available to the detector and practical considerations of the underground environment converge on the 4850L for the location of the water Cherenkov detector

Although it is possible to perform the neutrino beam measurements at the 1000 mwe depth, the shallower depth would lead to a narrower physics program. Given the anticipated  $> 30$  year lifetime of the experiment, the proposed depth of 4850 was chosen to maximize opportunities for non-accelerator-based measurements, with particular emphasis on minimizing background in proton decay. We feel the rich program of physics possible at the greater depth will provide many opportunities for graduate students and post-docs to engage in research that is both scientifically compelling and internationally competitive. An additional advantage of the broader program is that, even when the beam is unavailable, the detector can continue to make precision measurements of neutrinos from extra-terrestrial sources or continue the search for nucleon decay.

## 4 Detector Reference Design

### 4.1 Introduction

The LBNE collaboration is comprised of members who have spent the past few decades on the design and optimization of several different large-scale Cherenkov detectors. The LBNE water Cherenkov detector will be a fourth-generation instrument, born of a unique combination of the best ideas from the collaboration's prior experience. Our combined expertise has led us to a current reference design that optimizes mass and light collection, water purity, and careful control and measurement of systematic uncertainties, all with the restriction of reasonable cost. We anticipate that this reference design will evolve as we continue to exchange old ideas from our knowledge of prior detectors and generate new ideas specific to LBNE's physics goals.

### 4.2 Detector Elements

The LBNE water Cherenkov reference design at the Homestake mine requires a large excavated cavity in the very strong and stable Yates (or amphibolite) rock formation. The cavity will be lined with a smooth, watertight liner and then filled with extremely pure ASTM Type-1 water. About 29,000 PMTs, with additional light collectors, will detect the Cherenkov light from relativistic charged particles or gamma rays, and each will be connected via a single cable carrying both high-voltage (HV) and signal to readout electronics above the water. An extensive water-purification plant has been designed to fill the detector in about three months' time, and to repurify one volume of water in about one month. The size of a water Cherenkov detector is determined by three factors. First is the maximum transverse diameter of the cavern allowed by the rock properties and appropriate ground support. Current studies indicate this distance is 65 meters. Second is the maximum depth of the water limited by the pressure tolerance of the PMTs (and ultimately the rock properties). Finally, the maximum path length for Cherenkov light is limited by the attenuation lengths of water and by Rayleigh scattering to be  $\sim 80$ -100 m over the Cherenkov wavelength region of interest. The good uniformity of rock stress in the horizontal plane on the 4850L of the

Homestake mine leads to the current reference design of a cylindrical cavern, with a water diameter of 65 m and depth of  $\sim 80$  m. The total mass of water is 260 kt, and with a 2.0 m fiducial cut around the boundaries yields a fiducial volume of 200 kt.

### 4.3 Cavern Size and Shape

The maximum diameter of the cavern is determined by rock conditions. In 2010 the LBNE project commissioned a report from Golder Associates [6] on alternative cavern shapes as part of a value engineering exercise. The purpose was to find the cavern shape appropriate for the rock conditions at the 4850L providing the cavern with smallest surface to volume ratio. This minimizes the cost of the PMTs, which are the dominant cost driver of the WCD technical components. Several cavern shapes were considered, and the result of the report was that given the roughly equal stresses in the horizontal plane a right circular cylinder was the best shape. Their analysis included the known properties of the rock and its environment from mapping of the existing drifts and analysis of cores from bore holes drilled as part of the geotech investigation for DUSEL. The report concluded: a “domed, upright, cylindrical caverns are feasible up to spans of about 217 ft (66 m).” They further conclude that no additional ‘special’ costs are incurred going from a 100kt to a 300kt cavity (the costs scale linearly), indicating that even at 300kt, there is no need for the development of new ground support techniques.

The Golder report and the plans therein were further reviewed by the DUSEL Large Cavity Advisory Board (LCAB) in April 2011, whose members are Evert Hoek, Ed Cording, and Derek Martin. They make the following points in their executive summary:

- A combination of favorable rock mass strength and structural conditions and an in situ stress field that is reasonably benign means that a stable 65 m diameter 102 m high vertical cylindrical cavern can be constructed at the selected location on the 4850 level of the Homestake mine.
- The hemispherical shape of the cavern dome and the cylindrical shape of the main body of the cavern are both close to optimum in terms of inducing a stress field that will support potentially unstable wedges while, at the same time, not overstress the intact rock surrounding the cavern. The chosen cavern shape has significant advantages compared to alternative cavern shapes, such as a letter-box cavern, since it avoids the formation of tensile stress regions and deep zones of low confining pressures in large planar walls.
- The increased size of the 200 Kt cavern, compared to the 100 Kt cavern considered to date, means that access for construction of the dome can be provided by a simple ramp from the 4850 level. Consequently, the halo drift proposed for the 100 Kt cavern is no longer required.

- While the combination of cavern size and depth below surface of the 200 Kt WCD is beyond precedent, the factors that control the stability of the cavern are well within our experience and technical knowledge base. It has been demonstrated that structurally controlled gravity-driven wedge instability can be controlled by a carefully designed excavation sequence and the installation of grouted rockbolts and cables as was done in the Norwegian Ice Hockey cavern. In fact, the Norwegian cavern has approximately the same width as the 200Kt WCD, but its letterbox configuration is a more severe geometry that can produce larger wedges than the axisymmetric configuration of the WCD. It has also been demonstrated that adverse in situ stress conditions giving rise to spalling and even rockbursting can also be controlled by carefully designed excavation and support installation methods such as those used for the Sudbury Neutrino Observatory cavern. Even though the WCD is located at significant depth, the rock strength is sufficient so that stress-induced spalling will be limited and rock bursting will not develop, as demonstrated by both analyses and the extensive experience in mining and driving drifts at the 4850 level.
- Based on analyses of rock strength, in situ stresses, and structural features mapped and laser scanned in existing excavations on the 4850 level, it has been concluded that a pattern of 15 m long 50 ton capacity cables on a 2.5 x 2.5 m grid would provide adequate support for any potential gravity driven wedge failures in the rock mass surrounding the 200 Kt WCD cavern. Untensioned grouted rockbolts of 5 m length and spaced on a 2.5 x 2.5 m grid, centered on the midpoints of the cable pattern, and a layer of shotcrete installed close to the advancing excavation front would provide support for small-scale wedges and breakouts and limit loosening of the rock near the excavation surface. It is possible that a reduction of both cable length and capacity of the cables may be achieved by further optimization studies and further exploration at the selected cavern site. However, it is recommended that the sizes and capacities listed above be used in present cost estimates.
- The LCAB recommends that the double corrosion protection system that has been proposed for the cavern designs considered to date should be eliminated and that standard cement grout installation procedures should be used. These procedures were used for both the 62 m span Norwegian Ice Hockey cavern and the 2070 m deep Sudbury Neutrino Observatory cavern and have been used for many of the large underground powerhouse caverns constructed and operating over the past 50 years.

There is clearly value in making the cavity as large as possible up to the constraints given by rock mechanics, light attenuation in water and PMT mechanical stability under pressure, since the surface to volume ratio is a major cost driver. A 65 m diameter cavity is technically feasible and would allow a scientifically compelling and internationally competitive experiment to be launched at DUSEL in a single cavity.

Based on these analyses, the reference design for the 200kt LBNE water Cherenkov detector is a cavern with a free diameter of 65 m.

The two other drivers for the cavern dimensions are the maximum working pressure for the PMTs under water and the attenuation and scattering of light. Table 4-1 lists physics and safety requirements for the water Cherenkov detector. Various design specifications and the dimensions of the chamber are shown in Table 4-2. For our reference design, LBNE has assumed a technically feasible 65 m diameter excavation as shown in Figures 4-1 and 4-2.

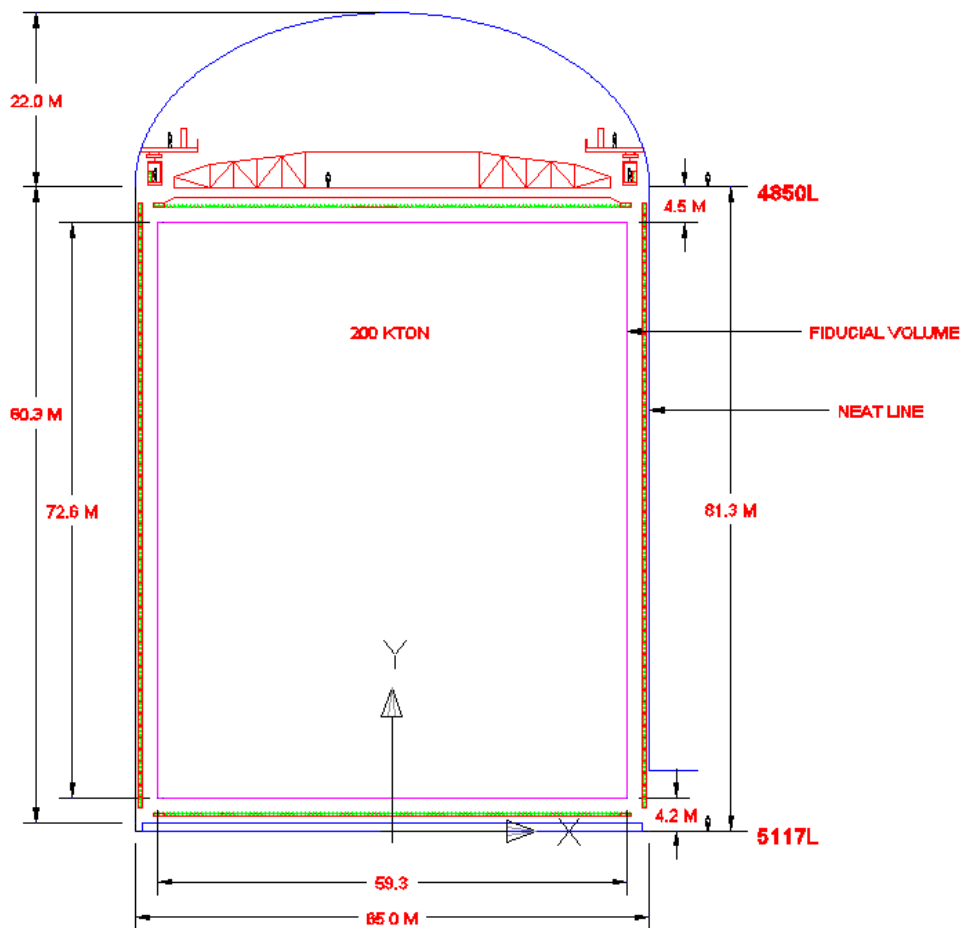


Figure 4-1: Cross-sectional view of 200 kt cavity, with dimensions labelled.

Once the cavern is excavated, it must be prepared to hold water, divert native water in a systematic way so it can be collected without pressure buildup, and anticipate and collect leaks from the detector volume. The main function of the watertight liner is to provide an absolute barrier between the highly purified water (ASTM Type 1, ultra purified water) in the detector and any underground water that might seep into the excavations. We have selected a liner attached directly to the shotcrete selected for the case study as it maximizes the fiducial

Table 4-1: List of requirements for the water Cherenkov detector

Item	Value	Reason
Fiducial volume of WCh detector	200 kt	Neutrino oscillation parameter measurement, proton decay
Maximum distance between cavities perpendicular to neutrino beam	5 km	Neutrino beam opening angle
Maximum depth of water above lowest PMT	~100 m	PMT collapse under water pressure
Depth of cavity below surface	4850L	Cosmogenic background to proton decay
Maximum distance between any two PMTs	80-100 m	Water attenuation length at peak PMT wavelength sensitivity when convolved with Cherenkov light spectrum
FV cut	2 m	from PMT photocathode, top bottom and sides Cosmic ray rejection
Cavity lifetime	$\geq 30$ years	Proton decay, neutrino oscillation parameter measurement
Egress (From all drifts and cavities during all phases of construction and operation)	Dual egress	Personnel safety
Water temperature	$13\text{ }^{\circ}\text{C} \pm 2^{\circ}\text{C}$	Reduce biological growth
Temperature	$22^{\circ}\text{C} \pm 4^{\circ}\text{C}$	Standard ventilation air temperature
Humidity of dome air	$40\% \pm 10\%$ RH.	Standard ventilation air temperature
Code requirements	TBD	Personnel, equipment, or facility safety

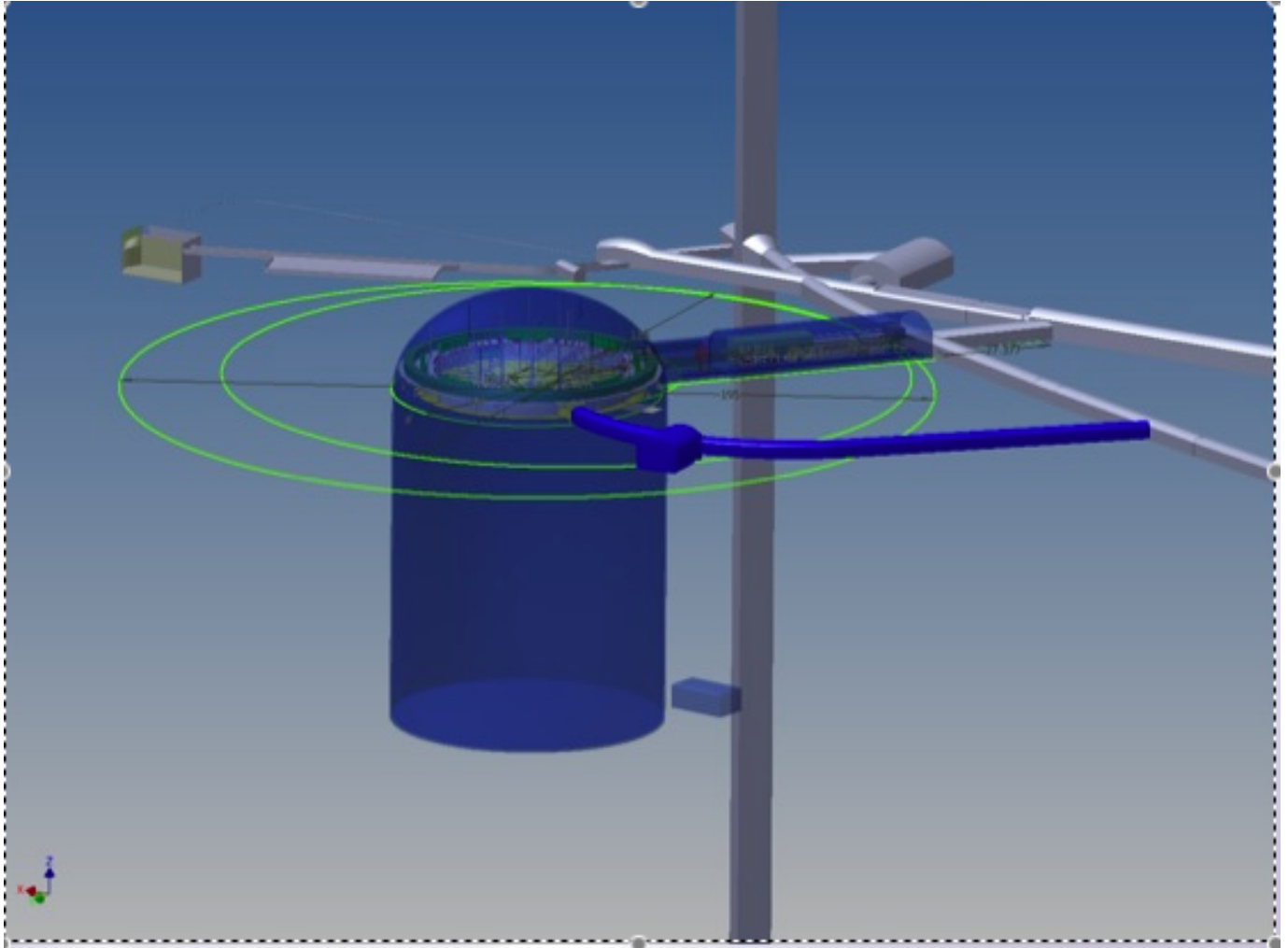


Figure 4-2: Illustration of the full complex for the 200kt water Cherenkov detector at the 4850L, showing the detector itself, the utility drift containing the water repurification plant, electrical systems and other infrastructure, and the secondary access drift from the 4850L. The Davis chamber, Majorana transition cavity, Yates shaft and an area of refuge are visible in the background.

Table 4-2: Water Cherenkov Cavern Physics Specification

Item	Specification
Shape	An unobstructed right cylindrical volume free of rock outcroppings or ground support
Free diameter	65 m (maximum allowed by geotech analysis of rock conditions)
Top of right cylindrical	Level with the 4850L
Free height from (possibly virtual) flat floor to 4850L	81.3m*
Fiducial volume dimensions	59.3 m diameter by 72.8 m high, 200 kt FV
Lifetime	$\geq 30$ years
Water temperature	$13^{\circ}\text{C} \pm 2^{\circ}\text{C}$
Dome air temperature, relative humidity	$22^{\circ}\text{C} \pm 4^{\circ}\text{C}$ , $40\% \pm 10\%$ RH

volume for a constant excavation size, and is cheaper to build. Magnetic ‘compensation’ coils will be embedded in the wall to partially cancel the Earth’s magnetic field, thus improving PMT efficiency and charge response.

## 4.4 Photodetectors

The photomultiplier tubes (PMTs) are the only active element in the water Cherenkov detector, and as such they have a direct impact on the physics reach of the experiment. The total number of photons detected, their times of arrival, and the angular positions relative to a hypothesized Cherenkov cone (or cones) determine the detector’s energy and position resolution, its efficiency for particle identification and ultimately background rejection. We have been examining PMTs made by two vendors: Hamamatsu Corporation, and ADIT/ETL. For our reference design, we have selected 12” photomultiplier tubes with high quantum efficiency (HQE) photocathodes, that are being developed by Hamamatsu Corporation. Figure 4-3 is a photograph of a sample 12” PMT, with a standard efficiency photocathode.

Several studies [8,9,2], have shown that the photodetection efficiency of Super-Kamiokande II, in which roughly half of the PMTs had been removed, is capable of providing the necessary reconstruction and particle identification to achieve the LBNE accelerator physics, supernova burst, and proton decay physics goals. Scaling from the Super-K II coverage to the

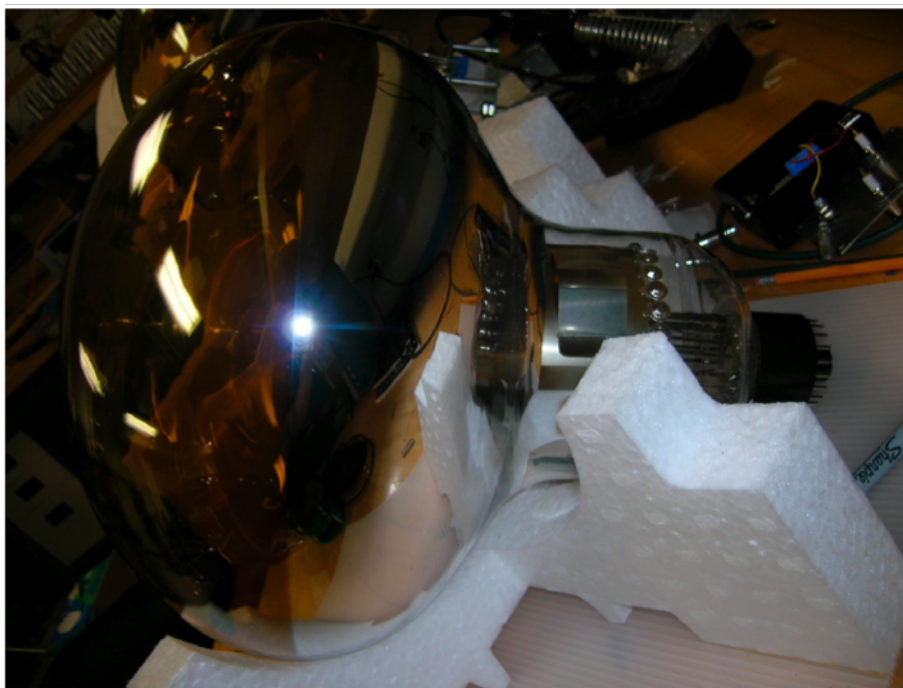


Figure 4-3: Hamamatsu R11781 12" PMT, designed for LBNE.

needed coverage for the LBNE water Cherenkov detector requires a knowledge of the relative active areas of the Super-K 20" PMTs, the relative quantum efficiency as a function of wavelength of the Super-K and LBNE PMTs, the wavelength spectrum of Cherenkov light and the optical properties (attenuation lengths) of the water.

We have recently received newly-developed high quantum efficiency 12" PMTs from Hamamatsu, and tests of these tubes will be starting very soon. We have already made direct comparisons using a Cherenkov source between a Super-K 20" PMT and a 10" high quantum efficiency PMT produced by Hamamatsu, and found that the scaling between the two was roughly what we would expect based on a direct comparison of Hamamatsu's published quantum efficiency curves for the two PMTs. We have also compared 10" HQE PMTs with 12" standard quantum efficiency PMTs, illuminated simultaneously by the same Cherenkov source, and also find that the scaling between them agrees with the expected differences in quantum efficiency and PMT area. Hamamatsu has previously provided 'enhanced quantum efficiency' (EQE) versions of the 12" PMTs, and our initial tests of these tubes show that they have quantum efficiencies as much as 35% higher than the standard 12" PMTs, for about a  $\sim 29\%$  absolute quantum efficiency.

The agreement to date between our measurements and Hamamatsu's claimed efficiencies gives us confidence that their published efficiency curves are generally correct, and we have used them to write a simple parameterized simulation that distributes event vertices

throughout the 200 kt detector volume, produces Cherenkov light and propagates the photons through the optical transmission of the water. For this simulation, we have conservatively assumed that the newly received HQE PMTs from Hamamatsu will not achieve the same 34% quantum efficiency as the 10" PMTs, but that they will be no better than 30%. We have run the same simulation for Super-K 20" PMTs and 12" HQE tubes, and as shown in Figure 4-4 find that to provide equivalent photodetection efficiency as Super-K II we would need roughly 37,000 12" HQE PMTs, without any additional light collection such as Winston cones. We have checked the parameterized simulation against the complete hit-level simulation ('WCSim'), described in Section 5.2 developed for LBNE for the 10" HQE case, and find very good agreement.

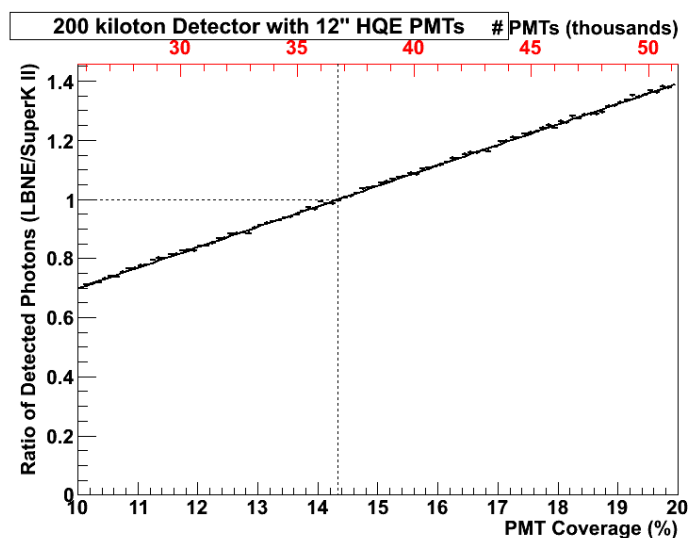


Figure 4-4: Number of 12" HQE PMTs needed to provide the same number of  $\text{pe}/\text{MeV}$  as Super-K II. This does not include any additional enhancement from light collectors, and assumes that the quantum efficiency of the 12" tubes is slightly below that of the off-the-shelf 10" HQE PMTs.

To further reduce the number of PMTs and thus reduce overall costs, our reference design assumes that some kind of light enhancement will be used: either reflective Winston concentrators like those used for SNO, or wavelength-shifter plates like those used in IMB, or a combination of the two. While SNO achieved roughly a 50% improvement in light collection with the Winston cones, we conservatively assume that any LBNE light collection will have roughly a 40% improvement. We have made measurements with several LBNE-designed reflective Winston cone light collectors, and found that for a standard shape we do, indeed, see roughly a 40% light collection improvement, and for a 'wide' Winston cone we see as much as a factor of three improvement, albeit with some degradation to the width of the prompt time peak (which moves from about 1.4 ns to 1.7 ns). With the therefore conservative assumption of a 40% improvement from light collectors, the total number of 12" HQE PMTs that will be needed for the LBNE 200 kt detector is 29,000. We note that

given the small statistics to date in our comparisons, and the tube-to-tube variations in real PMTs, that this number currently has an uncertainty associated with it of 10-15%. As we test more PMTs and more fully develop the PMT model in our simulation, we will reduce the uncertainty.

We have been pursuing an intense R&D effort on the photomultiplier tubes, examining their charge and timing characteristics, behavior in various magnetic fields, and the collection efficiency and mean photoelectron transit time across the face of the PMT. Figure 4-5 shows the single-photoelectron charge and timing spectra for a 12" 'enhanced' quantum efficiency

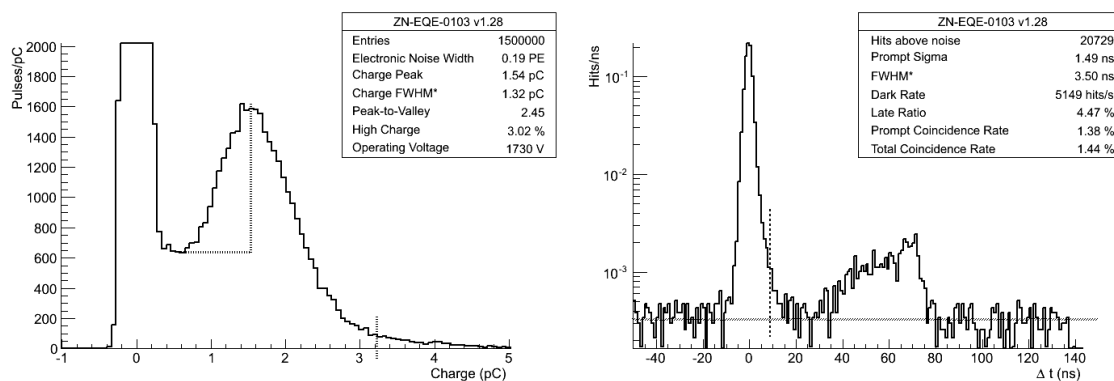


Figure 4-5: Single photoelectron charge (left) and transit time (right) distributions, measured using a Cherenkov source, for a 12" 'enhanced' quantum efficiency PMT.

PMT, and we see that overall its performance is excellent. In Figure 4-6 we show scans across the face of a 12" PMT using a Cherenkov source placed at normal incidence, measuring the

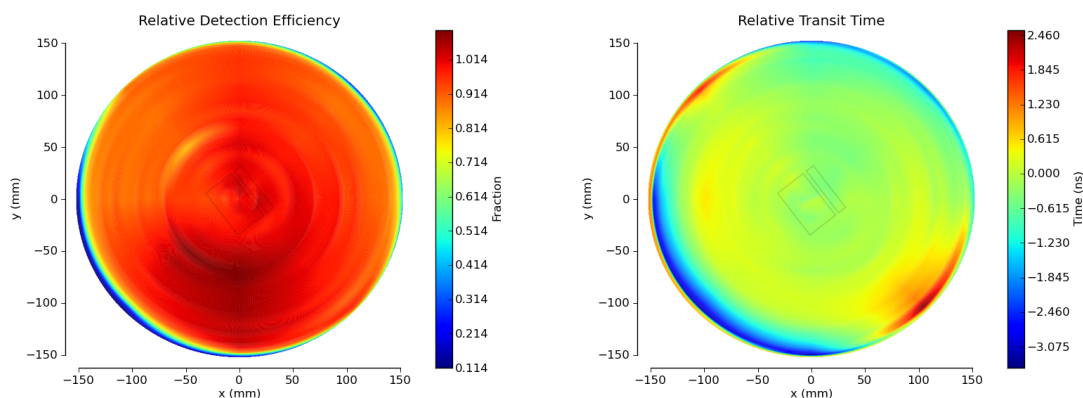


Figure 4-6: PMT collection efficiency measured (left) and mean transit time (right) measured relative to the center of the tube, for a standard quantum efficiency 12" PMT, measured using a Cherenkov source at normal incidence to the tube scanned over its face.

efficiency as a function of position relative to the center, and the mean transit time relative to the center. While we see that the efficiency looks reasonably flat across the PMT, out to nearly the full 12" diameter, the mean transit time does show large shifts near the edge. We have presented these results to the manufacturer (Hamamatsu) who confirmed the timing shifts with their own electron optics simulation, and are looking in to ways of compensating for it.

The most attractive approach for mounting the PMTs within the cavity is to use a vertical string, and lower this string into the detector volume from a work area supported from the deck, see Figure 4-7. The typical number of tubes per string is  $\sim 90$ . The tube mount takes into account both empty and filled conditions of the cavern, and the design avoids torques on the tube due to the buoyancy of the spherical section or the long power/signal cable at the end of the tube. It also should allow the installation of additional PMTs relatively easily, if funding becomes available and the physics case is strong.

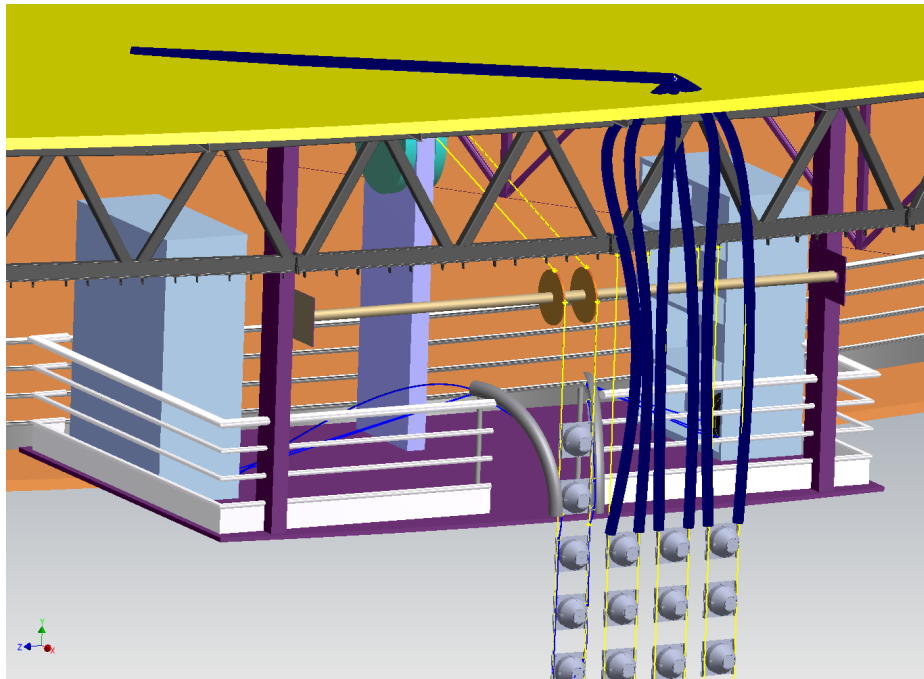


Figure 4-7: Stage for deploying PMT strings and lowering them into the detector. In this figure, there are three vertical strings of PMTs that have already been installed, and a fourth string under installation. The PMTs, their enclosure and cable spool are delivered to the working platform as a single unit. The PMT and enclosure are attached to the support cables (yellow), and the PMT signal cable and its spool (blue lines) is placed on a shelf with custom rollers. The string is lowered by one unit, and the next PMT assembly is installed. PMT string ends are supported from the ring truss at the bottom perimeter of the cavern, and the PMT signal cables are routed to the deck (heavy dark blue lines). The cable penetration enclosures are not shown.

The procurement schedule for the PMTs is such that some fraction of them will have to be stored for a few years or more. SNO PMTs that have been stored in air for over two decades have been found to perform within specification, and we do not think any special handling will be needed for the three years of storage of LBNE PMTs. Nevertheless, we will include a program of long-term testing and helium immersion as soon as production-quality PMTs are available, to get an early idea of whether anything needs to be done to ensure the tubes do not degrade in any way before they are submersed in water.

Our initial requests for production schedules from Hamamatsu were for 100,000 PMTs, and they provided a schedule for delivery of these PMTs. Our numbers now are below 1/3 of that, and therefore we see no reason why demand for large-area PMTs by other experiments would affect our delivery schedule. In fact, if other experiments were moving ahead and chose the same PMT model, the costs would likely go down and provide an opportunity for LBNE to have larger coverage for the same total PMT cost. In addition, as stated above, we are also pursuing another vendor (ADIT/ETL) who is working on an 11” PMT that would suit our needs.

## 4.5 PMT Implosion Mitigation

The larger-sized cavity envisioned for LBNE makes minimization of the risk of PMT implosion a high priority. As is well known, the largest water Cherenkov detector built to date—Super-Kamiokande—suffered a catastrophic failure of PMTs, after a period of maintenance on the detector. Subsequent mitigation of this problem by Super-Kamiokande was done by adding acrylic shields to prevent the propagation of an implosion to other tubes, but to date no new tubes have been known to implode. It is the danger of propagation—not the failure of a single tube—that is the critical issue. We have been investigating a number of approaches to mitigate the problem for LBNE, ranging from total tube enclosure, encasement in a shock-wave-dampening shield, to a shock-wave deflector between tubes. We have therefore begun very detailed shock-wave measurements of PMT implosions at the Naval Underwater Weapons Research Lab, and have been developing numerical studies using industrial software, and comparing the simulation results to our measurements. We plan on doing these tests for all potential PMT types from both vendors.

For the reference design described in this case study, the maximum pressure exerted by water on the PMT will be approximately 80 m of water or 7.8 bar. The two alternatives for PMT placement in water are: The electronic high voltage base for the PMT can be encapsulated to be water-tight and the PMT placed so that the glass bulb of the PMT is in contact with the water and is subject to the full static load (PMT in contact with water). As an alternative, the PMT can be completely encased in a pressure housing that does not allow the water to be in contact with the glass and the PMT is not subjected to the full static load (PMT in pressure vessel). Our current preferred alternative is to place the PMTs in contact with water because this minimizes the cost, maximizes the light gathering capacity,

and simplifies the eventual in-situ determination of PMT optical properties.

The first phase of our shock-wave program was completed in December 2010. To date, our work includes:

- Pressure tests of ten Hamamatsu 10-inch R7081 tubes, in which none imploded below a pressure of 10 bar. Examination of the failure modes of the six bare tubes indicates that base encapsulation of the tubes should protect the base of the tubes; this observation was confirmed by our own and vendor's simulation. Nevertheless we have found by simulation that the bulb design of the 10 inch tube is not optimized and tests of the 4 encapsulated R7081 tubes show a failure point on the dome where the shape is not spherical. The 12" tubes with new design are expected to have better performance. This has been confirmed by a single test that showed no failure up to 20 bars of pressure. More statistics on this design are planned both in our own labs and at the vendor. We also plan similar pressure testing on optimized bulb design from ETL. 30 HPK 12" bulbs, and 10 11" ETL bulbs are planned to be tested by December 2011.
- We have received samples of crushed glass specially formulated for underwater PMTs from both vendors. This glass is under examination by our collaborators at Alfred University to understand the surface stress corrosion in the ultra-pure water environment. With this work we will be able to understand the performance of the glass over the 30-year lifetime using techniques that mimic the aging process. The accelerated aging techniques developed by Alfred University colleagues will either follow the same protocol as ISO-720 or will be a standardized protocol developed at PNNL for long lifetime testing of glass.
- We have refurbished a 15-meter diameter pressure chamber (Propulsion Noise Test System) at the Naval Undersea Warfare Center (NUWC) in Rhode Island. The chamber can be pressurized up to 7 bar as currently configured. This chamber was chosen because it is large enough to produce the expected shock wave after implosion with no disturbance from wall reflections for at least 10 milliseconds. We have performed two implosion tests of 10" R7081 tubes with encapsulated bases, recording visual data with high-speed video as well as the pressure and shock wave field using shock sensors and accelerometers. These events were also simulated using the industrial hydrodynamic code LS-DYNA. The simulations are in agreement with data within 5% for the time scale of the event and within 20% for the amplitude of the shock wave. A second campaign of testing is planned for October 2011 when we will be testing the response of several PMTs to an initiated implosion using prototype mitigation schemes.

We have obtained mechanical samples of the new 12-inch Hamamatsu PMT design. We have received 11-inch PMT test samples from ADIT/ETL. In the second phase of our program we will place complete PMT assemblies in a new controlled slow rise pressure chamber at BNL and examine the static load performance of the assemblies to a maximum

pressure of 15.5 bar. In the second phase we expect to obtain low statistics data that can be used for evaluation of the static performance for the long term with the help of Alfred University. Lastly, we are now confident that the dynamic simulation models using LS-DYNA are highly predictive and therefore the initial design for the PMT assembly and support structure will be based on these numerical simulations. After the simulations, we will perform full-scale implosion testing at the NUWC facility to understand coupled implosion failures. Before CD2, we expect to make decisions regarding housing for the PMT (in contact with water or in a pressure housing) and have a good understanding of the long term performance of the tube assemblies at pressure.

## 4.6 Readout electronics

There are two possible approaches to the readout electronics. One is to locate electronics for batches of tubes (e.g., 16 tubes per batch) underwater, adjacent to the tubes. This reduces the cable length between tube and readout electronics but makes access to the electronics and maintenance extremely difficult. The other approach is to locate the electronics on a deck directly above the water detector and link each tube to the electronics with a cable. To minimize total cable length, and the associated costs including storage and installation, we have opted for four different cable lengths. Any up/down asymmetry caused by these will have to be understood through the calibration program. The electronics is planned to capture only the time (resolution 0.1 nsec) and total charge (0.2 photo electron threshold and  $\sim 14$  bit dynamic range) of each PMT hit, and time of the PMT pulse above threshold. Complete pulse shape information (i.e. using waveform digitizers) is not needed for any of the physics goals, from the high priority topics of neutrino oscillation physics and proton decay to other measurements involving extraterrestrial neutrinos. The reference design assumes the detector will be hardware-triggered—that is, the trigger will be based on a multiplicity of PMTs firing in coincidence. Super-Kamiokande, however, has successfully implemented a software trigger that counts detected hits and reduces the data set on that basis, and this is a possibility for LBNE as well. Some combination is also possible: a very loose Level 1 hardware trigger, and an on-line or ‘near-line’ software Level 2 trigger.

The burst capabilities of the electronics can easily be made large enough to handle even a nearby supernova explosion. The SNO electronics could burst-trigger at rates up to 2.5 MHz and the buffers held up to  $\sim 10000$  supernova-sized events at the front end (or a million events at the trigger level) assuming no readout at all. Were a star as close as Betelgeuse (about 200 pc) to undergo supernova explosion, this would create as many as 75 million events in a 200 kt water detector, over about 30 seconds. While the highest rate of neutrino emission occurs during the ‘breakout’ or ‘neutronization’ burst, which typically lasts 4 ms, these are primarily  $\nu_e$ s and therefore interact in a light water detector only via the small elastic scattering cross section. The  $\bar{\nu}_e$ s arrive more slowly, and thus their rate over the 30 s in this scenario is roughly 2.5 MHz, already the capabilities SNO had with electronics built nearly 15 years ago. As for storage, these events will typically have roughly 50 PMTs

hit (depending on the PMT coverage) and, for three measured variables from each hit (time, charge, and time-over-threshold) digitized at 12 bits, we would need a total of 16 GBytes for this very extreme case. A hardware buffer this large is not unreasonable—roughly the equivalent of 8 common desktop PCs.

## 4.7 Water fill, recycling, and cooling

The surface-water processing system has been designed to purify about 1,000 liters/minute of fill water, resulting in a total fill time of several months. An adequate supply of industrial water at Homestake is available to fill the detector on this time scale. In addition, the system will recycle the detector water through a repurification system at a rate about five times higher. Figure 4–8 shows a 3D-CAD isometric drawing of the repurification plant located on the 4850L near the detector. The purification requirements for this detector are within the normal range of commercial systems and are similar to those of previous water Cherenkov detectors.

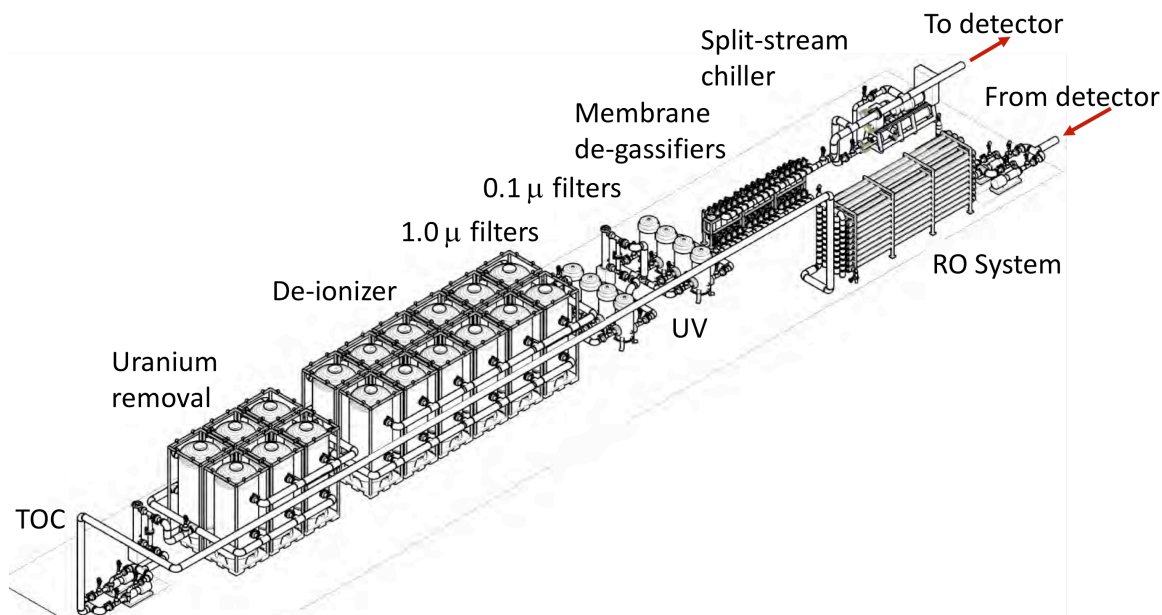


Figure 4–8: Drawing of 4500 lpm water recirculation system

The planned temperature of the water is about 13° C. This will reduce the photomultiplier dark rates and inhibit biological growth in the detector. This water temperature requires both that the initial fill water be cooled from its surface temperature and that the recycled water be cooled to remove the thermal energy due to heat flow from the rock and heat input from the photomultiplier bases. The internal rock temperature prior to excavation at the 4850L is about 33°C. As the excavation proceeds and increasing cavity surface

area is exposed to air, the near-surface rock will cool with the surface rock approaching the ventilation air temperature. Reasonable estimates are that by the time the detector is filled with water, the heat flow from the rock will be between 50 and 100 kW (no special insulation layer is needed). The photomultiplier bases are likely to add another 3 kW to this heat flow (see Table 4-3). If left uninsulated, a significant heat flow into the detector will come through the top surface from the room air contact. Insulation at this surface will be necessary.

Table 4-3: Temperatures and thermal flux in the water Cherenkov reference design. Adding insulation on the deck at the 4850L can significantly reduce the thermal load on the water-cooling system.

Item	Value
Ambient rock temperature	33.4°C at 4850L
Water temperature	13°C ± 2°C
Heat influx from rock	77 kW
Heat influx from PMTs (29k @ 100mW each)	3kW
Heat influx from dome (no insulation)	46 kW
Estimated total heat inflow	~126 kW

## 4.8 Fiducial volume definition

The photomultiplier-tube-mounting structure will include a black plastic shield at the equatorial plane of the photomultiplier tubes, that is, at the largest diameter of these tubes. This light barrier will separate any Cherenkov light generated in the outer annular region of the detector from light that is generated in the central detector cylinder. The present plan is to then define the fiducial-volume limit to be 2 meters radially inward from this light barrier. Since this is a software definition, it can be dynamically varied once the detector is in operation and events are being reconstructed. It is obviously possible to define different fiducial volumes for different signals.

## 4.9 Veto

Although the cosmic-ray-muon flux is very low at the depth of this detector, about four muons per day per m<sup>2</sup>, the large aperture of each module, about 3300 m<sup>2</sup>, will still result in a significant muon flux through the detector (approximately 0.16 Hz). At the depth of this detector array, the muons are very peaked in the vertical direction. Thus, a veto counter in

the water placed directly above the top set of photomultiplier tubes and directly beneath the top deck of the detector can tag a significant fraction of the incident high-energy cosmic-ray muons.

A black plastic sheet separates the active volume of the water forward of the PMTs from the annular volume near the cavern wall. This will prevent reflections from structures supported by the cavern wall from creating false signals in the detector. This annular volume behind the PMTs is being considered as 'thin veto' for cosmic rays or through going particles. We are studying whether this would allow using more of the fiducial volume for the long-baseline physics by allowing us to tag muons created in the surrounding rock by the neutrino beam, versus those that are fully contained in the detector.

## 4.10 Calibrations and monitoring

Water Cherenkov detectors are typically calibrated by a variety of 'sources', which can range from optical (e.g., diffuse 'laserballs', LEDs) to low-energy radioactive (e.g.,  $^{16}\text{N}$ ) to linear accelerators. Naturally occurring events that are easily tagged (through-going muons, Michel electrons) can also be used. The goals are to measure detector parameters, determine necessary corrections to things like PMT timing, and to test the detector model and the performance of reconstruction and particle ID. The design of the cavern deck includes several access ports for precisely lowering sources into the detector volume.

Detector performance characteristics such as energy scale and linearity, energy resolution, directional dependencies of energy scale and resolution, and the stability of the energy calibrations must all be well understood in order to achieve the physics goals. The goal for energy scale uncertainty is 2% or better in all energy regions (MeV to GeV), a level already exceeded by existing water Cherenkov experiments. The energy calibration can be accomplished by a combination of naturally occurring events inside the detector as well as dedicated sources deployed at various locations inside the detector volume. Cosmic muons can be used in the energy range of hundreds of MeV to several GeV. For low-energy calibration, radioactive gamma and beta sources, a low-energy linac (5-16 MeV) as well as Michel electrons can be used as sources. While not part of our costing at this point, we have also been examining the possibilities of a small, higher-energy accelerator that would allow us to test the detector's response up to energies near 1 GeV.

A centrally located LED diffuser ball will be used for timing and charge calibration. The PMT timing should be calibrated to better than 1 ns over a pulse height range of 1-1000 photoelectron (PE). After charge calibration, the uncertainty in number of PE in each PMT over the range of 1-1000 PE should be  $< 10\%$ . The water transparency needs to be continuously monitored. An attenuation length of 100 m or more must be measured to 5-10%. Muons or LEDs inside the detector could be used. Alternatively, the attenuation length could be measured for samples of water in an external system, specially designed or

commercially available. Other environmental variables that will require monitoring include water temperature, the flow rate and pattern of water circulation, water level, pH, resistivity, total dissolved solids, radon, magnetic fields, and biologics.

## 4.11 Overall Underground Layout and Facility Resource Requirements

Figure 4-9 shows a plan view of the 4850L and 5060L large cavity and related spaces. Explicit space has been provided to accommodate the water-purification plant, including maintenance considerations. Apart from the large cavity (LC), there is about 5170 m<sup>2</sup> of other space on the 4850L related to LBNE activities, not including the mucking or drifts for geotechnical investigation. Figure 4-10 is an isometric view of the dome area, showing the cable penetrations and electronics racks and magnetic compensation for the Earth's magnetic field. The magnetic field compensation maximizes the PMT efficiency and also reduces the asymmetries in the detector efficiency. If the Earth's field is not compensated, there is a 10-15% efficiency loss per PMT.

The utility drift holds the electrical room for the large cavity and the water purification system. The control room, room for calibration equipment and other storage are located on the deck. The occupancy in the lab is expected to vary from a peak of ~ 50 during the most intense installation activity to just 1 or 2 during normal operations. Not shown in the diagram is a radon-abatement system (or LN<sub>2</sub> plant) for suppressing radon between the deck and the water. (Experience has shown that Radon abatement outside the tank is not necessary). On the 5060L, sumps are needed to collect native and detector water, and pumps to recirculate the water to the purification system. In the event Gd is added to the water, there will be a small Gd recovery plant at this level to remove Gd from water leaking from the detector volume. Table 4-4 lists the facilities requirements for the water Cherenkov detector.

## 4.12 Conventional Facilities

The conventional facilities portion of the LBNE Water Cherenkov Detector sub-project must provide a cost-effective total solution that meets the requirements for each phase of the project: the excavation of the Large Cavity, construction of the vessel, liner and deck, installation of detector components, and detector operation. The surface conventional facilities include all necessary space and infrastructure from accommodation of excavation workers to the supply of water and electrical power for the experiment. Underground facilities for the WCD project require consideration of everything from the shaft cage and rock skipping capacity to occupancy requirements for areas of refuge through detector operation. Methods

Table 4-4: Facilities requirements for the water Cherenkov detector.

Layout		
Requirement	Value/Description	Comment/Justification
Depth	4850	at deck top, base at 5117L
Footprint [m <sup>2</sup> ]	3316	without utility or H2O purification areas
Max. Height [m] above 4850L	22	Top of dome at 86 m, springline at 81.3 m
Deck Weight (metric tons=1000 kg)	590	
Total Surface area [m <sup>2</sup> ]	3181	
Utilities		
Underground Power [kW]	933	Does not include surface power requirements.
Emergency Power [kW]	110	Sump pump + partial control system
Power for 200 kt		
UPS [kW]	5kW	.
Chilled Water [kW]	595	
Waste Heat to Air [kW]	317	Heat for 200 kt detector
Low Conductivity Water Needs	0	
Surface Power [kW]	771	
Network	10 Gb/s	1 dedicated line
Environment		
Temp. Min [C]	18	
Temp. Max [C]	25	
Humidity Min [%]	30	
Humidity Max [%]	50	
Rn Background [Bq/m <sup>3</sup> ]	OHSA limits in occupied spaces	

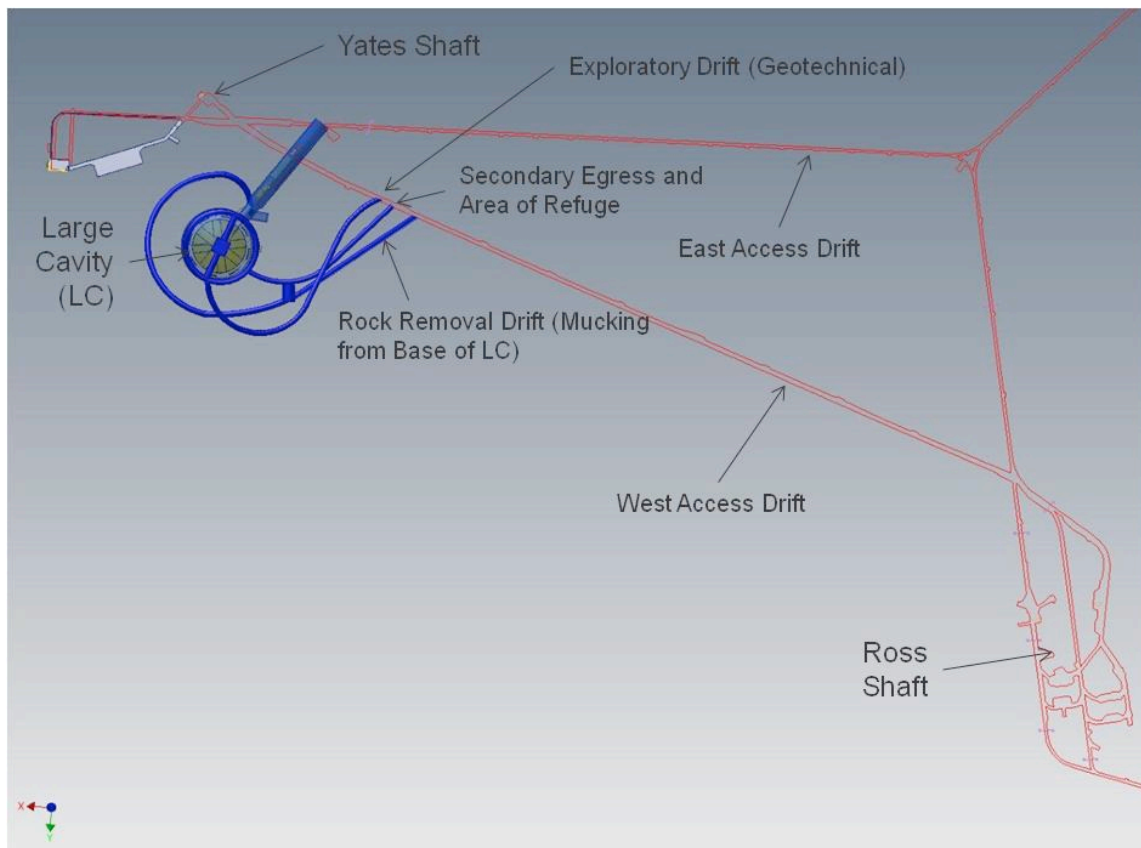


Figure 4-9: Plan view of the 4850L showing the Large Cavity (LC), the facilities related to the LBNE experiment, the Davis Campus (upper left), the Yate and Ross Shafts.

to achieve the life safety requirements change from phase to phase; and must be met throughout all phases. Paths for the ventilation air change as the excavation proceeds. Excavation sequencing must be considered accordingly. The methods of fire protection also change during the project, notably during installation of the PMTs when their cables are exposed to air before the Detector is filled with water. Temporary fire suppression is required during this part of the installation. Two egress paths are established with Areas of Refuge located and equipped to meet the occupancy during any phase. The Ross and Yates shafts are the primary and secondary means of egress for the entire underground facility, therefore proper scheduling of their maintenance and refurbishment is paramount.

For these configurations there is the “LBNE-Only” scenario where it is assumed that the LBNE Water Cherenkov Detector is the only experiment at Homestake. However, the placement of the Water Cherenkov Detector at the 4850 Level at Homestake is highly compatible with other experiments on the campus at this Level. In the LBNE-Only scenario careful consideration had to be made for maintenance, partial refurbishment and/or full refurbishment of one or both shafts. Decisions were made based on safety, cost and schedule on

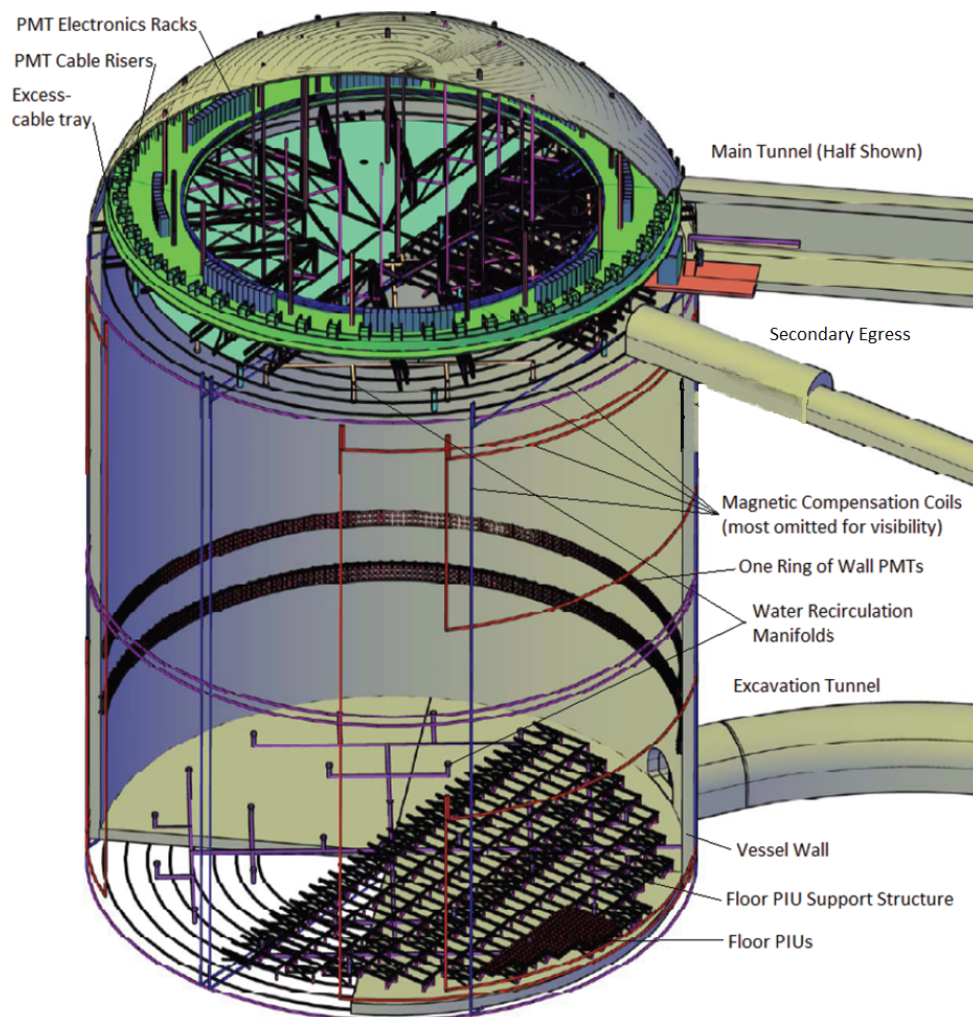


Figure 4-10: Isometric view of the dome of the water Cherenkov detector. There is a ‘balcony’ (green) around the perimeter of the cavity about 4 m above the 4850L. The balcony supports the cable penetrations around the perimeter and the eight sets of electronics racks. The structure is supported by large trusses that are in turn mostly supported from the rock above the dome. The total load on the rock above the dome is 600 T. The trusses are oriented so as not to obscure the entrance from the utility drift, the calibration drift, or calibration ports in the deck itself. The narrow, circumferential black lines and the red lines running down the side of the cylindrical volume represent the magnetic compensation cables for canceling the Earth’s magnetic field within the cavern. Only a few of the coils are shown. The structures at the bottom of the cavern are the PMT supports and water distribution system. This system is approximately repeated at the top of the cavern.

whether to partially refurbish both the Yates and Ross; or, fully refurbish one or both shafts. Refurbishment also reduces future shaft maintenance, improving reliability and increasing safety.

The LBNE-Only scenario does not require the enlargement of the East or West Access Drifts for hauling rock or ventilation except for truck by-pass areas in the west drift. The Detector operation configuration is to have the water purification system in the main utilities drift as shown in Figure 4-9. Mechanical, electrical and plumbing facilities services in both Detector sizes are to be in the Yates shaft. Detector vessel, liner and deck construction are highly integrated with the large cavity excavation. Vessel construction begins after beneficial occupancy of the large cavity. Both the excavation and the vessel have water drainage incorporated. The excavation surface finish and waviness are critical to vessel installation, and, if value engineering of an option without a vessel is approved, critical to the liner installation.

Operation of the Water Cherenkov Detector requires surface facilities. Buildings will be re-used as necessary to house the Detector fill water pre-purification system. Existing industrial water supply is used for fill. An existing substation on the Yates surface campus has adequate capacity for placement of additional transformers and backup generators needed by the experiment and life safety systems including the hoists, ventilation, fire protection and lighting. LBNE sponsored un-interruptible power supply capability is required for an orderly shutdown of the Detector computing and water system controls. Underground operations of the Detector have sustaining facilities requirements as well. Fire protection systems, communications infrastructure, areas of refuge are all needed for operations. Ventilation air is drawn through the spaces by the existing Oro Hondo shaft fans with a single new ventilation borehole required from 4850L to 3850L. Local cooling is to be provided by the experiment for electronics. The experiment has no additional heating and cooling requirements. The water recirculation system has a single chiller for removing heat in the water entering from the cavity rock, PMTs and other sources.

## 4.13 Installation

The installation effort provides the overall planning, scheduling, staging, and work planning for final assembly of all WCD equipment - above and below ground - at Homestake. Major systems that will be installed include:

- Photomultiplier tubes
- Water system
- Electronics DAQ system
- Magnetic compensation

- Deck
- Gas Blanket
- Vessel/liner

The Installation activities include management oversight, installation labor, materials and general use equipment required to perform these functions. For example, warehousing and storage, local transport, lift trucks and forklifts, man-lift, scaffolding and ladders, hand-tools, meters and o-scopes, fall-protection, PPE and general lifting equipment. Custom equipment and specialized labor remain the responsibility of each subsystem. All equipment ready for installation into the detector will be delivered to a central warehouse near Rapid City, SD. This equipment will be inventoried and stored. For example, the PMTs will be delivered from the manufacturer to a facility in which they will have bases attached, mounted in assemblies, and characterized. The PMTs will then be packaged and readied for assembly into the detector and delivered to the central warehouse. The PMTs may reside in this warehouse up to 3 years during which they will periodically undergo a series of tests to make sure they are still functional. These tests will not require removing the PMTs from their protective packaging.

The installation sequence is as follows

1. The large cavity will be excavated with ground support and rock stabilization. i.e. rock bolts, shotcrete and native water drainage.
2. Magnetic compensation system installed.
3. Water liner with additional drainage layer for leaks is installed.
4. Balcony - supporting the electronics, infrastructure and utilities installation.
5. Deck will be built on the floor of the vessel.
6. Deck will be raised 10 feet and the PMTs will be mounted to the bottom.
7. Deck will be hoisted into position at 4850.
8. Wall PMTs will be deployed via wired and the signal cables tied into place.
9. Floor PMT's are mounted and the cables tied into place.
10. Deck annulus PMT's installed.
11. PMT survey is completed.
12. Electronics installation and checkout is complete.

13. Deck is closed and made light and gas tight.
14. Water system installation, fill detector with water and leakcheck.
15. Final checkout of systems.
16. Ready for operations.

The estimated duration for installation of the technical components is  $\sim 2$  yr. Thereafter the detector is ready for first light and operations. Even without beam, the detector is still active for extraterrestrial neutrino observation and proton decay.

## 5 Experimental Approach

The members of the LBNE collaboration have long experience designing, building, and extracting physics both from large scale water Cherenkov detectors and long- (and short-) baseline neutrino experiments. Our approaches to operation, calibration, simulation, and data analysis overlap in many ways but are also in many ways distinct: each collaborator's past experience is brought to the table and debated, and we believe that this process of creating an experiment from the best of these different approaches will add great strength to the physics program of LBNE.

We describe here the results (to date) of our developing plan for extracting the physics from the LBNE water Cherenkov detector, starting with our assumptions and simulation of the beam, to calibrations, detector simulations, and reconstruction of events, including rejection of backgrounds. We focus here on the physics associated with the beam, but include a few details relevant to non-accelerator physics and lower energies.

### 5.1 The LBNE Beam Design and Simulation

The LBNE beamline will be a new neutrino beamline located at Fermi National Accelerator Laboratory that utilizes the 700 kW 120 GeV proton beam from the Fermilab Main Injector (MI) accelerator. The NuMI (Neutrinos at the Main Injector) [10] beamline from the MI is currently the most powerful neutrino beamline in operation. The NuMI beamline has been operational since Jan 21, 2005 and delivered in excess of  $1 \times 10^{21}$  protons-on-target (POT) to the MINOS long-baseline neutrino experiment [11]. The GEANT3/FLUKA08 [12] [13] based simulation of the NuMI beamline has been validated using data from the MINOS experiment. We have used the NuMI beamline simulation to optimize and validate the LBNE beamline design.

We studied the physics performance of several conventional horn-focused neutrino beam designs using a detailed beam simulation. Our studies considered different decay pipe geometries and different conventional focusing horn designs (BNL-AGS, NuMI, T2K) and different beam tunes (horn/target placement and horn currents). For the physics sensitivity studies

reported here, we chose a beam tune and design that maximized the number of oscillated  $\nu_e$  appearing at the Far Detector. We assumed a helium-filled decay pipe with a length of 280 m and a radius of 2 m. The current conceptual design of the LBNE decay pipe has limited the length to 250 m or less to reduce costs. The target simulated is a solid carbon/graphite cylinder 0.6 cm in radius, 80 cm long with a density of  $2.1 \text{ g/cm}^3$  \*. We assume the same two focusing parabolic horn designs as used for the NuMI neutrino beam, without modification. The target is inserted 50 cm into NuMI horn 1. The horn current is 250 kA and the horns are 6 m apart. In Figure 5-1 different beam tunes obtained from moving the target w.r.t to the first horn, or going off-axis are shown. The target partially inserted into horn 1 (50 cm in) is the Low-Energy (LE) beam tune that produced the largest rate of  $\nu_e$  appearance at a detector located 1300 km from the target. This is the default beam used in most of the long-baseline physics studies reported in this chapter. The off-axis beam is used to estimate sensitivities at very short baselines, and the beam with the target pulled out 1.5 m - the Medium Energy (ME) beam tune - is used to maximize  $\nu_\tau$  appearance rates. A tunable beam is also desirable for constraining the focusing uncertainties on the near to far detector extrapolation. For this reason, a beam with at least 2 tunes (LE, ME) is being considered for LBNE.

**LBNE Beam Tunes**

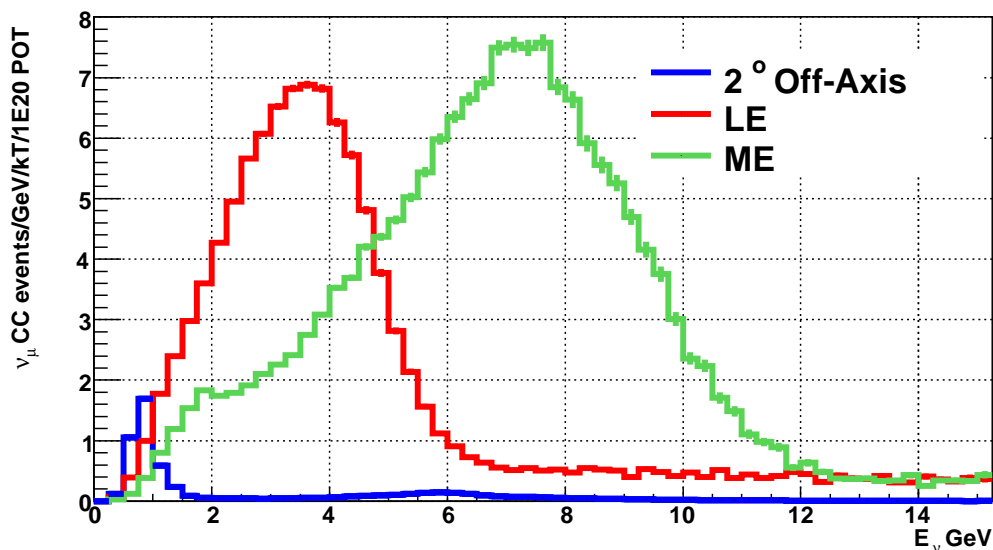


Figure 5-1: Different possible LBNE beam spectra at a baseline of 1300km. The LE beam is as described in this section. The ME tune is produced by pulling the target out 1.5m from horn 1. The off-axis tune is  $2^\circ$  off-axis to the LE tune.

In Fig. 5-2, the  $\nu_\mu \rightarrow \nu_e$  oscillation probability for the LBNE to Homestake baseline of 1300 km for different mixing parameters is shown as colored curves. The total CC  $\nu_\mu$

\*Recent target irradiation studies at BNL indicate that a carbon-composite material with this density is a good target material candidate, provided the material is clad.

spectrum from the LBNE LE candidate beam design is shown as the black solid histogram. At the second oscillation maximum, where CP effects are the largest, the current LBNE

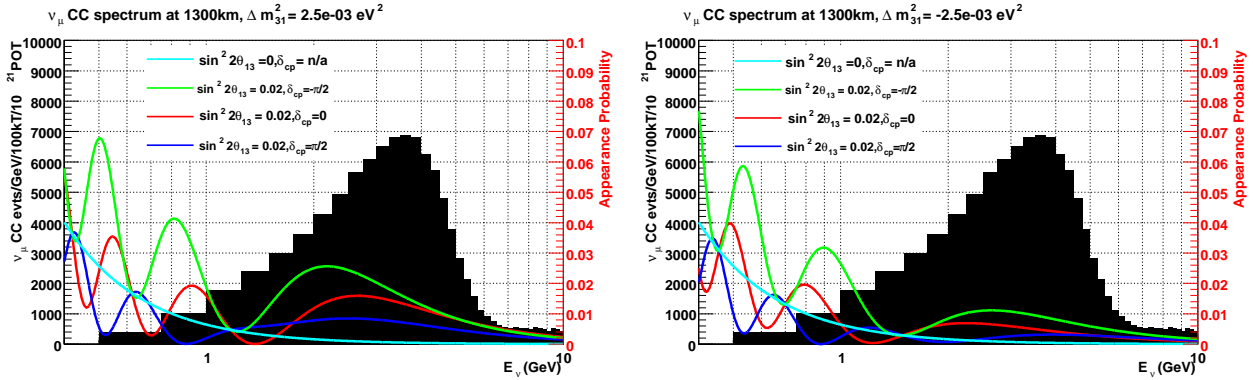


Figure 5–2: The  $\nu_\mu \rightarrow \nu_e$  oscillation probability for the LBNE to DUSEL baseline of 1300 km for different mixing parameter with normal hierarchy (left) and inverted hierarchy (right), is shown as colored curves. The unoscillated CC  $\nu_\mu$  spectrum from an LBNE candidate beam is shown as the solid black histogram.

beam designs do not produce as much on-axis flux as we would like. We are therefore re-examining and re-designing the target and focusing system to better optimize this, and thus maximize our sensitivity to the CP phase and the mass hierarchy.

## 5.2 Detector Simulation

The performance assumptions we used to evaluate physics sensitivities are based on Super-K detector simulation and reconstruction algorithms. Super-K had several run periods with different detector configurations. In the SK-I period, the photocathode coverage was 40%. During the SK-II period, the coverage was reduced to 20%. Atmospheric neutrino Monte Carlo from the SK-II period was fully reconstructed with the Super-K tools and re-weighted to the LBNE beam flux in order to calculate the sensitivity of the experiment. These Monte Carlo simulations and tools have been extensively validated against beam and atmospheric data sets and are state-of-the-art in their performance. From this work, we conclude that a WC detector with the same performance characteristics as Super-K II will perform at the level required to meet our physics objectives. We would expect a detector with higher light collection would perform better; our motivation for choosing Super-K II is that is the minimum coverage (and hence lowest cost) that we know can achieve our physics goals.

In order test more precisely the effects of varying detector geometries and phototube coverages for LBNE, we have designed an extremely flexible GEANT4 based simulation framework (WCSim). This code was built on the base used to design the 2KM complex for the T2K experiment [14]. In that context, the simulation was shown to match the performance

of Super-K for the T2K  $\nu_e$  appearance search at the better than 10% level.

The simulation code is based on the modern and modular GEANT4 system. The code allows us to easily simulate many detector options creating any size water Cherenkov detector with any needed tube response we need, but also, most critically, it allows us to also simulate the Super-Kamiokande detector itself. Then, we can do a direct comparison with the Super-K Monte Carlo simulation. The Super-K simulation has been validated with data from Super-K, K2K and T2K and calibrated with a variety of sources to the 1% level. Therefore, if we obtain the same response between the two simulations, we can be quite confident in our results.

The output of the Monte Carlo simulation includes both true raw hit information, and digitized times and charges. WCSim includes the water, black sheet, Tyvek, and tube characteristics of the Super-K detector along with the simulation of its digitizer. Optical parameters were tuned for agreement with Super-Kamiokande, running a geometry based on Super-Kamiokande. With little tuning, the energy scale agreement was found to be at the 10% level, with the worst performance at low energy. After tuning, we then switched the simulation to the geometry and coverage to the LBNE configuration to study the response, confident that we are correctly simulating the basic response of the detector. An example of this work can be seen in Fig. 5-3 which shows good agreement between the two simulations. After some basic initial tuning, the raw charge scale difference between two simulations for 15 GeV muons was  $\sim 5\%$ .

The output of the simulation has also been used extensively for low energy studies and set several design requirements necessary for the case of the inclusion of gadolinium into the design. The hits were taken from the Monte Carlo simulation and vertex resolution along with radioactive background and dark noise were simulated and then used to calculate the neutron tagging efficiency. This information was used to set the requirements on the radioactivity levels of the concrete used in the detector walls, along with their thickness. Finally, the Monte Carlo simulation is also now being used to study the inclusion of various veto options.

## 5.3 Reconstruction

Reconstruction affects nearly every physics topic LBNE will address. We focus here on some of the details of the reconstruction of beam events, and discuss a few specifics of low-energy reconstruction later, in Section 10.2.1.

In the  $\nu_e$  appearance analysis an excess of electron-like events are searched for in a mostly pure  $\nu_\mu$  beam. Various backgrounds which look like  $\nu_e$  events are also reduced when possible. Principally, these backgrounds are intrinsic electron neutrino contamination in the beam from kaon and muon decay, and the mis-identification of neutral current produced  $\pi^0$ s

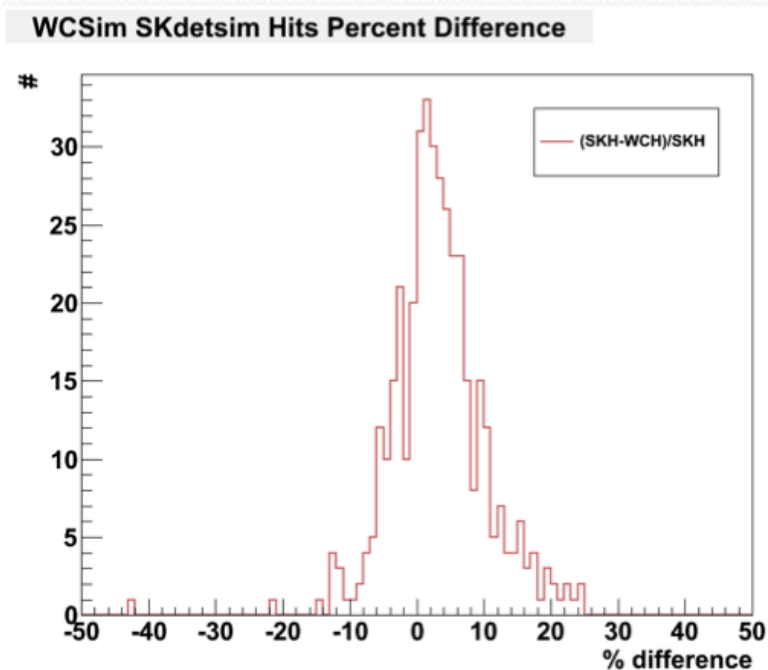


Figure 5-3: Comparison of Super-K Monte Carlo simulation with the WCSim GEANT4 simulation with nominal tuning. Shown is a comparison of collected raw charge per pathlength from the PMTs for 15 GeV through-going muons. The average difference is  $\sim 5\%$ . The percentage difference between the same events simulated in the two Monte Carlos simulations is shown. The width of the distribution is primarily due to the natural fluctuation in the number of detected photons in the two different detectors.

in which one of the two rings was not identified. In a WC detector the proton from a neutrino interaction is often not identified, but using only the lepton, the neutrino energy for single-ring beam neutrino events can be reconstructed assuming the event was a charged-current quasi-elastic interaction,  $\nu_l + n \rightarrow l^- + p$  using the following formula:

$$E_\nu = \frac{E_{lepton} m_N - \frac{1}{2} m_{lepton}^2}{m_N - E_{lepton} + p_{lepton} \cos \theta_{lepton}} \quad (5.1)$$

where  $E_{lepton}$ ,  $m_{lepton}$ ,  $p_{lepton}$ , and  $\theta_{lepton}$  are the electron or muon energy, mass, momentum, and angle with respect to the beam direction and  $m_N$  is the nucleon mass. (The binding energy of oxygen is ignored in this expression.)

Typical momentum resolutions are  $\sim 3\%$  ( $\sim 4.5\%$ ) for 1 GeV/c electrons in SK-I (SK-II) and the electron angular resolution is  $\sim 3^\circ$  ( $1.5^\circ$ ) for sub-GeV rings (multi-GeV rings) [16]. Taking into account these resolutions, the Fermi motion, and the effect of contamination from non-quasi-elastic events in the selected sample, the electron neutrino energy resolution is expected to be  $\sim 10\%$  at 1 GeV.

In order to reconstruct the energy and also specify whether a particle came from a muon or electron neutrino, several steps are undertaken. It should be noted that at high energy, many events are not quasi-elastic but rather from single-pion, multi-pion, and deep-inelastic scattering interactions. Therefore in many events there will be large numbers of particles, above Cherenkov threshold all producing light. In order to identify all of these particles several algorithms are run, most employing likelihoods to compare the observed with expected hypotheses. At least for the case of Super-K, which was used to generate the sensitivities, the algorithm is a general one and the same code is used to find all event categories.

The full reconstruction chain used by Super-Kamiokande is quite complex but roughly it follows the following steps: First, a vertex is found using mostly timing information. Then, a simple ring-finder finds the most energetic ring. At this point a recursive Hough-based ring-finder is employed. Fixing the information from the ring that is already known, a Hough algorithm picks possible other ring positions in the event. A likelihood comparison against the data is then used to determine if the addition of any of those rings increases the agreement with the event pattern. If so, the best new ring found is fixed and the process repeats until no new rings need to be added. At this point, the rings need to have their particle identifications assigned on the basis of expected light patterns. Then, the charge must be correctly apportioned between the rings and the parameters such as the vertex positions and ring directions can be refit with the improved information now available. Additional steps exist including, for example, the identification of decay electrons.

As already mentioned, one of the key factors for a  $\nu_e$  appearance search in a WCD is the rejection of backgrounds due to  $\pi^0$ s. The signal for a  $\nu_e$  interaction is a single electron-like ring. CC interactions from  $\nu_e$  that are intrinsic to the beam form an irreducible background as the signature is exactly the same as the signal. On the other hand, if a  $\pi^0$  is produced, it can decay via  $\pi^0 \rightarrow \gamma\gamma$ . The  $\gamma$ s form two fuzzy (electron-like) Cherenkov rings. If the opening angle between the two gammas is small, the rings overlap and will sometimes be reconstructed as one electron-like ring. In addition, if the decay is asymmetric, a small low-energy ring might be missed. In this way, the  $\pi^0$  can generate an event topology that mimics the  $\nu_e$  signal. In lower energy off-axis experiments such as T2K, a dedicated algorithm is used to eliminate these events. All one-ring e-like events are examined and assuming there is a second ring from a  $\pi^0$  decay present, the most likely 2nd ring is identified using a likelihood. Then, the probability that the 2nd ring is real and the two rings have an invariant mass of a  $\pi^0$  is considered. Those events consistent with neutral current background are removed.

At higher energy, with a wide-band beam, the NC background is more pernicious as there is a larger high-energy tail to make neutral current events which feed down into the signal region. For this case, instead of making a simple cut as described above, a likelihood consisting of several variables is constructed to remove the neutral current background. That is the approach taken in our LBNE studies.

A study of  $\nu_e$ -appearance background rejection in a large WCD using simulation and

reconstruction tools from SK-I is described in detail in [15]. By developing a likelihood function based on nine discriminating variables, the authors demonstrate an improvement in the signal-to-background ratio over the standard Super-Kamiokande analysis for this energy range. Similar results were found in an independent study [16]. The signal and background efficiencies assumed in our  $\nu_e$  appearance studies of Chapter 6 come from the analysis in [15].

We know based on the physics publications by the T2K collaboration that  $\nu_e$  appearance measurements are possible in a large water Cherenkov detector. To apply these techniques to LBNE, we have been using reconstruction/particle ID tools developed by Super-Kamiokande and run on LBNE-simulated events, as well as developing our own LBNE-specific set of reconstruction tools. Throughout, we have assumed the same light collection as Super-Kamiokande II, which studies have shown is near the minimum needed to achieve the long-baseline physics goals. Reconstruction in LBNE will be in some ways more difficult than Super-Kamiokande II, and in others somewhat better. The issues that will make reconstruction and particle ID more difficult are:

- The larger detector size means there will be more Rayleigh scattering and attenuation, adding further position-dependence to energy and position reconstruction.
- The use of light enhancement—either Winston cones or wavelength-shifting plates—in place of additional PMTs adds further ‘late light’, decreasing the ratio of prompt to late light as compared to Super-Kamiokande II, thus making position and time reconstruction poorer.
- The additional scattering and attenuation will provide more smearing to Cherenkov rings, making separation of neutral current  $\pi^0$  events from appearance electrons harder.
- The wideband beam will produce harder  $\pi^0$  events which are more likely to leak into the  $\nu_e$  appearance signal box.

Issues that will make reconstruction in LBNE better than in Super-Kamiokande II will be:

- The better timing of our reference design PMTs—1.3 ns for the width of the transit time jitter compared to about 2.5 ns for Super-Kamiokande II—will provide a sharper rising edge on the prompt time distribution and thus better position and time reconstruction.
- The smaller size of the PMTs will mean more effective pixels, thus providing better angular information.
- The better charge response of the reference design PMTs will help to identify multiple hits on PMTs.

- More sophisticated analysis techniques are already being developed, which will use more of the information in reconstruction and thus provide better position, energy, and particle ID information.

A large part of the effort now underway is studying exactly how the first list will affect our background rejection, as well as optimizing items on the second list. We note that as far as light enhancement is concerned, both SNO and IMB successfully reconstructed events with high precision using different light enhancement approaches.

### 5.3.1 Super-K based reconstruction tools

We have compared the results of our reconstruction of LBNE simulated events using Super-Kamiokande reconstruction tools, examining GeV scale muons, electrons,  $\pi^0$ s, and low-energy electrons and positrons.

For example, Fig. 5-4 shows the invariant mass distribution for reconstructed  $\pi^0$  in both Monte Carlo simulations in the Super-K configuration. The relative difference in the fitted peak between the two is 1.4%. It should be noted achieving this agreement indicates that ring-counting, particle ID and photo-electron to energy conversion are all working well.

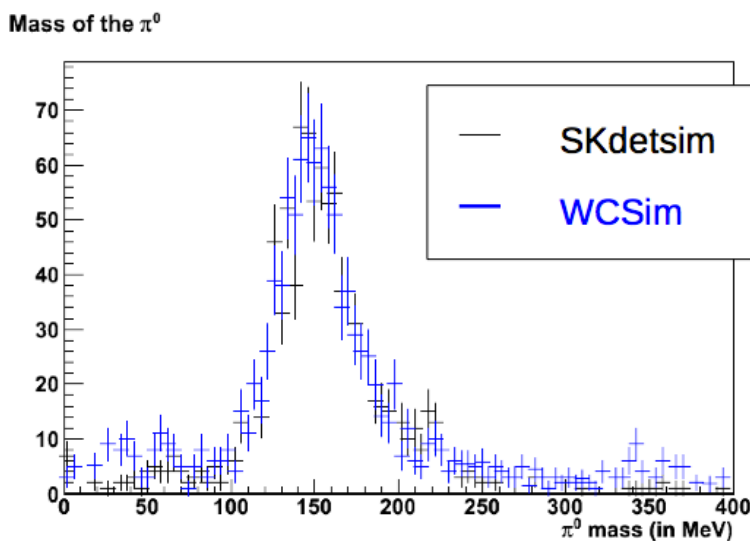


Figure 5-4: Comparison of the invariant mass peak for 2-ring e-like events from  $\pi^0$  decays in the Super-K configuration of WCSim compared with the standard Super-K Monte Carlo output. The fitted peaks agree to better than 2%.

Good agreement between the two Monte Carlo simulations when running in the WCSim Super-K mode was found. For example, for 1 GeV electrons vertex resolution was 35 vs 34 cm

in the two simulations, the angular resolution for single ring events was 1.8 vs 1.5 degrees and the particle mis-identification based on the pattern alone was 2.8 vs. 3.1%. After tuning and comparing with Super-K configuration, the GEANT4 simulator was then used to simulate the geometry relevant for the LBNE experiment.

In the LBNE configuration, lower physical PMT coverage area with higher quantum efficiencies in a larger tank are used. For example, Tab. 5-1 shows a comparison between some critical parameters in the reconstructed 12% HQE configuration and the standard SK-II output. The results vary as a function of input energy and particle type and we have chosen one point that shows some discrepancies, but overall the agreement is very good at this stage.

	skdetsim (SK-II mode)	WCSim 12% HQE	Difference (sigma)
Vertex Resolution	$36.0 \pm 2.3$ cm	$31.9 \pm 2.5$ cm	-1.7
Angular Resolution	$1.0 \pm 0.2$ deg	$1.2 \pm 0.3$ deg	1.0
Energy Resolution	$2.6 \pm 1.2$ %	$2.5 \pm 0.8$ %	0.1
Particle MisID	$2.5 \pm 0.3$ %	$3.1 \pm 0.4$ %	2.0

Table 5-1: Comparison between SK-II and WCSim for a 150kton 12% physical photocathode coverage using high quantum efficiency (HQE) PMTs configuration with preliminary SK reconstruction. The comparisons are shown for reconstructed monochromatic 1.5 GeV electrons.

We know that we have more work to do to optimize the code for this low coverage case, but these results already leave us confident that we can obtain similar basic responses between the two detectors.

### 5.3.2 LBNE based reconstruction tools

Work has also begun on standalone reconstruction tools usable by the LBNE collaboration as a whole. A few are already complete and available, such as versions of low-energy event and muon fitters which were independently written by LBNE members for the IMB and Super-K collaborations. Additionally, completely new algorithms based on many of state-of-the-art ideas developed by IMB, Super-K and MiniBooNE are now being implemented within LBNE. As an example, Fig. 5-5 shows a reconstructed ring processed from the WCSim output.

We have recently also developed a new tool called Chroma which does very fast ray-tracing using GPUs—200 times faster than GEANT4. This speed allows likelihoods to be calculated using an entirely Monte Carlo approach, including all effects (scattering, reflections, etc.) that are included in the simulation. Different event hypotheses (say,  $\pi^0$ s compared to electron events) are handled easily, simply by flipping a simulation switch. To deal with

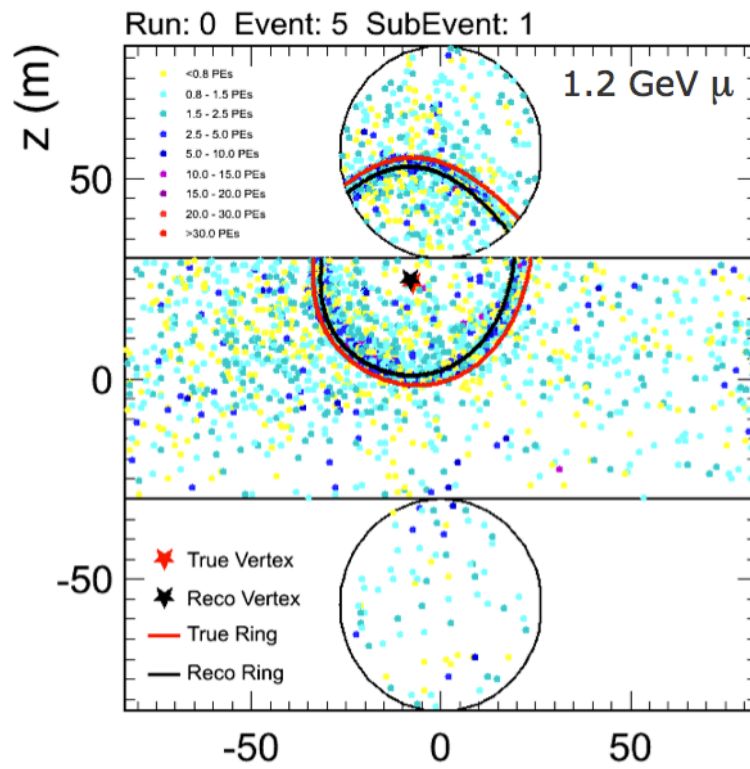


Figure 5-5: A reconstructed Cherenkov ring from a 1.2 GeV muon simulated using WCSim by the new standalone LNBE tools utilizing a Hough algorithm.

the associated fluctuations in the likelihood space, we have developed a stochastic gradient descent method (a ‘fuzzy fitter’) that is robust to these variations. We are currently optimizing the fitter to increase its speed further, but our initial results look very promising. Figure 5-6 shows a 1.5 GeV electron event and the associated hit PMTs in LBNE, rendered by the Chroma photon propagation code.

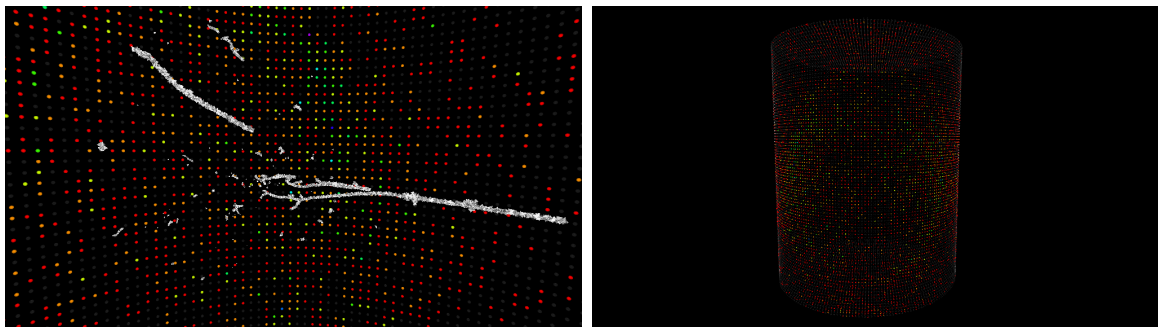


Figure 5-6: A 1.5 GeV electron track shown in the LBNE detector, rendered using the Chroma photon propagation code (left) and the associated Cherenkov ring viewed from outside the detector (right). The green PMTs are hit by a single photon, red by two photons, and blue by three photons.

### 5.3.3 Future Work

We believe that the use of re-weighted Super-K simulation combined with the validated output of our GEANT4-based simulation makes a case that a detector with HQE PMTs with the same light collection efficiency as SK-II will meet our performance goals.

Our main R&D task as we move towards CD2 is to show that if the number of phototubes is reduced even further, and the missing photons are still collected by a light collection system we can achieve the same performance. The work to implement these options into the Monte Carlo to do this study has also begun.

## 5.4 Calibrations

One of the advantages of the water Cherenkov technique is the simplicity of the detector. The response is determined by known physics (particle passage through water and the generation of Cherenkov light) and detector parameters (optics and PMT response). The calibration program must thus do three things: measure parameters like bulk optical properties (such as scattering and attenuation lengths), generate corrections to things like

PMT times and charges, and provide tests of the detector model and accuracy of energy, position reconstruction, and particle ID. By creating as physical a model of the detector as possible, we will have confidence that extrapolating tests done with calibration sources (say MeV-scale electrons or cosmic muons) to real beam events will be accurate. Our program is thus aimed at measuring physical parameters, including those describing the photomultiplier behavior, as precisely as possible.

The vertex and angular resolution functions will be confirmed using a combination of radioactive sources and muons (in conjunction with a top veto). Understanding the efficiency of the particle-identification algorithms will require a detailed understanding of the detector performance — including the propagation of light within the detector. Therefore the primary determination of the particle identification will use a complete Monte Carlo simulation of the WCD. To ensure that the simulation correctly characterizes the behavior of the detector, we will deploy several systems that will allow for a direct comparison with the Monte Carlo and to monitor the stability over time.

Vertex resolution varies as a function of energy and depends on whether the event is e-like or  $\mu$ -like. Based on experience from similar WCDs such as Super-Kamiokande ([106], [110]), the vertex resolution for both e-like and  $\mu$ -like events should be determined with less than 30 cm uncertainty in the high-energy range. As the particle energy decreases, the amount of emitted Cherenkov light decreases as well, increasing the uncertainty in the vertex resolution. Thus the vertex resolution in the low energy range should be better than 200 cm, although this requirement may vary, depending on the detector photo coverage and physics goals. Another important element for differentiating between e-like and  $\mu$ -like events and determination of their energy is the angular resolution, which should be better than  $3^\circ$  for e-like and  $1.8^\circ$  for  $\mu$ -like events in the high energy range. Angular resolution becomes significantly worse in the low energy range for the same reasons as the vertex resolution.

Particle misidentification for e-like and  $\mu$ -like is crucial for the  $\nu_e$  appearance search and thus should be less than 1% for all particle types. Finally, the Cherenkov ring finding algorithm should achieve more than 90% efficiency while rejecting 99% of the background at neutrino energies of 1 GeV.

We will utilize several approaches using hardware systems and software algorithms for calibration and monitoring of the vertex resolution uncertainty, angular resolution uncertainty and particle identification efficiency throughout the energy range of interest:

- Cherenkov Simulating Light Pulser (CSLP) which are battery operated light pulsers that emit light cones with several tunable parameters: light intensity, light-cone direction, cone opening, thickness of the cone envelope and sharpness of the cone envelope. In this way, a CSLP will be able to simulate light cones produced by electrons and gammas of various energies (different cone opening and fuzziness). The CSLP cones provide a control data sample of known energy and direction for single and two ring

events providing a way to monitor particle ID for electrons versus  $\pi^0$ .

- Naturally occurring events inside the detector (e.g., Michel electrons) with dedicated software to utilize these events. The non-exhaustive list, for both high and low energy includes: cosmic muons (number of photo-electrons as a function of track length, number of photo-electrons as a function of Cherenkov angle for low energy muons, spectrum of Michel electrons, stopping muons) and neutral pions (reconstruction of  $\pi_0$  invariant mass). For vertex and angular resolution a veto region will help better determine the position of entering muons.
- Injection of downward-going electrons of known energy and position via a LINAC will provide vertex-resolution calibration as a function of energy and position the low energy range (5 MeV – 16 MeV).
- Radioactive sources deployed at various locations inside the detector volume provide a valuable tool for determination of vertex shifting and resolution in the lowest energy range. Uniform gamma sources will be designed and deployed to assess any vertex shift in the detector. Various radioactive sources will be used to calibrate vertex resolution as a function of energy in the low energy regime up to 20 MeV, where vertex resolution deteriorates quickly with decreasing energy. In the case of gadolinium loading, deployment of neutron sources will also be needed to measure the neutron capture efficiency.
- We have been discussing the possibility of a high energy accelerator that would allow us to directly test both our detector simulation model and our reconstruction and particle ID efficiencies. We have not included this option in our costing at this stage.



## 6 Long-Baseline Neutrino Physics

Long-baseline neutrino oscillation physics is the primary focus of LBNE. While our highest priority is a search for CP violation in the lepton sector, the great strength of the long-baseline, on-axis, wideband-beam approach is that it will allow us to make precision measurements of nearly all elements of the PMNS matrix as well as resolving the mass hierarchy, in a single experiment.

Appearance measurements of  $\nu_\mu \rightarrow \nu_e$  alone will allow:

- An observation of  $\nu_e$  appearance \*
- a more precise measurement of  $\theta_{13}$  or extension of the limit beyond current experiments,
- a determination of the neutrino mass hierarchy, i.e, whether the mass ordering is normal:  $\Delta m_{31}^2 > 0$  or inverted:  $\Delta m_{31}^2 < 0$  (assuming  $\theta_{13} \neq 0$ ),
- a measurement of leptonic CP violation through measurement of the CP violating phase,  $\delta_{CP}$  (assuming  $\theta_{13} \neq 0$ ), and
- a search for non-standard neutrino interactions that interfere with neutrino oscillations.

In addition to precision measurements of the unknown neutrino matrix parameters accessible through  $\nu_\mu \rightarrow \nu_e$  oscillations such as  $\theta_{13}$ , the mass hierarchy, and  $\delta_{cp}$ , LBNE will enable precision measurements of the atmospheric neutrino oscillation parameters:  $\Delta m_{32}^2$ ,  $\theta_{23}$  for both neutrinos and anti-neutrinos with a degree of precision that exceeds current experiments. LBNE can also make an observation of  $\nu_\tau$  appearance with sufficient statistics to test the 3-flavor model of neutrino oscillations, and to extend the search for non-standard interactions in the  $\nu_\tau$  appearance channel.

The measurement capabilities of an LBNE Water Cherenkov detector (WCD) to the different physics associated with  $\nu_\mu$  oscillations are discussed in Section 6.1. The LBNE detailed beam and WC detector simulation used to estimate the performance parameters used in the

---

\*If  $\theta_{13}$  is 0,  $\nu_e$ s will appear due to  $\nu_\mu$  oscillations from the solar oscillation term.

physics sensitivity calculations are presented in Sections 5.1 and 5.2. The beam and detector performance parameters obtained from the simulations described in Sections 5.1 and 5.2 are implemented into the General Long-Baseline Experiment Simulator (GLOBES) [17] framework which is used to calculate the physics sensitivities discussed in this section. Although many of these studies were done with the initial 280 m decay pipe, we have found that the much-lower cost 250 m decay pipe described in the previous chapter has a very small impact on our ultimate oscillation sensitivities.

We have not explicitly investigated near-detector configurations in our studies, but instead have assumed that any near detector will be able to provide the normalization for background processes to 5% and signal to 1%. We further assume, based on the work described in the previous chapter and the references therein, that our acceptance for  $\nu_e$  signal events is 15%, and the background leakage from NC  $\pi^0$ s is 0.6%.

## 6.1 Long-Baseline $\nu_\mu \rightarrow \nu_e$ Oscillations

A large WC detector (WCD) operating at a long baseline will be able to significantly extend the sensitivity to  $\nu_\mu \rightarrow \nu_e$  oscillations. For the mass hierarchy and CP violation we will demonstrate that such an experiment can extend the  $3\sigma$  sensitivity almost an order of magnitude beyond current neutrino oscillation experiments. Figure 6–1 and Table 6–1 give the expected event rates for  $\nu_e$  appearance measurements in a 200 kton WC detector at a baseline of 1300 km (FNAL-Homestake) from the the LBNE beamline target (see Section 5.1) for normal and inverted mass hierarchies. The appearance rates are higher for the normal mass hierarchy in the case of neutrinos and for the inverted hierarchy in the case of antineutrinos. From Figure 6–1, we also see the effect of the  $\delta_{CP}$  phase: larger neutrinos rates are expected for negative phases (both normal and inverted hierarchies), while larger antineutrino rates expected for positive phases. By exploiting such differences in the neutrino and antineutrino  $\nu_e$  appearance spectra observed at these large distances, separate information on  $\theta_{13}$ , the mass hierarchy, and CP violation can be obtained. In addition, a very long-baseline experiment exploiting a wide-band neutrino beam, such as the on-axis LBNE beam, can resolve the oscillation parameter degeneracies in the  $\nu_e$  appearance spectrum and allow a precision measurement of the value of  $\theta_{13}$  and the  $\delta_{CP}$  phase.

The sensitivities to  $\theta_{13} \neq 0$ , our ability to resolve the neutrino mass hierarchy, and our ability to determine CP is violated are summarized in the following sections. The sensitivities are all estimated assuming a 1300 km baseline from the LBNE beam at Fermilab which corresponds to the location of the Homestake mine. A discussion of the impact of different baselines on the oscillation sensitivities will also be discussed in Section 6.5.

	WC ( $\nu$ mode)	WC ( $\bar{\nu}$ mode)
<u>Normal mass hierarchy:</u>		
Oscillated $\nu_e + \bar{\nu}_e$	484	180
Beam $\nu_e + \bar{\nu}_e$	218	115
NC Bkd	276	118
Mis-identified $\nu_\mu$ CC	15	7
<u>Inverted mass hierarchy:</u>		
Oscillated $\nu_e + \bar{\nu}_e$	212	261
Beam $\nu_e + \bar{\nu}_e$	221	114
NC Bkd	276	118
Mis-identified $\nu_\mu$ CC	15	7

Table 6-1: Number of  $\nu_e$  and  $\bar{\nu}_e$  events expected in a 200 kton WC detector in 5 years each of neutrino and antineutrino running in a 700 kW beam. Rates have been integrated over the region from 0.5 – 12 GeV. In correspondence with Figure 6-1, this assumes  $\sin^2 2\theta_{13} = 0.04$  and  $\delta_{CP} = 0$ . ‘NC’ refers to backgrounds from neutral current events looking like  $\nu_e$  events.

### 6.1.1 Sensitivity to $\theta_{13} \neq 0$

Based on current projections, upcoming reactor and accelerator-based experiments should be able to distinguish  $\theta_{13}$  from zero at the  $3\sigma$  level for  $\sin^2 2\theta_{13}$  values down to 0.02 before LBNE is in operation [18]. Figure 6-2 shows the sensitivity of LBNE to  $\theta_{13} \neq 0$ . The results are dependent on both the value of  $\delta_{CP}$  and the mass hierarchy. As can be seen, the sensitivity is better for normal mass hierarchy unless  $\delta_{CP} = 45 - 180^\circ$ , in which case the sensitivity is better for inverted mass hierarchy.

Of course, the sensitivity of LBNE to determining a non-zero value of  $\theta_{13}$  also increases with longer exposure, for a constant beam power. Figure 6-3 shows the sensitivity in a WC detector as a function of exposure at the  $3\sigma$  level. LBNE can probe  $\sin^2 2\theta_{13}$  down to the  $10^{-3}$  level with reasonable detector and beam assumptions. For example, with a standard 2000 kt-yr exposure to a 700 kW beam, and normal mass hierarchy, a WC detector is sensitive to  $\sin^2 2\theta_{13} \neq 0$  at  $3\sigma$  down to a  $\sin^2 2\theta_{13}$  value of 0.008 for 100% of all possible  $\delta_{CP}$  values. Note: the sensitivity is worse for an inverted mass hierarchy.

In Figure 6-4 we show the LBNE discovery reach for non-zero  $\theta_{13}$  compared to other long-baseline experiments. The NO $\nu$ A and T2K sensitivities were provided to us by Joachim Kopp.

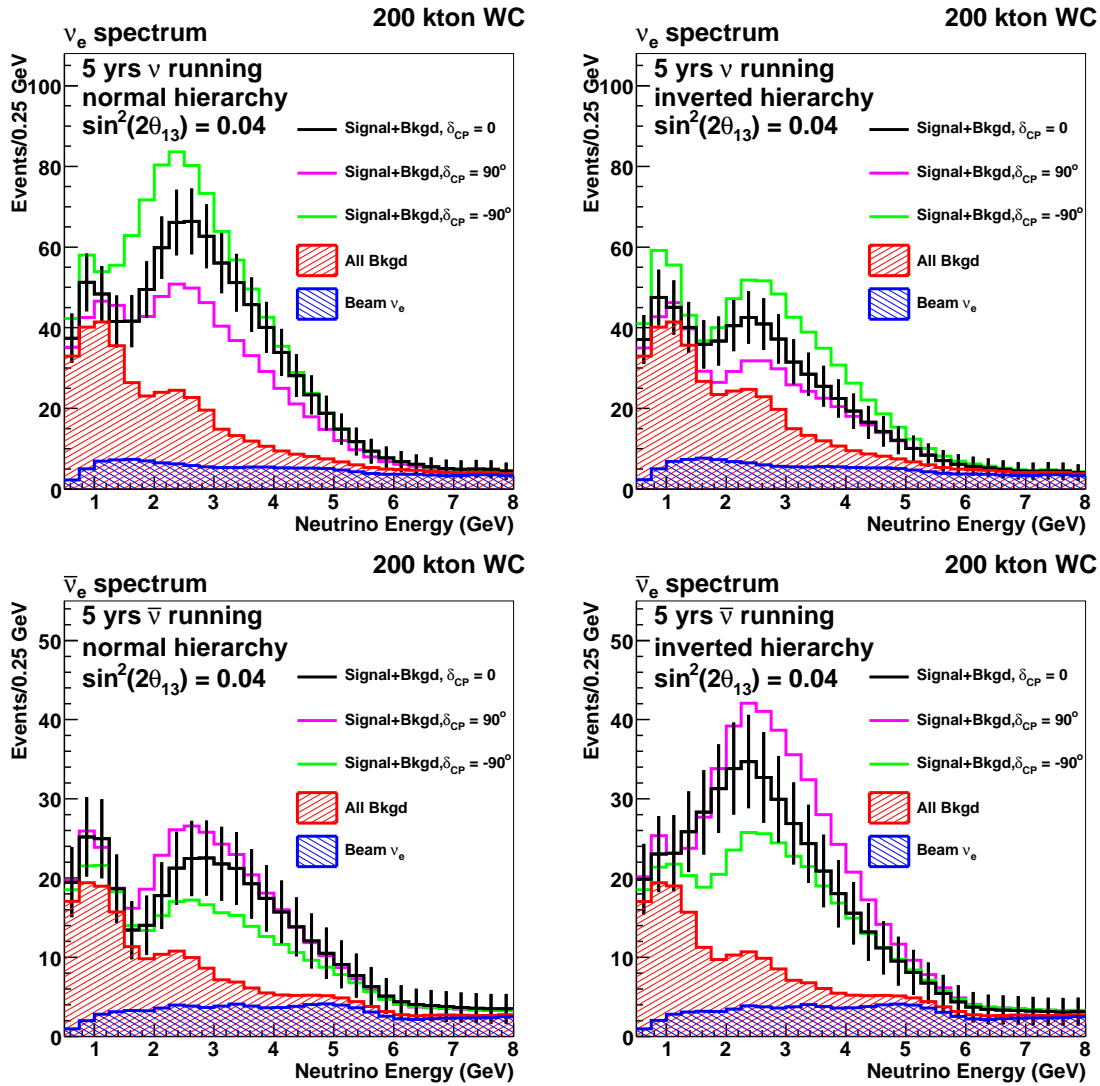


Figure 6-1: The expected  $\nu_e$  spectra in a 200 kton WC detector assuming  $\sin^2 2\theta_{13} = 0.04$  and 5 years of neutrino (top) and antineutrino (bottom) running in a 700 kW beam for normal (left) and inverted (right) mass hierarchies. The black points assume  $\delta_{CP} = 0$  while the pink and green lines are for  $\delta_{CP} = \pm 90^\circ$ . The different background contributions are indicated by the hatched histograms with intrinsic  $\nu_e$  events shown in blue and the total background contribution including intrinsic  $\nu_e$ , NC, and mis-identified  $\nu_\mu$  CC events in red. In the case of antineutrino running, the signal and background distributions explicitly include an additional contribution from neutrinos in the beam. Error bars are statistics only.

### 6.1.2 $\nu_e$ Appearance if $\theta_{13} = 0$

In Figure 5-2 the appearance probability of  $\nu_e$  when  $\theta_{13} = 0$  is overlaid with the LBNE beam spectrum used in this study. From the figures, we can see that the probability

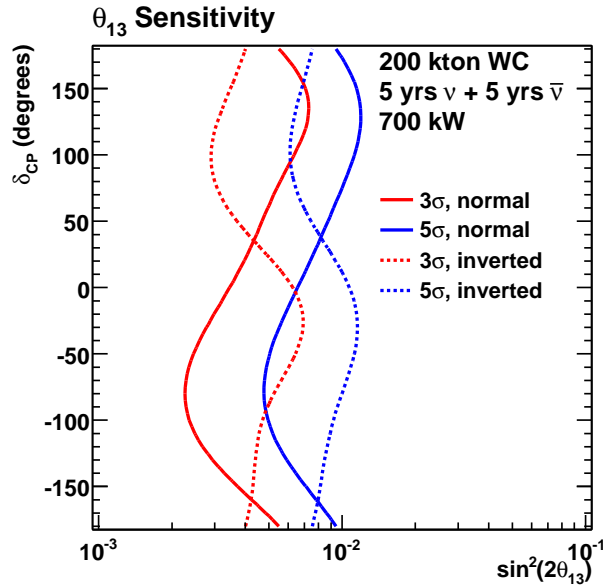


Figure 6-2:  $3\sigma$  (red) and  $5\sigma$  (blue) sensitivity of LBNE to  $\sin\theta_{13} \neq 0$  as a function of  $\delta_{CP}$  for a 200 kton WC detector assuming 5+5 years of  $\nu$  and  $\bar{\nu}$  running in a 700 kW beam. Curves are shown for both normal (solid) and inverted (dashed) mass hierarchies. Here, the discovery reach for  $\sin^2 2\theta_{13}$  is defined as the minimum value of  $\sin^2 2\theta_{13}$  for which LBNE can rule out  $\sin^2 2\theta_{13} = 0$  at the  $3\sigma$  and  $5\sigma$  levels.

of  $\nu_\mu \rightarrow \nu_e$  appearing from mixing in the 1 – 2 sector (solar term) is 1 to 2 % for  $0.5 < E_\nu < 0.8$  GeV when  $\theta_{13} = 0$ . The beam  $\nu_e$  contamination in this energy range is less than  $< 1\%$ . This appearance signal is taken into account properly in estimating the sensitivities to  $\theta_{13} \neq 0$ . For very low values of  $\sin^2 2\theta_{13}$ , LBNE can play a very important role in the study of 3 flavor oscillations, by observing  $\nu_e$  appearance from mixing in the 1 – 2 sectors. All previous and current experiments studying the mixing in the 1 – 2 (solar, reactors) are disappearance experiments (with the exception of SNO, which is an inclusive, rather than exclusive, appearance experiment). The appearance probability in this low energy range is also sensitive to the  $\sin^2 2\theta_{23}$  octant. Currently, using the LBNE LE beam tune, we can expect to see an appearance signal of  $\approx 40 \nu_e$  events in a 200 kt WC detector in the region 0.5 – 2 GeV if  $\theta_{13} = 0$ , assuming a 700 kW beam running for 5 years in neutrino mode. The total background in that region is  $\approx 200$  events (see Figure 6-1).

There is a significant ongoing effort on increasing the neutrino flux in this region ( $< 2$  GeV) as well as reducing the NC backgrounds from higher energy neutrinos by optimizing the LBNE beam target and focusing designs. This should improve the sensitivity to  $\nu_e$  appearance regardless of the value of  $\theta_{13}$ .

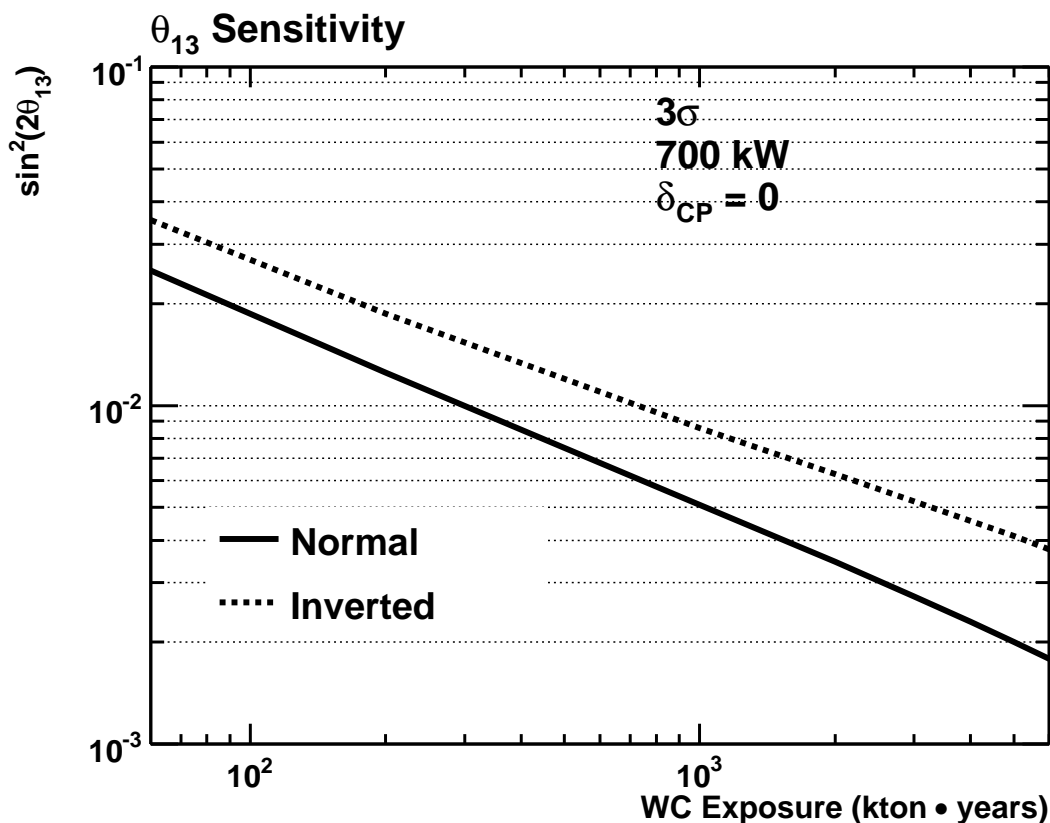


Figure 6–3: Sensitivity of LBNE for determining non-zero  $\theta_{13}$  at the  $3\sigma$  level as a function of exposure for a WC detector with a baseline of 1300 km. The plot gives projections assuming  $\delta_{CP} = 0$  for both normal (solid) and inverted (dashed) mass hierarchies.

### 6.1.3 Mass Hierarchy

While the primary goal of upcoming neutrino oscillation experiments is discovery of  $\theta_{13}$ , they may also provide information on the mass hierarchy and CP violation if  $\theta_{13}$  is large. Nevertheless, the next generation of experiments (like NoVA and T2K) may not be able to resolve these issues even with increased beam power, because of the inherent degeneracies between CP-violating asymmetries and matter effects. An experiment like LBNE is needed to take the next step in physics reach [18].

Figure 6–5 shows LBNE’s projected sensitivity to the mass ordering as a function of  $\theta_{13}$  and  $\delta_{CP}$  for a 200 kton WC detector.

To get a sense for how this changes with detector mass and/or beam power, Figure 6–6 shows the sensitivity for resolving the mass hierarchy as a function of exposure. With an exposure of 2000 kt-yrs, a WC detector can resolve the mass hierarchy at  $3\sigma$  for 100% of all  $\delta_{CP}$  values for a  $\sin^2 2\theta_{13}$  value down to 0.04. The sensitivity improves with larger exposures.

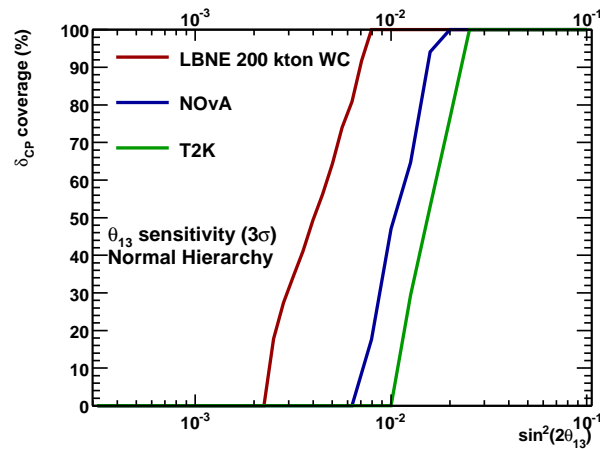


Figure 6–4:  $3\sigma$  sensitivity of LBNE to  $\sin^2 2\theta_{13} \neq 0$  as a function of  $\delta_{CP}$  for a 200 kton WC detector assuming 5+5 years of  $\nu$  and  $\bar{\nu}$  running in a 700 kW beam, compared to the sensitivities of the NO $\nu$ A and T2K experiments, assuming a normal hierarchy. The discovery reach for  $\sin^2 2\theta_{13}$  is defined as the minimum value of  $\sin^2 2\theta_{13}$  for which LBNE can rule out  $\sin^2 2\theta_{13} = 0$  at the  $3\sigma$  and  $5\sigma$  levels.

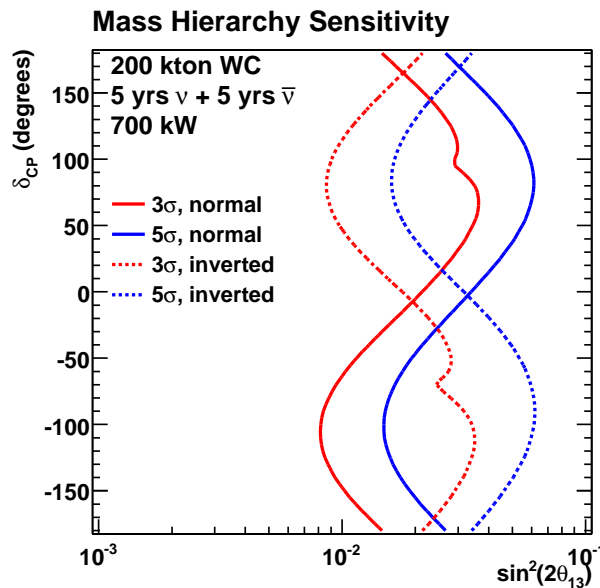


Figure 6–5: Resolution of the mass hierarchy for a 200 kton WC detector assuming 5+5 years of  $\nu$  and  $\bar{\nu}$  running in a 700 kW beam. To the right of the curves, the normal (solid) or inverted (dashed) mass hierarchy can be excluded at the  $3\sigma$  (red) or  $5\sigma$  (blue) level for the indicated values of true  $\sin^2 2\theta_{13}$  and  $\delta_{CP}$ . Here, the mass hierarchy discovery reach is defined as the minimum value of  $\sin^2 2\theta_{13}$  for which the wrong hierarchy can be excluded for a given value of  $\delta_{CP}$ .

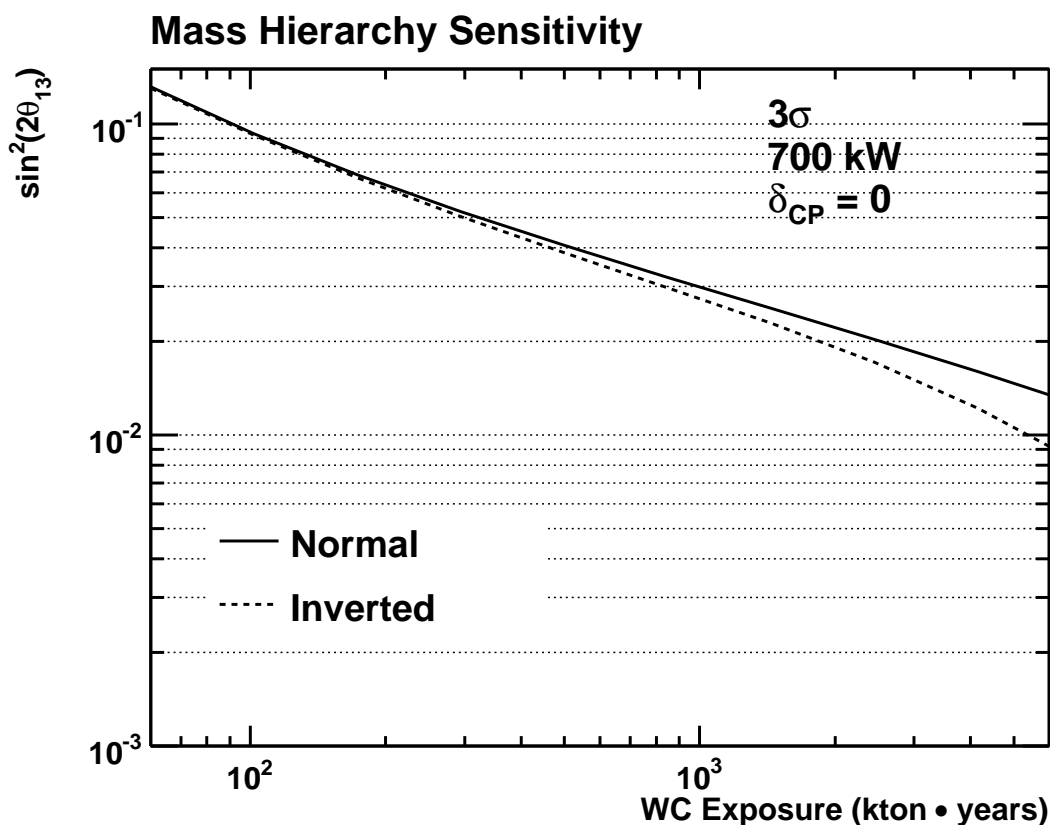


Figure 6-6: Resolution of mass hierarchy for a 200 kton WC detector at  $3\sigma$  as a function of exposure. The plot gives the projections assuming  $\delta_{CP} = 0$  for both normal (solid) and inverted (dashed) mass hierarchies.

Figure 6-7 shows the  $3\sigma$  mass hierarchy ‘discovery’ potential of LBNE in the  $\delta_{CP}$ — $\sin^2 2\theta_{13}$  plane with a 700 kW beam, compared to the NO $\nu$ A experiment and T2K experiments. The NO $\nu$ A and T2K sensitivities were provided to us by Joachim Kopp.

#### 6.1.4 CP Violation

Figure 6-8 summarizes the CP violation reach of LBNE. An LBNE WC detector can make a  $3\sigma$  discovery of CP violation for 50% of all  $\delta_{CP}$  values for  $\sin^2 2\theta_{13}$  values down to 0.03 assuming an exposure of 2000 kt-yrs.

Figure 6-9 shows the resolution on LBNE’s ability to measure  $\delta_{CP}$  as a function of exposure. Assuming a normal mass hierarchy,  $\sin^2 2\theta_{13} = 0.01$ , and  $\delta_{CP} = 0$ , a WC detector can measure  $\delta_{CP}$  to within  $\pm 19^\circ$  (at  $1\sigma$ ) in a 2000 kt-yr exposure. From Figure 6-9, we see that higher mass (or equivalently, higher beam power) provides a rapid improvement in resolution in the early years of running.

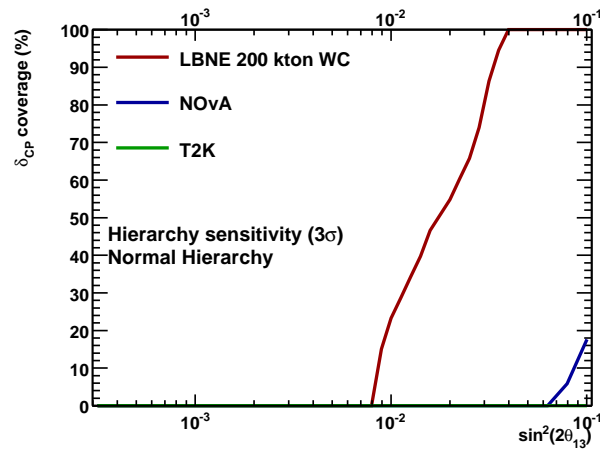


Figure 6–7:  $3\sigma$  sensitivity of LBNE to resolving the mass hierarchy as a function of  $\delta_{CP}$  for a 200 kton WC detector assuming 5+5 years of  $\nu$  and  $\bar{\nu}$  running in a 700 kW beam, compared to the sensitivities of the NO $\nu$ A and T2K experiments, assuming a normal hierarchy.

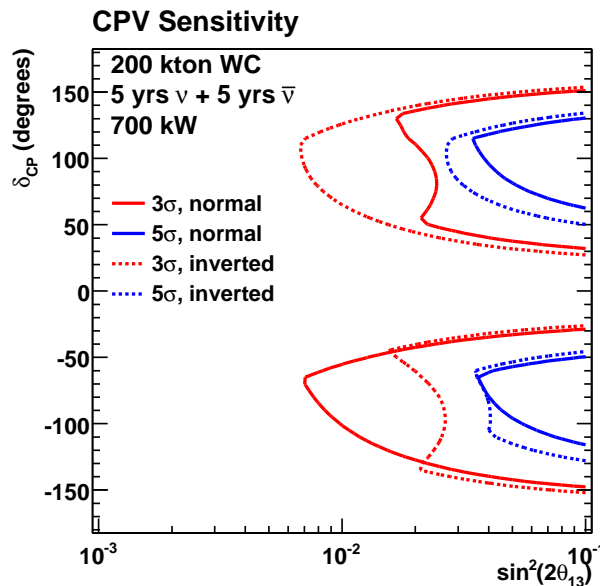


Figure 6–8:  $3\sigma$  (red) and  $5\sigma$  (blue) sensitivity of LBNE to CP violation for a 200 kton WC detector assuming 5+5 years of  $\nu$  and  $\bar{\nu}$  running in a 700 kW beam. Curves are shown for both normal (solid) and inverted (dashed) mass hierarchies. Here, we define the CP violation discovery potential as the range of  $\delta_{CP}$  values as a function of  $\sin^2 2\theta_{13}$  for which one can exclude the CP conserving solutions for  $\delta_{CP} = 0^\circ$  and  $\delta_{CP} = 180^\circ$ .

Figure 6–10 shows the  $3\sigma$  discovery reach for LBNE, compared to the NO $\nu$ A and T2K experiments. As is clear from the figure, neither NO $\nu$ A nor T2K can make a  $3\sigma$  discovery for the values of  $\theta_{13}$  examined here. The sensitivities for NO $\nu$ A and T2K were provided to

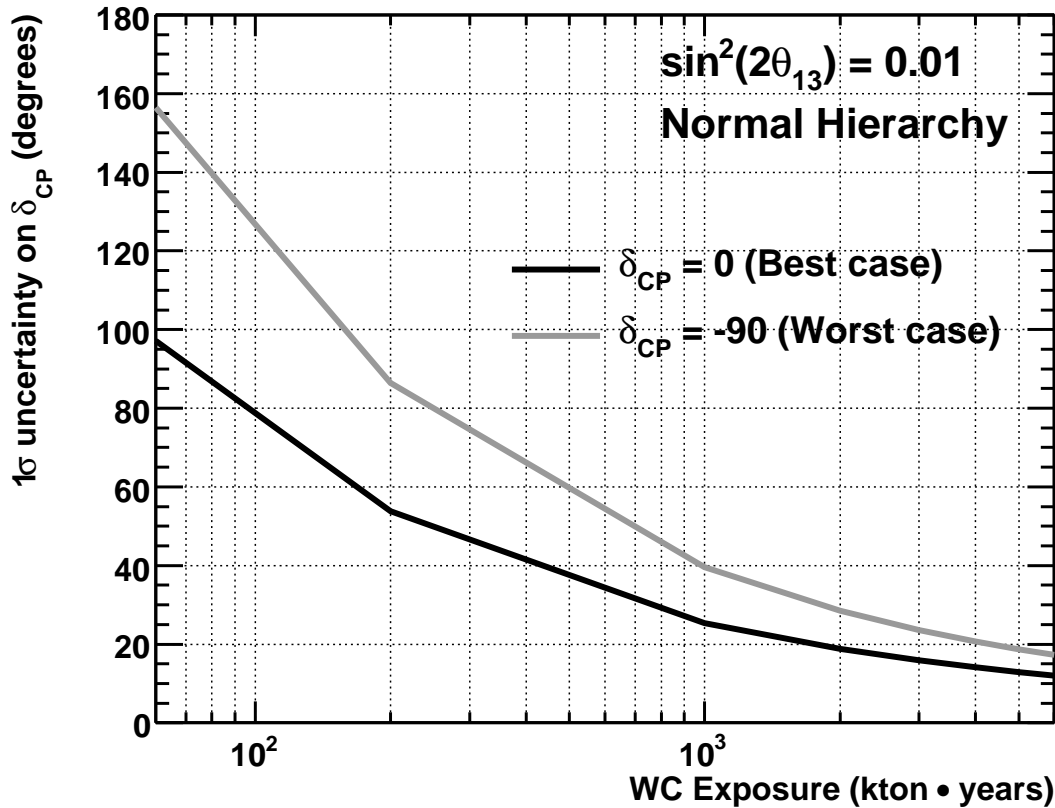


Figure 6-9:  $1\sigma$  resolution on the measurement of  $\delta_{CP}$  in a WC detector assuming  $\sin^2 2\theta_{13} = 0.01$  and normal mass hierarchy. Projections for both  $\delta_{CP} = 0$  (black) and  $\delta_{CP} = -90^\circ$  (gray) are separately shown.

us by Joachim Kopp.

### 6.1.5 Future Improvements

As discussed in Section 5.3, we have been studying improving the sensitivities to the  $\nu_\mu \rightarrow \nu_e$  oscillation parameters by studying the latest improvements to the WC detector response function and optimized efficiency from the T2KK collaboration. The updated Super-K response function from the latest T2KK optimization study [16] significantly increased the  $\nu_e$  signal efficiency in a wider-band beam ( $1^\circ$  off-axis) at a 270 kt WC detector located at a baseline of 1050 km in Korea. The signal and background selection were optimized for the T2KK experiment. For LBNE, we are currently working with T2KK/LBNE collaborators to reoptimize the Super-K response for the higher energy on-axis LBNE beam. The  $\nu_\mu \rightarrow \nu_e$  signal and background event numbers in LBNE with the T2KK WC detector signal and background efficiency numbers are shown in Table 6.1.5. As we can see from these

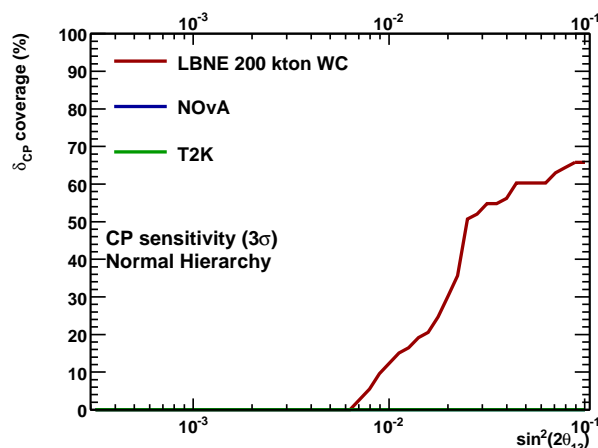


Figure 6–10:  $3\sigma$  discovery reach of LBNE for  $\delta_{CP}$  for a 200 kton WC detector assuming 5+5 years of  $\nu$  and  $\bar{\nu}$  running in a 700 kW beam, compared to the sensitivities of the NO $\nu$ A and T2K experiments, assuming a normal hierarchy.

preliminary studies the efficiency of the  $\nu_e$  signal is increased by a factor 2.3. The background acceptance is high at this signal efficiency, so we are studying varying the T2KK selection criteria to optimize  $S/\sqrt{B}$  for LBNE.

	Oscillated $\nu_e$ Signal	NC+ $\nu_\mu$ CC	Beam $\nu_e$
LBNE 200 kt Detector (default efficiency)	484	291	218
LBNE 200 kt Detector (T2KK efficiency)	1105	1733	362
T2KK 270 kt Detector in Korea	212	200	100

Table 6–2: Number of expected  $\nu_e$  events in the LBNE 200 kt WC detector from 5 years of neutrino running in a 700 kW beam with the default WC detector response extrapolated from Super-K and optimized for low background, compared to the rates obtained with the higher signal efficiency response from the T2KK study [16]. The last line is the expected off-axis event numbers in the 270kt WC detector in Korea in the T2KK experiment from reference [16] - scaled to 700kW, 5 years neutrino running. These numbers assume, normal hierarchy,  $\sin^2 2\theta_{13} = 0.04$  and  $\delta_{CP} = 0$ .

## 6.2 Beam Upgrades

The possibility of a more intense beam, of up to 2 MW [20], could significantly improve the experiment’s sensitivity to  $\nu_e$  appearance physics, with no changes to the detector necessary.

In Figures 6–11 and 6–12 we show the improvements to CP violation coverage,  $\theta_{13}$  sensitivity, and the mass hierarchy, with a 2 MW beam. As can be seen, for CP violation, the 50% coverage point moves downward to near  $\sin^2 2\theta_{13} \approx 0.01$  in this scenario.

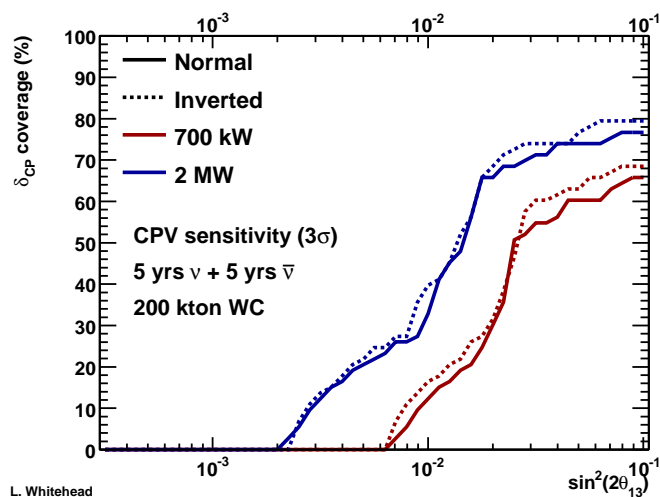


Figure 6–11: Phase coverage for  $3\sigma$  discovery of CP violation, under the assumption of a 2 MW beam.

## 6.3 $\nu_\mu$ and $\bar{\nu}_\mu$ Disappearance

In addition to the  $\nu_e$  appearance measurements, LBNE will also be able to provide precise measurement of the atmospheric oscillation parameters through observation of both  $\nu_{\mu\mu}$  and  $\bar{\nu}_\mu$  disappearance. The most precise constraint on the atmospheric mass splitting is currently set by the MINOS experiment while the most precise constraint on the atmospheric neutrino mixing angle is currently set by the Super-K +experiment.

In the coming years, next generation experiments, such as T2K and NOvA, will be able to push beyond the current values and obtain even more precise measurements of these parameters. For example, with an exposure of  $3.75 \text{ MW} \times 10^7 \text{ sec}$ , T2K hopes to achieve

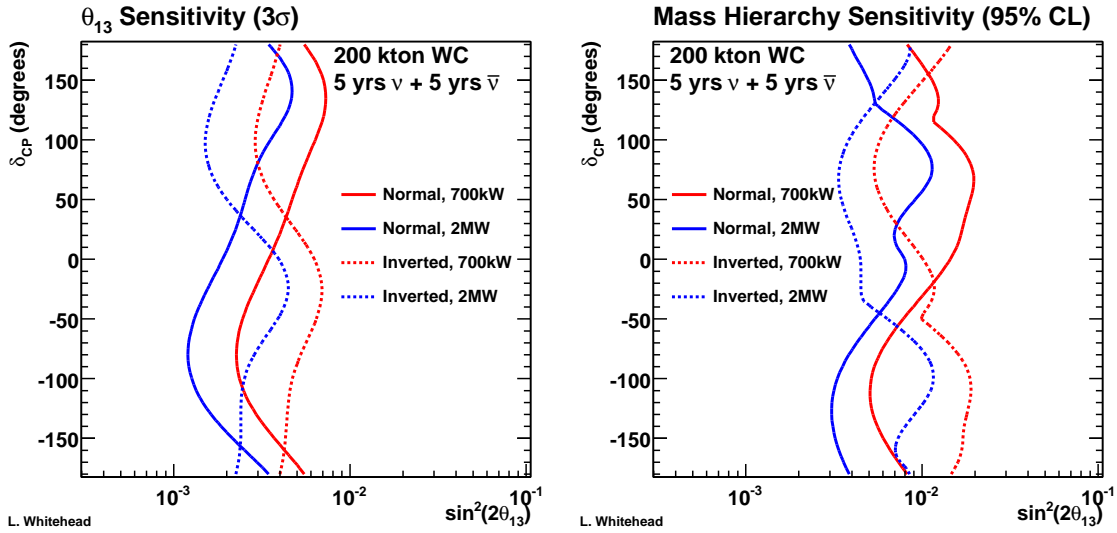


Figure 6-12:  $3\sigma$  discovery reach for  $\sin^2 2\theta_{13}$ , and the mass hierarchy (at 95% C.L.), under the assumption of a 2 MW beam.

a 1% (4%) measurement of  $\sin^2 2\theta_{23}$  ( $\Delta m_{32}^2$ ) [21]. For maximal mixing and after 6 years of  $\nu + \bar{\nu}$  running, NoVA plans to measure  $\sin^2 2\theta_{23}$  to  $\sim 0.3\%$  and  $\Delta m_{32}^2$  to  $\sim 1\%$  [23].

LBNE will also provide a sensitive test of the atmospheric oscillation parameters through its measurement of  $\nu_\mu$  and  $\bar{\nu}_\mu$  disappearance. One advantage of the long baseline in LBNE is that the multiple oscillation pattern in the spectrum will be clearly detectable. This should offer some advantage when it comes to reducing systematics. As such, LBNE should be the first experiment to observe the bi-modal structure in  $\Delta m_{32}^2$  (note that KAMLAND has already observed this for  $\Delta m_{21}^2$ ). Figure 6-13 and Table 6-3 show the expected  $\nu_\mu$  and  $\bar{\nu}_\mu$  event rates at the LBNE far detector site for a 200 kton WC detector. The statistics and the size of the expected signal are large.

Using the assumptions from Section 5.3, Figure 6-14 shows the expected resolutions on  $\sin^2 2\theta_{23}$  and  $\Delta m_{32}^2$  achievable in LBNE as a function of exposure. As can be seen, quick gains are made in the first years of running. In 5 years of neutrino running and for maximal mixing, sub-% level measurements of  $\Delta m_{32}^2$  and  $\sin^2 2\theta_{23}$  are possible (at  $1\sigma$ ) with a 200 kt WC detector. Measurements of these parameters in the antineutrino disappearance channel are also possible at the 1% level assuming a similar exposure.

Table 6-4 summarizes the physics reach of an LBNE WC detector to  $\nu_\mu$  and  $\bar{\nu}_\mu$  disappearance parameters for exposures of both a single 100 kton module and two 100 kton modules to 5 years of 700 kW beam.

	WC ( $\nu$ mode)	WC ( $\bar{\nu}$ mode)
<u>No oscillations:</u>		
QE signal	27,947	18,220
non-QE background	5,884	3,767
wrong-sign background	—	2,725
<u>With oscillations:</u>		
QE signal	8,955	5,500
non-QE background	1,888	1,133
wrong-sign background	—	1,366

Table 6-3: Number of  $\nu_\mu$  and  $\bar{\nu}_\mu$  events expected in a 200 kton WC detector for 5 years each of neutrino and antineutrino running in a 700 kW beam. Rates have been integrated over the region from 0 – 10 GeV. The signal samples are assumed to be  $\nu_\mu$  ( $\bar{\nu}_\mu$ ) QE events in the case of neutrino (antineutrino) mode running. Wrong-sign backgrounds refer to  $\nu_\mu$  events in the antineutrino mode beam.

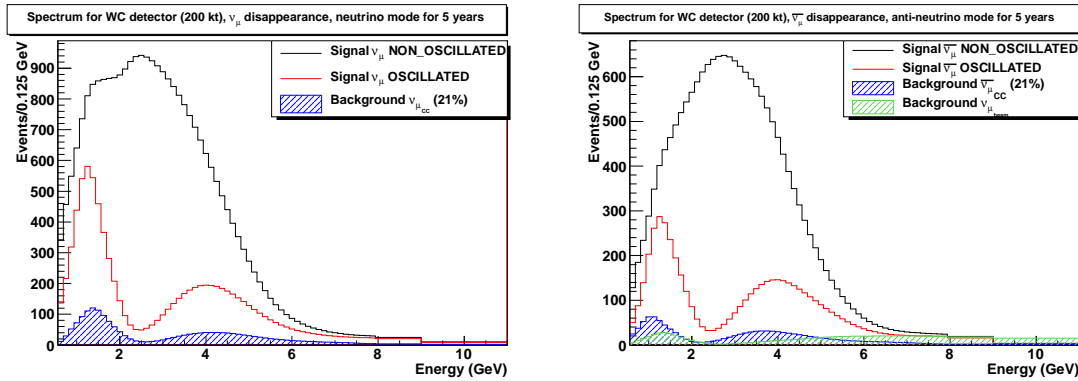


Figure 6-13: Number of events expected with (red) and without (black) oscillations as observed by a 200 kt WC detector in 5 years of neutrino (left) and 5 years of antineutrino (right) running in a 120 GeV 700 kW beam. In the current set of assumptions, a  $\nu_\mu$  QE sample is used for the signal channel. The backgrounds are assumed to be predominantly from CC  $\pi^+$  events. In the case of antineutrino running, there is an additional contribution from  $\nu_\mu$  events which is taken into account and shown in green.

	$\delta(\sin^2 2\theta_{23}) (\nu)$	$\delta(\Delta m_{32}^2) (\nu)$	$\delta(\sin^2 2\theta_{23}) (\bar{\nu})$	$\delta(\Delta m_{32}^2) (\bar{\nu})$
500 kt-yrs WC	0.007	0.019	0.009	0.022
1000 kt-yrs WC	0.005	0.013	0.007	0.015

Table 6-4:  $1\sigma$  resolution on the measurement of  $\nu_\mu$  (and  $\bar{\nu}_\mu$ ) disappearance parameters in LBNE assuming an exposure of 500 and 1000 kt-yrs of WC (e.g., 100 kt or 200 kt of WC in 5 years of  $\nu$  (or  $\bar{\nu}$ ) running at 700 kW). Values are quoted for  $\sin^2 2\theta_{23} = 1.0$ . Units on  $\delta(\Delta m_{32}^2)$  are in  $10^{-3}\text{eV}^2$ .

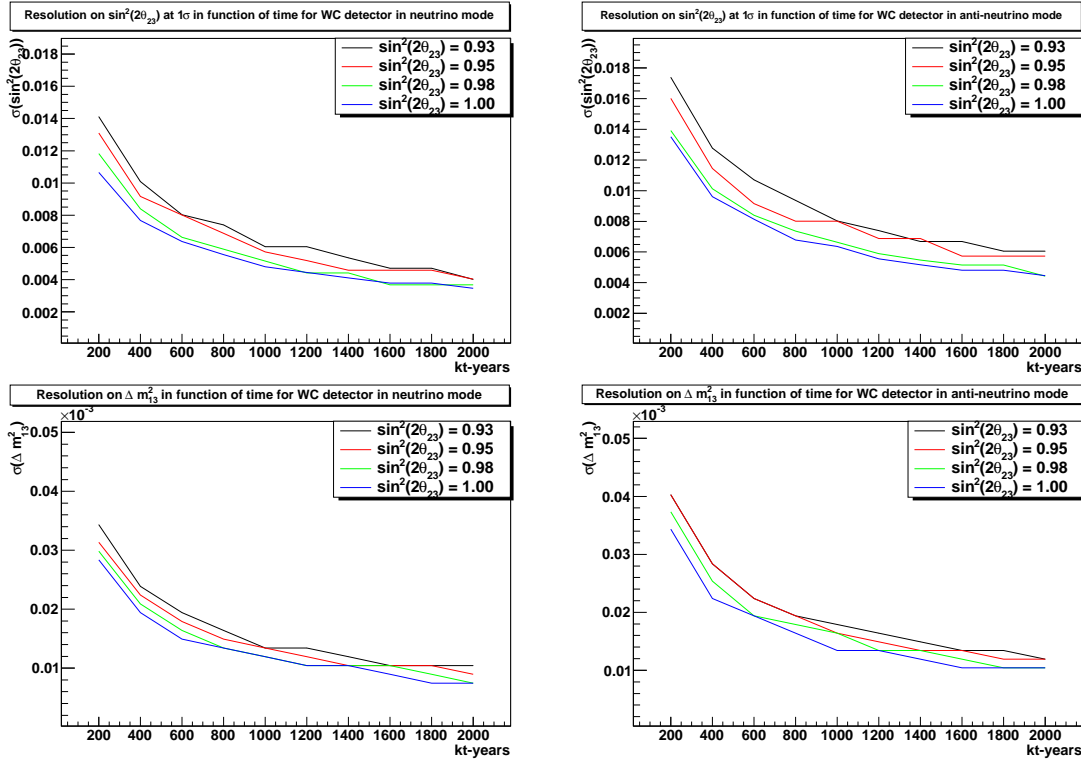


Figure 6–14: Resolution on  $\sin^2 \theta_{23}$  (top) and  $\Delta m_{31}^2$  (bottom) as a function of exposure that could be achieved in LBNE at the  $1\sigma$  level for a WC detector running in neutrino (left) and antineutrino (right) mode assuming a 700 kW beam.

### 6.3.1 Resolving the $\theta_{23}$ Octant

Current experimental results tell us that  $\sin^2 2\theta_{23}$  is near maximal ( $\sin^2 \theta_{23} > 0.91$  at 90% CL [19]), however there exist two solutions of  $\theta_{23}$  for a given set of measured oscillation parameters, known as the  $\theta_{23}$  octant ambiguity. Determining whether  $\theta_{23}$  is greater than or less than  $\pi/4$  will help tell us whether the third neutrino mass eigenstate couples more strongly to  $\nu_\mu$  or  $\nu_\tau$ . Figure 6–15 displays the capability of LBNE to resolve the  $\theta_{23}$  octant with a 200 kt WC detector. LBNE is able to resolve the  $\theta_{23}$  octant degeneracy for  $\theta_{23}$  values less than  $40^\circ$  at 90% CL and 90% of  $\delta_{CP}$  values if  $\sin^2 2\theta_{13}$  is greater than 0.070.

### 6.3.2 $\nu_\tau$ Appearance

The LBNE baseline at 1300 km will be longer than any long-baseline experiment currently in operation. As a result, the oscillation probability occurs at higher energy and in particular the energy range is favorable to  $\nu_\mu \rightarrow \nu_\tau$  appearance since there is a large appearance probability above the  $\tau$  CC production threshold of 3.4 GeV. In this respect LBNE has a unique ability compared to current long-baseline experiments, since oscillation between all

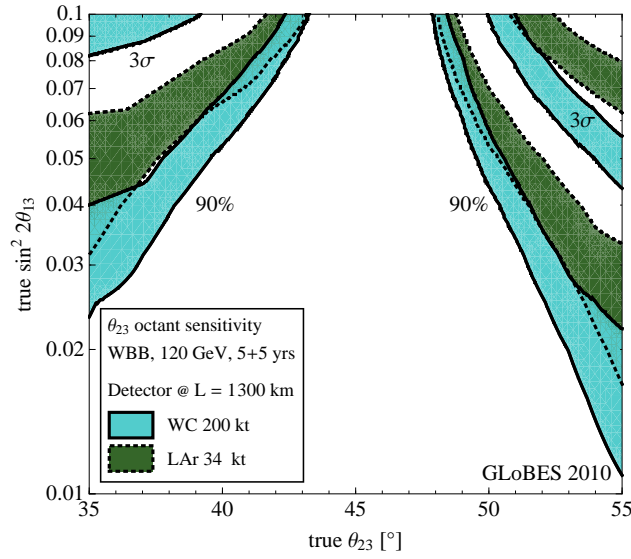


Figure 6–15: Sensitivity of LBNE to resolve the  $\theta_{23}$  octant degeneracy for 5+5 years of  $\nu+n\bar{u}$  running at 700 kW and normal mass hierarchy. The blue band shows the results for 200 kt WC and the green for 34 kt LAr. The width of the bands corresponds to the impact of different true values for  $\delta_{CP}$ , ranging from a 10% to 90% fraction of  $\delta_{CP}$ . In the region above the bands, the determination of the  $\theta_{23}$  octant is possible at 90% CL (lower bands) and  $3\sigma$  (upper bands).

three flavors of neutrinos can be observed with significant statistics in a single experiment. To increase the  $\nu_\tau$  CC appearance signal, we are considering several high energy beam tunes produced by moving the target further upstream of horn 1. The Super-K collaboration has recently announced the observation of a  $\nu_\tau$  signal from atmospheric oscillations [22]. We are currently estimating the statistical significance with which  $\nu_\tau$  appearance can be established in the LBNE WC detector.

In Table 6–5, the  $\nu_e$  and  $\nu_\tau$  CC appearance rates for several LBNE beam tunes are shown.

Target Position	$\nu_\mu$ CC	$\nu_\mu$ CC osc	$\nu_e$ CC beam	$\nu_\mu \rightarrow \nu_e$ CC	$\nu_\mu \rightarrow \nu_\tau$ CC
0	20K	7.8K	220	400	100
-0.3 m	29K	11K	260	560	140
-1.5 m	44K	28K	320	480	640
-2.5 m	47K	35K	280	340	800

Table 6–5:  $\nu_\mu, \nu_\tau, \nu_e$  appearance rates per 100 kt.MW.yr at the far detector in LBNE for different beam tunes obtained by moving the target w.r.t. horn 1. Normal hierarchy,  $\sin^2 2\theta_{13} = 0.04, \delta_{cp} = 0$ . The rates are integrated in the region 0-20 GeV.

## 6.4 Neutrino Physics Beyond Standard Mixing

In addition to precision measurements of the standard three-flavor neutrino oscillation parameters, LBNE is also well-suited for new physics searches in the neutrino sector. For example, the experiment is sensitive to non-standard neutrino interactions and active-sterile neutrino mixing, provided that these effects are not too weak.

### 6.4.1 Non-standard Interactions

Theories beyond the Standard Model can induce Lagrangian operators that couple neutrinos to normal matter in non-standard ways. In the low-energy effective theory relevant to neutrino oscillation experiments, these non-standard interactions manifest themselves as 4-fermion operators, either of the charged current (CC) type or of the NC type. NC NSI can be understood as non-standard matter effects that are visible only in a far detector at a sufficiently long baseline. This is where LBNE has a unique advantage compared to other long-baseline experiments (except atmospheric neutrino experiments, which are, however, limited by systematic effects, and solar neutrino experiments that probe a different region of parameter space). They can be parameterized as new contributions to the MSW matrix in the neutrino propagation Hamiltonian:

$$H = U \begin{pmatrix} 0 & & \\ & \Delta m_{21}^2/2E & \\ & & \Delta m_{31}^2/2E \end{pmatrix} U^\dagger + \tilde{V}_{\text{MSW}}, \quad (6.1)$$

with

$$\tilde{V}_{\text{MSW}} = \sqrt{2}G_F N_e \begin{pmatrix} 1 + \epsilon_{ee}^m & \epsilon_{e\mu}^m & \epsilon_{e\tau}^m \\ \epsilon_{e\mu}^{m*} & \epsilon_{\mu\mu}^m & \epsilon_{\mu\tau}^m \\ \epsilon_{e\tau}^{m*} & \epsilon_{\mu\tau}^{m*} & \epsilon_{\tau\tau}^m \end{pmatrix}. \quad (6.2)$$

Here,  $U$  is the leptonic mixing matrix, and the  $\epsilon$ -parameters give the magnitude of the NSI relative to standard weak interactions. For new physics scales of few  $\times 100$  GeV, we expect  $|\epsilon| \lesssim 0.01$ . Model-independent bounds on NSI are typically of order 0.01–1 [26,27,28]. To assess the sensitivity of LBNE to NC NSI, we define the NSI discovery reach in the following way: We simulate the expected event spectra, assuming given “true” values for the NSI parameters, and then attempt a fit assuming no NSI. If the fit is incompatible with the simulated data at a given confidence level, we say that the chosen “true” values of the NSI parameters are within the experimental discovery reach. In Fig. 6–16, we show the NSI discovery reach of LBNE for the case where only one of the  $\epsilon_{\alpha\beta}^m$  parameters is non-negligible at a time.

We conclude from the figure that LBNE will be able to improve model-independent bounds on NSI in the  $e$ - $\mu$  sector by a factor of 2, and in the  $e$ - $\tau$  sectors by an order

### NC NSI discovery reach ( $3\sigma$ C.L.)

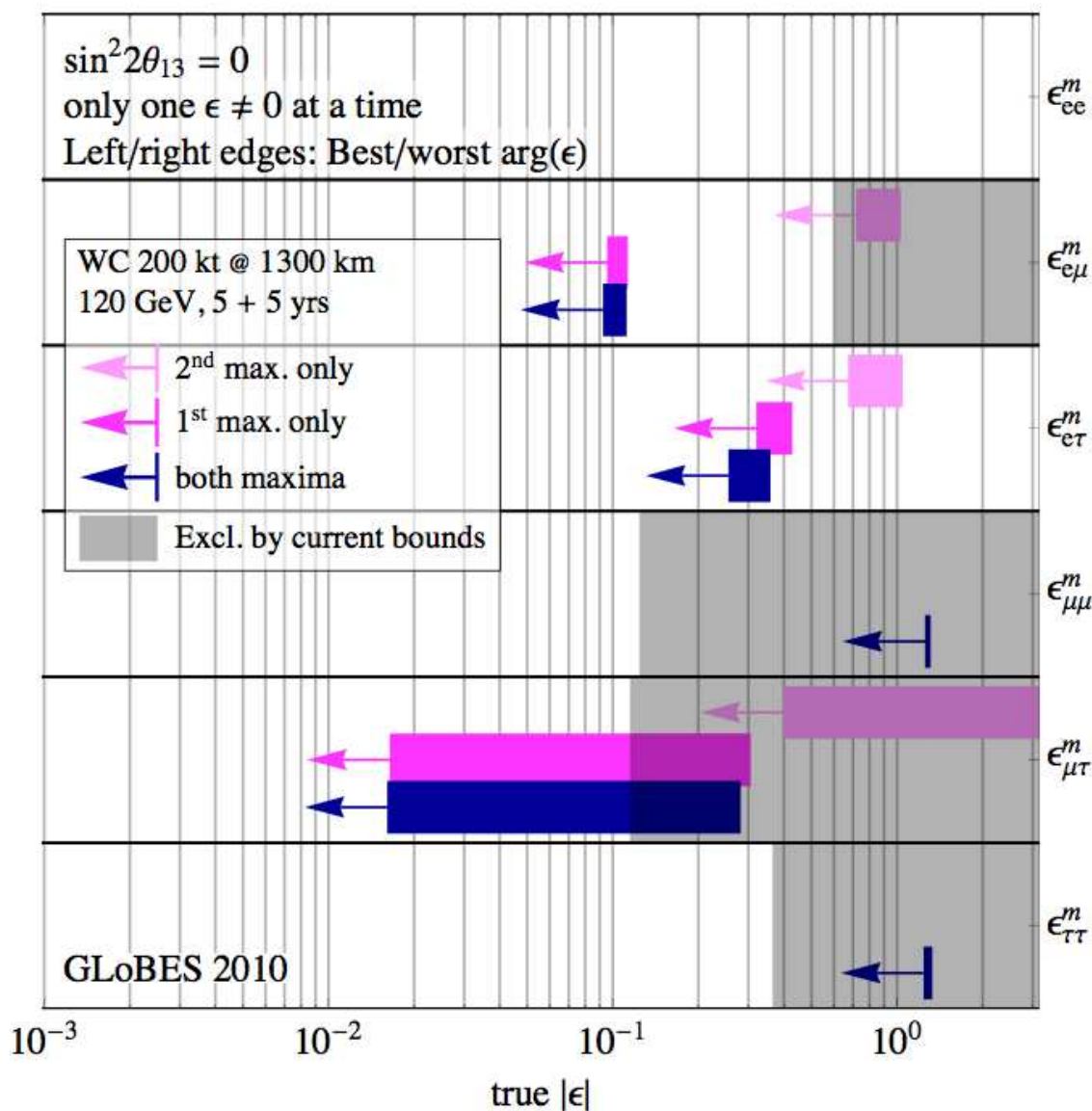


Figure 6-16: NSI discovery reach in a 200kt WC detector. The left and right edges of the error bars correspond to the most favorable and the most unfavorable values for the complex phase of the respective NSI parameters. Red arrows indicate the current model-independent limits on the different parameters at  $3\sigma$  [26,27,28].

of magnitude. Bounds on non-standard effects in the  $\mu$ - $\tau$  sector are already quite strong because of the sensitivity of atmospheric neutrino experiments, but LBNE may be able to improve also some of the bounds in this sector, and in any case, LBNE bounds will be more robust than the ones derived from atmospheric neutrino oscillations [35].

### 6.4.2 Long Range Lepton Flavor Interactions

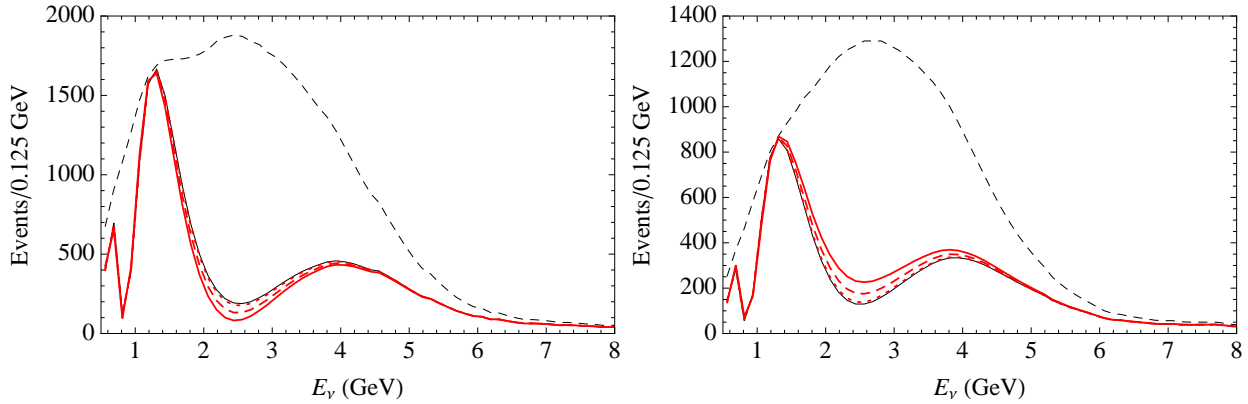


Figure 6–17: The number of  $\nu_\mu$  (left) and  $\bar{\nu}_\mu$  (right) CC interactions in a 200 kton detector located at 1300 km from the LBNE beam for  $\sin^2 2\theta_{23} = 0.9$ ,  $\Delta m_{32}^2 = 2.4 \times 10^{-3} \text{ eV}^2$ . The experiment assumes 5+5 yrs of running in neutrino+anti-neutrino mode at 700 kW. The dashed black line is the unoscillated interaction rate, the solid black line is the oscillated spectrum with no new physics. The red curves are the oscillated spectra with LRI with  $\alpha' = 1.0, 0.5, 0.1 \times 10^{-52}$  (thick solid, dashed, and dotted) [37].

LBNE will be able to measure the oscillation of  $\nu_\mu \rightarrow \nu_\tau$  and  $\bar{\nu}_\mu \rightarrow \bar{\nu}_\tau$  with a precision that exceeds any previous or currently planned long-baseline neutrino oscillation experiments. The expected precision is  $< 1\%$  on the mass-difference squared, and  $\sin^2 2\theta_{23}$ . Long range lepton flavor interactions (LRI) caused by the collective effect of particles in the Sun and the Earth can manifest themselves as a difference in  $\nu_\mu/\bar{\nu}_\mu$  oscillations in terrestrial neutrino experiments [37]. The precision measurement of  $\nu_\mu$  disappearance in both neutrinos and anti-neutrinos using a wide-band beam in LBNE, make it a unique laboratory to explore long range lepton flavor interactions. The strength of the LRI interaction is given by an effective fine structure constant  $\alpha'$ , whose values are constrained to be in the range  $\leq \mathcal{O}(10^{-49} - 10^{-47})$  by precision measurements of gravity. Figure 6–17 displays the oscillated  $\nu_\mu$  and  $\bar{\nu}_\mu$  spectra expected in a 200 kt LBNE detector with different values of  $\alpha' \leq 10^{-52}$ . The large mass of the WC detector coupled with the excellent  $\nu_\mu$  PID capabilities and excellent energy resolution achievable with large statistics of QE events (see Figure 6–13) indicate that LBNE is sensitive to small asymmetries in the oscillations of neutrinos and anti-neutrinos at a level sufficient to probe current models of long-range interactions with effective coupling constants at least an order of magnitude below that excluded by precision tests of gravity.

## 6.5 Variation of Physics Sensitivities with Baseline

We have studied the impact of the baseline on oscillation physics sensitivities with a 200 kt WC detector assuming 5+5 years of  $\nu$  and  $\bar{\nu}$  running in a 120 GeV 700 kW beam. To try and keep L/E near the optimal for each baseline, we considered 3 different beam tunes: i) a narrow band  $2^\circ$  off-axis beam similar to the T2K beam for baselines of 300 and 500 km, ii) the default LE wide-band on-axis beam for baselines from 500 to 2000 kms, and iii) the ME wide-band beam tune for baselines greater than 2000 km. The beam spectra are shown in Figure 5-1. The results of the sensitivity vs baseline studies are shown in Figure 6-18 for the  $\nu_\mu \rightarrow \nu_e$  oscillation physics.

From the study, we observe that for a normal hierarchy the  $3\sigma$  sensitivity to  $\theta_{13} \neq 0$  at  $\delta_{cp} = 0$  with a 200kt WC detector is almost constant as a function of baseline (300-3000km) with the best matched beam tune and is achieved for values of  $\sin^2 2\theta_{13}$  between 0.003 and 0.0045. The statement is not true for the inverted hierarchy, where the sensitivity to non-zero  $\theta_{13}$  is usually worse for the same beam tune compared to the normal hierarchy. The studies show that we can resolve  $\theta_{13} \neq 0$  at  $\delta_{cp} = 0$  for both mass hierarchies for  $\sin^2 2\theta_{13} \leq 0.006$  using the same wide-band beam tune for baselines  $\geq 1300$  km. For the sensitivity to the mass hierarchy at  $3\sigma$  for at  $\delta_{cp} = 0$ , the sensitivity for both normal and inverted hierarchy is almost identical and improves rapidly with baseline until a baseline of around 1500 where it begins to plateau. The MH sensitivity is achieved for values of  $\sin^2 2\theta_{13}$  between 0.015 to 0.006 for baselines from 1500km to 3000km respectively. The  $1\sigma$  resolution of the measurement  $\delta_{cp}$  at  $\delta_{cp} = 0$  as a function of baseline demonstrates that the best resolution of  $\leq 20^\circ$  is achieved at baselines between 1000 to 1500km. While the resolution of this one point is also  $\leq 20^\circ$  for baselines  $\leq 500$ km, we cannot resolve the parameter degeneracies with baselines shorter than 1000km. The  $1\sigma$  resolution of the measurement  $\delta_{cp}$  at  $\delta_{cp} = 0$  gets significantly worse at baselines  $> 2000$  km.

We conclude that to obtain the best sensitivity to  $\theta_{13} \neq 0$ , resolving the mass hierarchy, and measuring the oscillation parameters - particularly  $\delta_{cp}$  - with the highest precision in the same experiment with the same beam requires baselines between 1300 and 1700 km.

## 6.6 Summary of Long-Baseline Physics Capabilities

LBNE is sensitive to non-zero  $\theta_{13}$  (at the  $3\sigma$  level) down to  $\sin^2 2\theta_{13} = 0.005$  for a single 100 kton WC module operating for 10 years (5+5 years  $\nu + \bar{\nu}$ ) and down to  $\sin^2 2\theta_{13} = 0.003$  for 200 ktons operating in this same time. This assumes  $\delta_{CP} = 0$  and normal mass hierarchy (Figure 6-3). As one might expect, the 200 kton configuration reaches a sensitivity almost a factor of two higher than the 100 kton case; of course, higher beam power could also provide the same sensitivity in the case of a smaller detector. Additionally, the 1000 kton-yr exposure provides a  $25^\circ$  measurement of  $\delta_{CP}$ , whereas an  $19^\circ$  accuracy can be achieved in

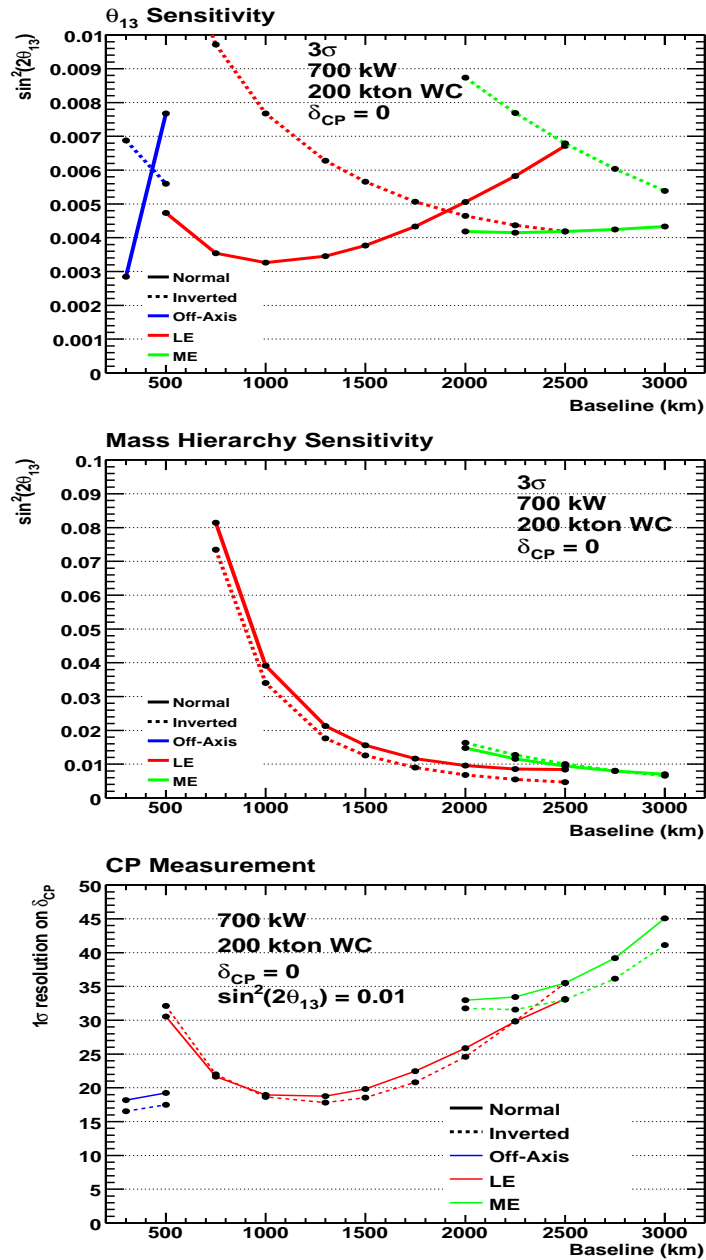


Figure 6-18: The physics sensitivities of a 200kt WC detector vs baseline and  $\sin^2 2\theta_{13}$  assuming 5+5 years of  $\nu$  and  $\bar{\nu}$  running in a 700 kW beam. The different colors correspond to different beam spectra used as shown in Figure 5-1. The top figure is the  $3\sigma$  discovery reach for  $\theta_{13} \neq 0$ , at  $\delta_{CP} = 0$ . The middle figure is the sensitivity at  $3\sigma$  to the mass hierarchy resolution at  $\delta_{CP} = 0$ . The bottom figure shows the  $1\sigma$  resolution on  $\delta_{CP}$ , at  $\delta_{CP} = 0$ . The solid lines are for normal hierarchy and the dotted lines are for inverted hierarchy.

2000 kton-yrs. This assumes normal mass hierarchy,  $\sin^2 2\theta_{13} = 0.01$ , and  $\delta_{CP} = 0$ . Figure

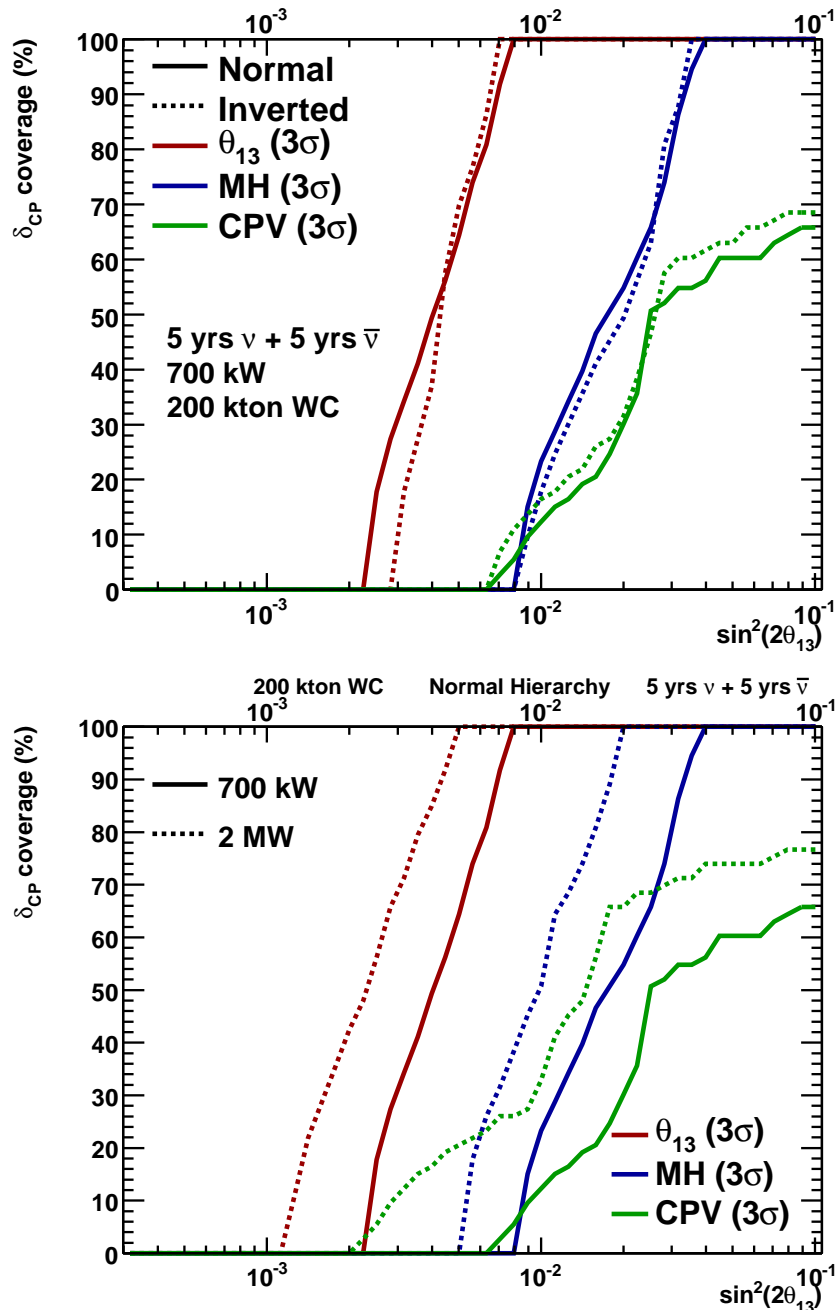


Figure 6–19:  $3\sigma$  discovery potential of LBNE for determining  $\sin^2 2\theta_{13} \neq 0$ , the mass hierarchy (blue), and CP violation (green) as a function of  $\sin^2 2\theta_{13}$  and the fraction of  $\delta_{CP}$  coverage. In the top figure, the sensitivities are shown for both normal (solid) and inverted (dashed) mass hierarchies for a 200 kton WC detector in 5+5 years of  $\nu + \bar{\nu}$  running in a 700 kW beam. The bottom figure shows the discovery potential for 5+5 yrs running with a 700 kW (solid) and 2 MW (dashed) beam at normal hierarchy.

6-19 summarizes the value of  $\sin^2 2\theta_{13}$  at which  $3\sigma$  sensitivity can be achieved as a function of the fraction of  $\delta_{CP}$  values covered. The sensitivity is shown for 10 yrs of running in both a 700 kW beam and a 2 MW beam, such as could be available from the proposed ProjectX at Fermilab [20]. Table 6-6 summarizes the sensitivity of a WC detector in LBNE to measure non-zero  $\sin^2 2\theta_{13}$ , the mass hierarchy, and CP violation assuming a run time of 5 years each in neutrino and antineutrino modes at 700 kW for detectors with masses of 100 kton, 150 kton, and 200 kton. We also considered the case where a 2MW ProjectX beam at 120 GeV coupled with a 200 kton WCD detector. We find that the greatest impact of the detector

	$\sin^2 2\theta_{13} \neq 0$	Mass Hierarchy	CP violation
1000 kt-yrs WC (700kW)	0.010	0.06	0.09
1500 kt-yrs WC (700kW)	0.009	0.05	0.06
2000 kt-yrs WC (700kW)	0.008	0.04	0.03
2000 kt-yrs WC (2MW)	0.005	0.02	0.015

Table 6-6: Sensitivity comparisons for 1000 kt-yr, 1500 kt-yr, and 2000 kt-yr exposures of a WC detector (e.g., 100 kton, 150 kton, 200 kton) of WC in 5+5 years of  $\nu + \bar{\nu}$  running at 700 kW and for 2000 kt-yr at 2 MW. These numbers represent the value of  $\sin^2 2\theta_{13}$  where a  $3\sigma$  determination of  $\sin^2 2\theta_{13} \neq 0$ , the sign of  $\Delta m_{31}^2$ , and CP violation can be made for 100% of the possible values of  $\delta_{CP}$ . For CP violation, the values are quoted for 50% of possible  $\delta_{CP}$  values. All assume a normal mass hierarchy.

mass is on the sensitivity to CP violation with large gains in sensitivity (larger than expected from simple statistics) as the detector mass is increased. Figure 6-20, shows the impact of the detector mass on the sensitivity to CPV as a function of  $\delta_{CP}$  and  $\sin^2 2\theta_{13}$ .

From the study of the sensitivity variations with baseline and detector mass, we conclude that best sensitivities to the  $\nu_\mu \rightarrow \nu_e$  oscillation parameters - including the ability to carry out precision measurements of the CP phase and  $\theta_{13}$  for values of  $\sin^2 2\theta_{13} > 0.01$  - requires a wide-band beam coupled to baselines between 1300 and 1700km and a WC detector of at least 200 kton in mass.

LBNE will also actively search for new physics manifesting itself as non-standard matter effects and has enhanced sensitivity due to the very long baseline of the experiment. LBNE will be able to improve model-independent bounds on NSI in the  $e-\mu$  sector by a factor of 2, and in the  $e-\tau$  sectors by an order of magnitude.

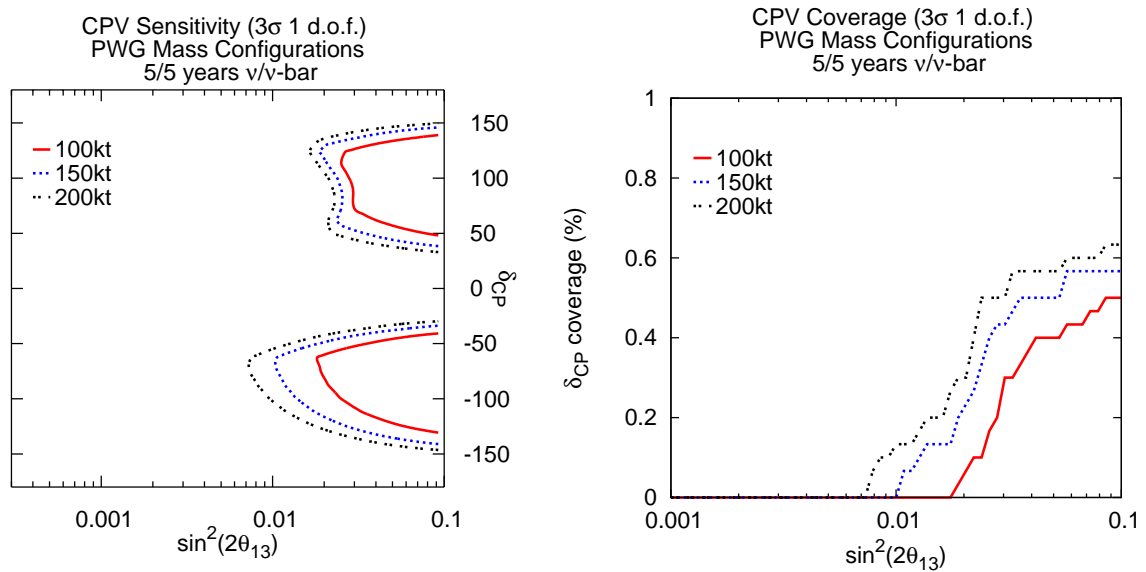


Figure 6–20: The sensitivity of a 100, 150, and 200 kton WC detector at 1300km to CP violation at  $3\sigma$ . The plot on the left is the  $3\sigma$  sensitivity contour as a function of  $\delta_{cp}$  and  $\sin^2 2\theta_{13}$ . The plot on the right is the  $3\sigma$  sensitivity as a function of  $\sin^2 2\theta_{13}$  and the fraction of  $\delta_{CP}$  coverage. The experiment assumes 5+5 years of  $\nu$  and  $\bar{\nu}$  running in a 700 kW beam.

## 7 Proton Decay

Proton decay, bound neutron decay, and similar processes such as dinucleon decay and neutron-antineutron oscillation test the apparent but unexplained conservation law of baryon number. These decays are already known to be rare based on decades of prior searches, all of which have been negative. If measurable event rates or even single candidate events are found, one immediately concludes that they must have proceeded via unknown virtual processes based on physics beyond the standard model. The impact of demonstrating the existence of a baryon number violating process would be profound.

The class of theories known as Grand Unified Theories (GUTs) make predictions about baryon number violation and the life of the proton that may be within reach of the LBNE detectors. Early GUTs were the original motivation for putting kiloton-scale detectors underground. The 22.5 kiloton Super-Kamiokande experiment extended the search for proton decay by more than an order of magnitude. Although there has been no sign of proton decay, the strict limits from these experiments constrain the construction of contemporary GUTs and indeed, a tension between experiment and theory is now commonly discussed. It is very natural to continue the search with 100-kiloton-scale detectors.

### 7.1 Motivation and Scientific Impact of Future Measurements

The grand unified theoretical motivation for the study of proton decay has a long and distinguished history [38,39,40], and has been reviewed many times [41,42,43]. Contemporary reviews [44,45,46] discuss the strict limits already set by Super-Kamiokande and the context of proposed multi-100-kiloton scale experiments such as Hyper-Kamiokande and LBNE. Here are some of the key points related to scientific impact:

- Conservation of baryon number is unexplained, corresponding to no known long-range force.

- Baryon number non-conservation has cosmological consequences, such as a role in inflation and the baryon asymmetry of the universe.
- Proton decay is predicted by a wide range of GUTs.
- Grand unified theories are also often able to accommodate massive neutrinos with characteristics as discovered over the last decade.
- GUTs incorporate other unexplained features of the standard model such as the relationship of quark and lepton electric charges.
- The unification scale is suggested experimentally and theoretically by the apparent convergence of the running coupling constants of the Standard Model. It is in excess of  $10^{15}$  GeV.
- The unification scale is not accessible by any accelerator experiment, and can only be probed by virtual processes such a proton decay.
- The dominant proton decay mode is often sufficient to roughly identify the likely characteristics of the GUT, such as gauge mediation or the involvement of supersymmetry.
- GUTs usually predict the relative branching fractions of different nucleon decay modes, requiring a sizeable sample of proton decay events to more fully explore.

In summary, the observation of even a single unambiguous proton decay event would strongly corroborate that the ideas of unification are correct and would give strong guidance as to which ideas are correct. One or two events would also give guidance to the larger size detector needed to explore the physics in more detail.

From the body of literature, two decay modes emerge that dominate our experimental design. First, there is the decay mode of  $p \rightarrow e^+\pi^0$  that arises from gauge mediation. This is the most famous proton decay mode, often predicted to have the highest branching fraction, and also demonstrably the most straightforward experimental signature for a water Cherenkov detector. The total mass of the proton is converted into the electromagnetic shower energy of the positron and the two photons from  $\pi^0$  decay, with a net momentum vector near zero.

The second key mode is  $p \rightarrow K^+\nu$ . This mode is dominant in most supersymmetric GUTs, which also often favor several other modes involving kaons in the final state. The decay mode with a charged kaon is notable because it presents the unique opportunity for a liquid argon TPC or a scintillation detector to detect it with high efficiency, although water Cherenkov detectors can search for it with 10-15% efficiency and maintain relatively low background rates. We discuss the sensitivity to this mode with a ‘scintillator fill’ of the LBNE water Cherenkov detector, in Section 11.5.1.

There are a number of other proton decay channels to consider, but they will not influence the design of a next-generation experiment beyond the above decay modes. There are 27 allowed modes of proton or bound neutron into anti-lepton plus meson (conserving  $B - L$ ). The most stringent limits besides  $p \rightarrow e^+\pi^0$  include  $p \rightarrow \mu^+\pi^0$  and  $p \rightarrow e^+\eta$ , both of which must have partial lifetimes greater than  $4 \times 10^{33}$  years. Any experiment that will do well for  $e^+\pi^0$  will do well for these decay modes. The decay  $p \rightarrow \nu\pi^+$  or  $n \rightarrow \nu\pi^0$  may have large theoretically predicted branching fractions but are experimentally difficult due to sizeable backgrounds from atmospheric neutrino interactions. The decay  $p \rightarrow \mu^+K^0$  is detected relatively efficiently by either water Cherenkov or LAr TPC detectors. There are a number of other possibilities such as modes that conserve  $B + L$ , or violate only baryon number, or that decay into only leptons. These possibilities are less well-motivated theoretically, as they do not appear in a wide range of theories. In any case, they can be accommodated with equal ease or difficulty by a large water Cherenkov detector.

Figure 7-1 shows experimental limits, dominated by recent results from Super-Kamiokande, compared to the ranges of lifetimes predicted by an assortment of GUTs. At this time, the theory literature does not include attempts to precisely predict lifetimes, concentrating instead on suggesting the dominant decay modes and relative branching fractions. The uncertainty in the lifetime predictions come from details of the theory, such as unknown heavy particles masses and coupling constants, as well as poorly known details of matrix elements for quarks within the nucleon.

It is apparent from this figure that a continued search for proton decay is by no means assured of success. In addition to the lifetime ranges shown, there are models that predict essentially no proton decay or lifetimes out of reach of likely experiments. With that caveat, an experiment with sensitivity between  $10^{33}$  and  $10^{35}$  years is searching in the right territory over a wide range of GUTs and even if no proton decay is detected, the stringent lifetime limits will restrict efforts to build grand unified theories. Minimal SU(5) was ruled out by the early work of IMB and Kamiokande; minimal SUSY SU(5) is considered to be ruled out by Super-Kamiokande. In most cases, another order of magnitude in limit will not rule out specific theories, but will constrain their allowed parameters, perhaps leading to the conclusion that some are fine-tuned.

## 7.2 Sensitivity of Reference Configurations

The experimental requirements of the search for proton decay can be found in the basic formula for the partial lifetime  $\tau$  for branching fraction  $B$ :

$$\frac{\tau}{B} = \frac{N_0 \Delta t \epsilon}{n_{obs} - n_{bg}}, \quad (7.1)$$

where  $N_0$  is the number of nucleons exposed,  $\Delta t$  is the exposure time,  $\epsilon$  is the detection efficiency,  $n_{obs}$  is the observed number of events, and  $n_{bg}$  is the estimated number of background

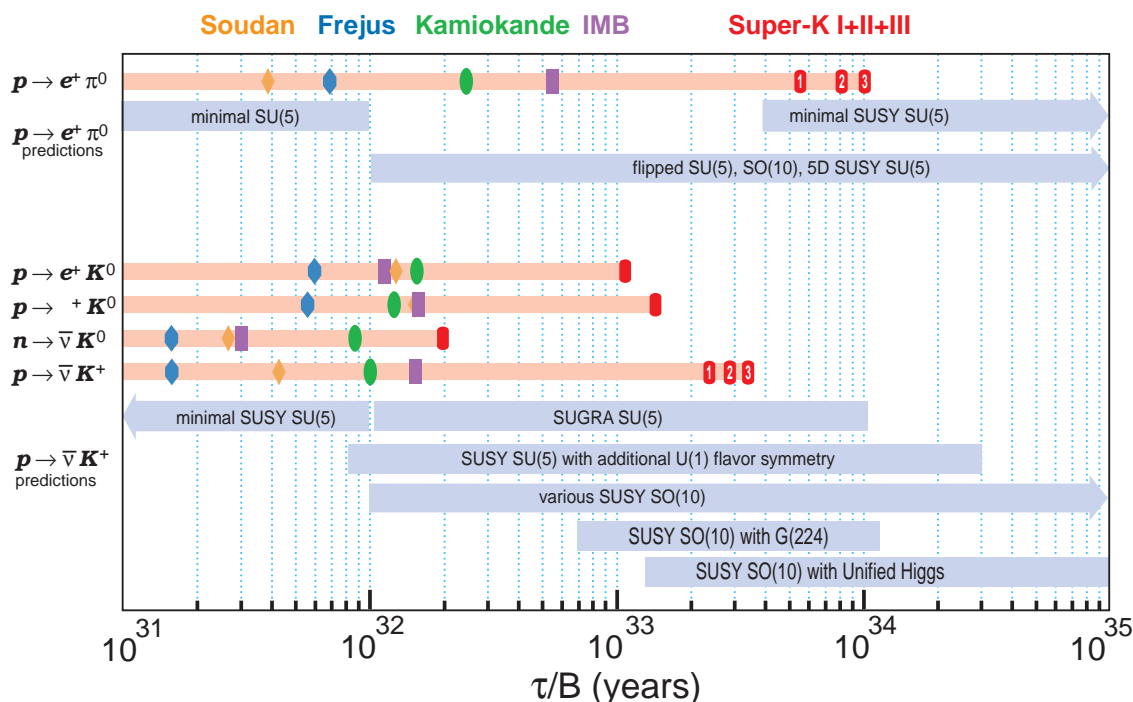


Figure 7-1: Proton decay lifetime limits compared to lifetime ranges predicted by Grand Unified Theories. The upper section is for  $p \rightarrow e^+ \pi^0$ , most commonly caused by gauge mediation. The lower section is for SUSY motivated models, which commonly predict decay modes with kaons in the final state. The marker symbols indicate published limits by experiments, as indicated by the sequence and colors on top of the figure.

events. To measure  $\tau/B$ , one would like the numerator to be as large as possible, which calls for the largest possible exposure of nucleons as well as the highest possible efficiency.

The sensitivity for a detector configuration is determined by the detector mass, efficiency, expected background, and running time, following Eq. 7.1. For the purpose of generating sensitivity curves, we calculate the 90% C.L. lifetime limit one would publish after a given exposure under the assumption that the number of detected events exactly equals the number of background events, and the background is subtracted. The efficiency and background estimates are drawn from Table 7-1.

The lifetime limit is calculated for the 90% confidence level based on the Poisson processes with background method from the 1996 Review of Particle Properties [48]. This method does not take into account systematic uncertainty; doing so typically weakens these limits by 20%.

Mode	Efficiency	Background Rate (evts/100 kt-y)
$p \rightarrow e^+\pi^0$	$45\% \pm 19\%$	$0.2(\pm 40\%)$
$p \rightarrow \nu K^+$	$13.4\% \pm 22\%$	$0.67(\pm 30\%)$ (SK1)
$p \rightarrow \nu K^+$	$10.6\% \pm 22\%$	$0.83(\pm 30\%)$ (SK2)

Table 7-1: Efficiency and background numbers used for sensitivity calculations for a water Cherenkov detector. The numbers are based on published or preliminary Super-Kamiokande studies. The systematic uncertainties are included for reference but play no role in the sensitivity calculation.

### 7.3 Proton decay to $e^+\pi^0$

For the decay of a free proton, the momentum should be zero within the limits of detector resolution; for the decay of a bound proton, the momentum is smeared up to the Fermi level (225 MeV/ $c$  in  $^{16}\text{O}$ ). No muon-decay electron should be present, a requirement that eliminates a great deal of atmospheric neutrino background. Compared to other possible nucleon decay modes, this is a very clean signature.

For  $e^+\pi^0$ , the detection efficiency is dominated by nuclear absorption when the proton decays in  $^{16}\text{O}$ , with 37% of the pions being absorbed or undergoing charge exchange; in either case the signature is lost. Decay of the free proton is detected efficiently, however, with an experimental efficiency of 87%. Overall, a proton decay to  $e^+\pi^0$  in water event will pass the standard set of Super-Kamiokande cuts with an efficiency of 45%.

Figure 7-2 shows the 90% sensitivity curve for  $p \rightarrow e^+\pi^0$  plotted as a function of calendar year. The leftmost curve is that for Super-K. The first smooth section reflects the initial running period known as Super-K-I (SK1) that started in May 1996. Then there is a flat period reflecting a planned small shutdown in 2001 that was lengthened due to the PMT chain reaction accident. The subsequent smooth curve is SK2, followed by a brief shutdown, and then SK3 changing smoothly into SK4 in 2008. The Super-K official limit as of early 2011 (SK1+2+3+4) is  $1.2 \times 10^{34}$  years [2,3].

The efficiencies and background rates for the curves were taken to be identical to those for Super-K. Based on the SK2 studies of  $p \rightarrow e^+\pi^0$  [2], the efficiency and background rates for 20% photocoverage were indistinguishable from 40% photocoverage (SK1 and SK3). Therefore, we take the LBNE curves to represent configurations with either 15%-HQE or 30%-HQE.

After 10 years, a 200 kt water Cherenkov detector would have an expected background of 4 events given our assumed background rate. This has a significant impact on the 90% C.L. limit we would set, or conversely, the ability to identify one or two candidate events in

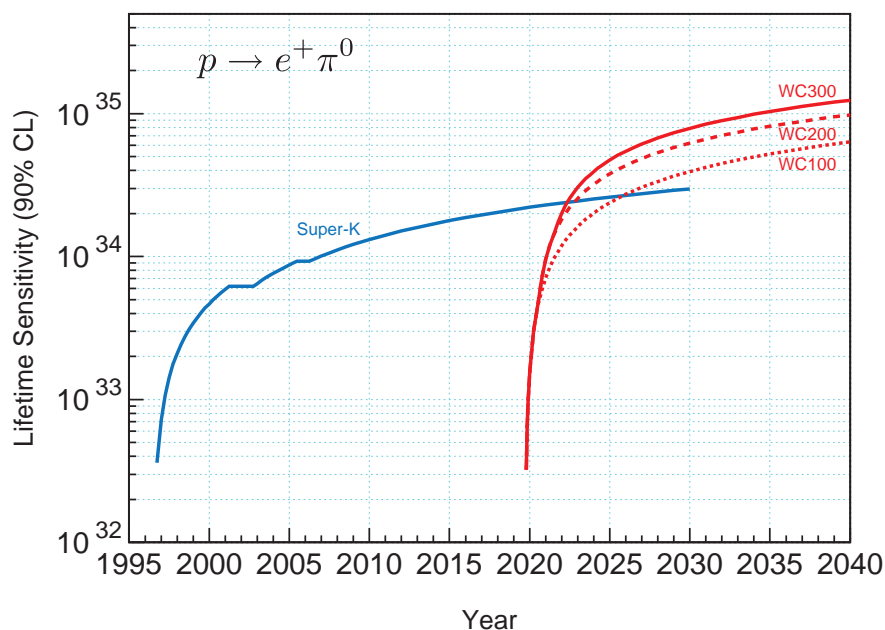


Figure 7-2: Proton decay lifetime limit for  $p \rightarrow e^+\pi^0$  as a function of time for Super-Kamiokande compared to 300 kt of water Cherenkov detector starting in 2019. The water Cherenkov detector is assumed to commission 100 kt each year for the first three years; the limits from the partial detector masses of 100 kt or 200 kt is indicated with dashed lines. All limits use the same detection efficiency of 45% and background rate of 0.2 events/100 kt-years; systematic uncertainties are not included. The limits are at the 90% C.L., calculated for a poisson process including background assuming the detected events equals the expected background.

such an exposure. It is possible that atmospheric neutrino backgrounds could be reduced in a detector with gadolinium, assuming (a) that proton decay does not eject neutrons from a  $^{16}\text{O}$  nucleus and (b) atmospheric neutrino interactions are frequently accompanied by ejected neutrons. If the background rate could be convincingly reduced by a factor of 2, from 0.2 events to 0.1 events per 100 kt-years, then a  $200 \times 10$  kt-year exposure would set a limit of  $0.8 \times 10^{35}$  years instead of  $0.6 \times 10^{35}$  years. A 300 kt detector with reduced background rates would reach the milestone of  $10^{35}$  years in 10 years running.

## 7.4 Proton decay to $\nu K^+$

Figure 7-3 shows the 90% sensitivity curve for  $p \rightarrow \nu K^+$  plotted as a function of calendar year. The leftmost curve is that for Super-K as described above. The Super-K analysis is described in several publications [49,4].

The Super-K analysis uses three methods: (i) gamma tag with  $K^+ \rightarrow \mu + \nu$ , (ii)

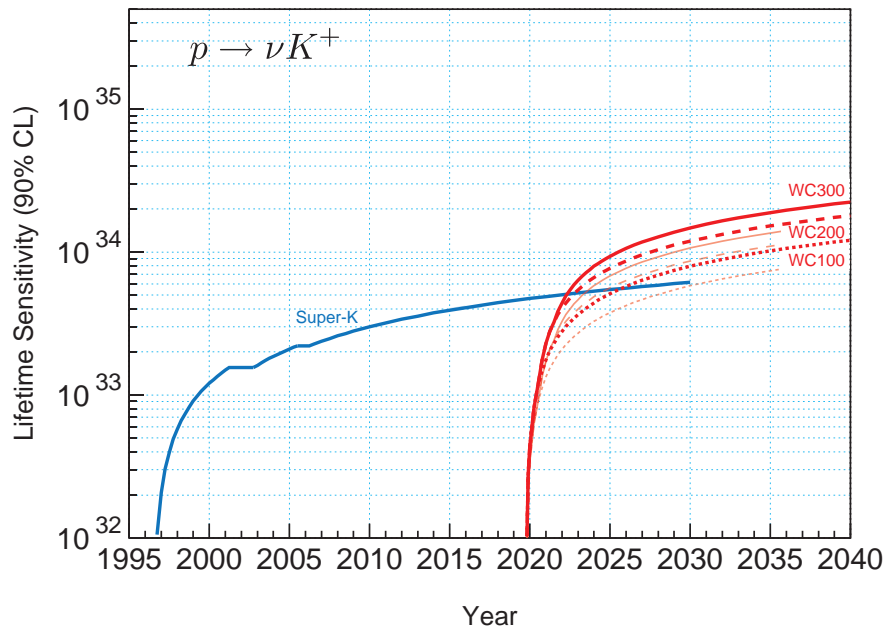


Figure 7-3: Proton decay lifetime limit for  $p \rightarrow \nu K^+$  as a function of time for Super-Kamiokande compared to 300 kt of water Cherenkov detector starting in 2019. The water Cherenkov detector is assumed to commission 100 kt each year for the first three years; the limits from the partial detector masses of 100 kt or 200 kt is indicated with dashed lines. The bold lines use the efficiency and background numbers for the SK1 analysis; the thin lines use the efficiency and background numbers for the SK2 analysis. The limits are at the 90% C.L., calculated for a poisson process including background assuming the detected events equals the expected background.

$K^+ \rightarrow \pi^+\pi^0$ , and (iii) a background limited search for a monoenergetic muon. For the purpose of the Super-K and LBNE water Cherenkov curves, only (i) and (ii) are used, because they are relatively background free. The SK1 analysis has a relatively high background rate of 0.67 events per 100 kt-year. It is likely that some re-optimization would occur for large exposures, but for the sake of argument, these numbers are assumed to not change the sensitivity much, as the most likely alteration would be some loss in efficiency in exchange for lower background. It is also possible that the LBNE detector with smaller PMTs and better timing could result in a sharper set of cuts to find the gamma ray tag. In other words, there is some hope that the LBNE detector would perform slightly better than Super-K for  $p \rightarrow \nu K^+$ , which is not likely to be true for  $e^+\pi^0$ .

As seen in Table 7-1, the performance of the Super-K analysis is markedly worse for SK2 (20% photocoverage) than SK1 (40% photocoverage). The efficiency is lower and the background rate is slightly higher. To study this difference, two sets of LBNE water Cherenkov curves are provided in Fig. 7-3, one set for each case.

After 10 years, a 200 kt water Cherenkov detector would have an expected background

of roughly 10 to 20 events depending on photocathode coverage and any possible enhancement via neutron tagging. This has a significant impact on the 90% C.L. limit we would set, or conversely, the ability to identify a small number of candidate events in such an exposure. Therefore the expected improvement in the limit over the long Super-Kamiokande run circa 2030 would be no better than roughly a factor of two.

## 8 Supernova Burst Neutrinos

### 8.1 Motivation and Scientific Impact of Future Measurements

A nearby core collapse supernova will provide a wealth of information via its neutrino signal (see [50,51] for reviews). The neutrinos are emitted in a burst of a few tens of seconds duration, with about half in the first second. Energies are in the few tens of MeV range, and luminosity is divided roughly equally between flavors. The baseline model of core collapse was confirmed by the observation of 19 neutrino events in two water Cherenkov detectors for SN1987A in the Large Magellanic Cloud, 55 kpc away [52,53]. An observed high-statistics core collapse neutrino signal will shed light on a variety of physics and astrophysics topics.

Core collapses are rare events: the expected rate is 2-3 per century in the Milky Way. The large LBNE detector(s), once constructed, may operate for decades. On this time scale, there is a significant likelihood of a supernova exploding in our galaxy. In a 20-year run of an experiment, the probability of observing a collapse event is about 40%. The detection of the neutrino burst from such an event would dramatically expand the science reach of these detectors: from measuring the neutrino mass hierarchy and  $\theta_{13}$  mixing angle, to observing the development of the explosion in the core of the star, to probing the equation of state of matter at nuclear densities, to constraining physics beyond the Standard Model. Each of these questions represents an important outstanding problem in modern physics, worthy of a separate, dedicated experiment. The possibility to target them all at once is very attractive, especially since it may come only at incremental cost to the project. The expected harvest of physics is rich enough that it is essential to prepare to collect as much information as possible when a burst happens.

In contrast to SN1987A, for which only 19 neutrinos were observed, the LBNE water Cherenkov detector would register tens of thousands of interactions from the burst. The high event rates imply that it should be possible to measure not only the time-integrated spectra, but also their second-by-second evolution. The oscillation patterns come out very different for the normal and inverted mass hierarchies. There are also several smoking gun physics signatures one can look for: for example, the expanding shock and turbulence leave a unique

imprint in the neutrino signal. The supernova signal also has a very high sensitivity to values of  $\theta_{13}$ , down to the levels inaccessible in any laboratory experiment. Additional information on oscillation parameters, free of supernova model-dependence, will be available if Earth matter effects can be observed in detectors at different locations around the Earth [54,55]. The observation of this potentially copious source of neutrinos will also allow limits on coupling to axions, large extra dimensions, and other exotic physics (*e.g.* [56,57]).

As a final note, because the neutrinos emerge promptly after core collapse, in contrast to the electromagnetic radiation which must beat its way out of the stellar envelope, an observed neutrino signal can provide a prompt supernova alert [58,59]. This will allow astronomers to find the supernova in early light turn-on stages, which may yield information about the progenitor (in turn important for understanding oscillations).

Several other experiments sensitive to supernova neutrinos will be online over the next few decades [50,60]. However one should not consider these to be “competition” for a supernova detection by LBNE: more experiments online during a supernova burst will only enhance the science yield from a supernova, and the ability to measure fluxes at different locations around the Earth will make the whole more than the sum of the parts [54].

## 8.2 Supernova Neutrino Interaction Rates

The total number of events expected scales as  $1/R^2$ , where  $R$  is the distance to the supernova (a distance of 10 kpc, which is a bit beyond the center of the Milky Way, is usually taken as a standard). In water, a few hundred events per kton within a few tens of seconds are expected at this distance; at underground sites under consideration for next-generation detectors, one expects a clean signal out to Andromeda. See Fig. 8-1.

Some of the cross-sections for interactions in water— in particular, charged current inverse beta decay  $\bar{\nu}_e + p \rightarrow e^+ + n$  (IBD) and elastic scattering (ES) of neutrinos on electrons  $\nu_{e,x} + e^- \rightarrow \nu_{e,x} + e^-$ , are known to few percent or better level. In contrast, other interactions on  $^{16}\text{O}$  nuclei have relatively large uncertainties, and cross-sections have never been measured in the few tens-of-MeV energy range.

IBD is overwhelmingly dominant in the supernova neutrino energy regime: water Cherenkov detectors are primarily sensitive to the  $\bar{\nu}_e$  component of the flux. The primary observable is the Cherenkov radiation of the IBD positron. In principle one may also exploit the delayed coincidence between the positron signal and a signal from capture of a neutron to tag the interaction, in the presence of Gd doping (see Section 11.2).

Elastic scattering, although a relatively small component of the signal, is of significance because of its directionality. IBD positrons are emitted nearly isotropically, so are of little use for pointing. In contrast, electrons are kicked in the direction of the incoming neutrino, and

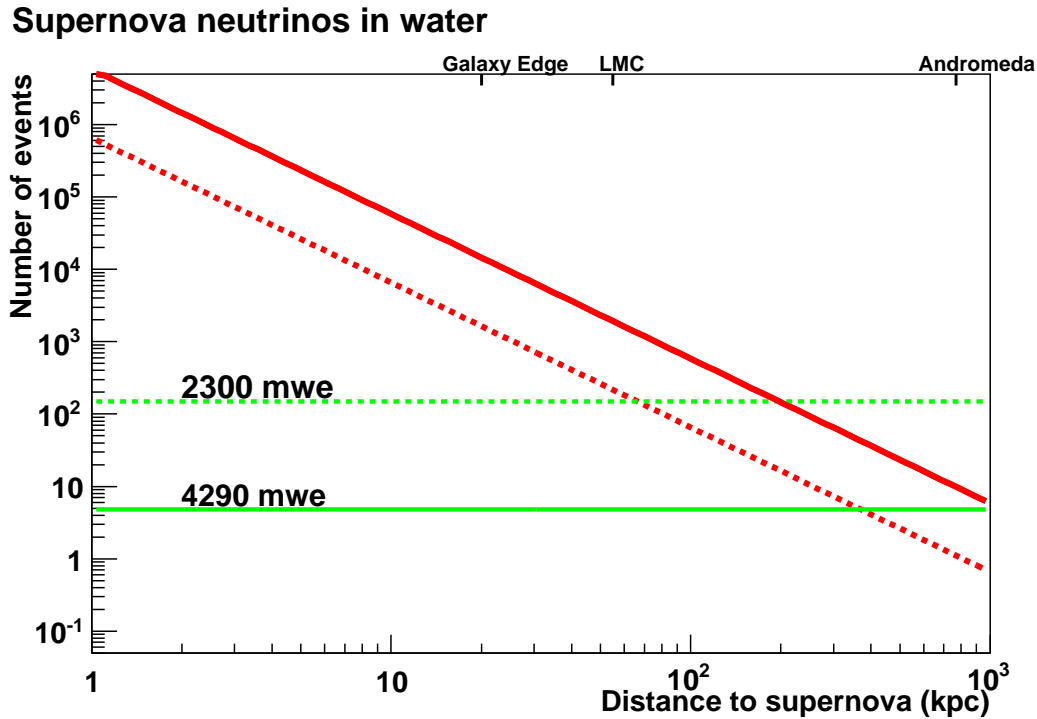


Figure 8-1: Approximate number of events detected in 30 seconds as a function of distance to the supernova for Super-K (dashed line) and a 200 kton water detector (solid line). The horizontal green lines indicate cosmic muon rates at SK depth ( $\sim 2300$  meters water equivalent (mwe)) and the Homestake mine depth (4290 mwe). (Note that cosmic muons can be effectively vetoed through several orders of magnitude.)

the Cherenkov light cone allows determination of the charged particle direction. The pointing quality scales approximately as  $\sim 25^\circ/\sqrt{N}$ ; degradation by isotropic background results in about 5 degrees pointing accuracy for a few hundred kton detector at 10 kpc [67,68]. The pointing quality can be improved somewhat with the addition of Gd to reduce the isotropic background; the angular information can be also used to select a flavor-enhanced sample (see Section 11.2). Furthermore, if the direction to the supernova is known, neutrino energy can be more precisely reconstructed for ES events.

There are also non-negligible contributions from charged current interactions on oxygen,  $\nu_e + {}^{16}\text{O} \rightarrow e^- + {}^{16}\text{F}$ ,  $\bar{\nu}_e + {}^{16}\text{O} \rightarrow e^+ + {}^{16}\text{N}$ , as well as neutral current excitations [65]. These reactions have diverse final states, including ejected nucleons and deexcitation gammas. These interactions are also asymmetric, and this asymmetry could potentially be of use in disentangling flavor components.

The predicted event rate from a supernova burst may be calculated by folding expected neutrino differential spectra with cross-sections for the relevant channels, and with detector

response. We have performed the event rate computation by using detector responses estimated with WCSim, making use of the GLOBES software [17]. We employ only the front-end rate engine part of GLOBES, and not the oscillation sensitivity part. GLOBES takes as input fluxes, cross sections, “smearing matrices” and post-smearing efficiencies. The smearing matrices incorporate both interaction product spectra and detector response.

Figure 8–2 shows the resulting differential energy spectra for the different channels. The plot on the left shows the interaction rates as a function of neutrino energy. The plot on the right shows the distribution of observed event energies in the detector. Table 8–1 shows the breakdown of detected event channels, for two different specific supernova neutrino flux models, the “Livermore” [61] and “GKVM” models [62]. We note that different flux models can give substantially different event rates. In particular, because of the thresholds of the  $^{16}\text{O}$  interactions, the rates of the CC interactions on oxygen are quite sensitive to the  $\nu_e$  and  $\bar{\nu}_e$  spectra.

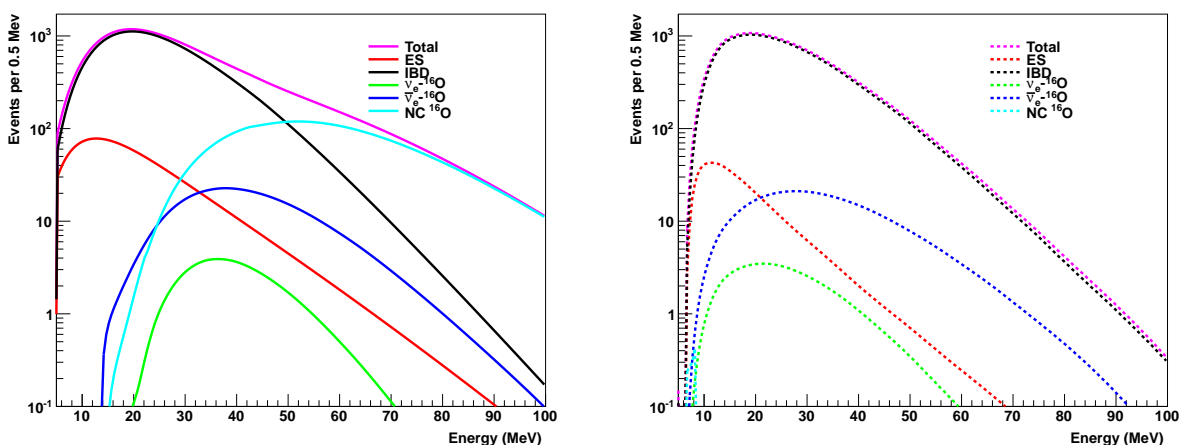


Figure 8–2: Event rates in 200 kton of water, for the Livermore model (events per 0.5 MeV). Left: interaction rates as a function of neutrino energy. Right: observed event rates as a function of detected energy.

### 8.3 Mass Hierarchy Sensitivity

There will likely be significant and observable imprints of oscillation parameters on the observed spectrum of burst supernova neutrino events. For oscillation sensitivity, ability to measure and tag the different flavor components of the spectrum is essential.

We have attempted a simple quantification of the relative sensitivity of the different single detector configurations to mass hierarchy using a flux provided by Huaiyu Duan [63],

Channel	Events, “Livermore” model	Events, “GKVM” model
$\bar{\nu}_e + p \rightarrow e^+ + n$	50272	30442
$\nu_x + e^- \rightarrow \nu_x + e^-$	1198	774
$\nu_e + {}^{16}\text{O} \rightarrow e^- + {}^{16}\text{F}$	170	748
$\bar{\nu}_e + {}^{16}\text{O} \rightarrow e^+ + {}^{16}\text{N}$	1379	968
$\nu_x + {}^{16}\text{O} \rightarrow \nu_x + {}^{16}\text{O}^*$	2	0.5
Total	53021	32932

Table 8–1: Event rates for different models in 200 kton of water.

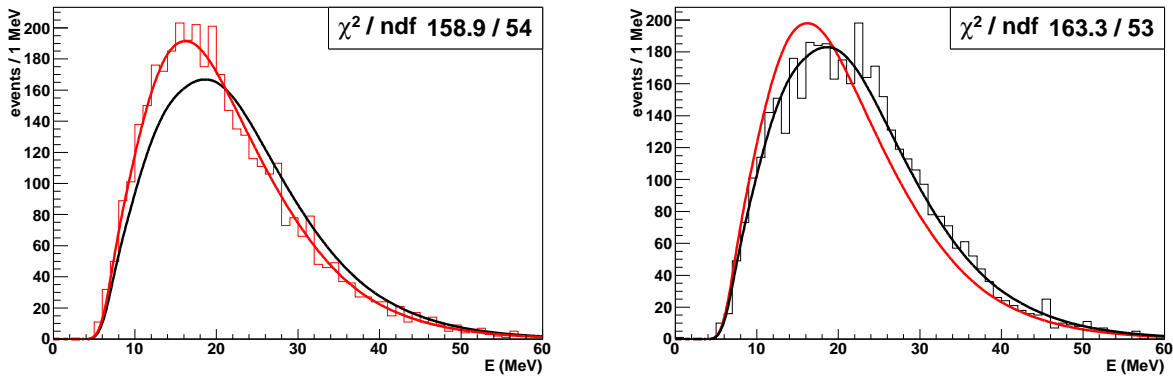


Figure 8–3: Example fits to the expected spectral shapes for normal and inverted hierarchies for the Duan model, for 4000 water events. Left plots: true hierarchy is inverted. Right plots: true hierarchy is normal. The  $\chi^2/\text{dof}$  is given for the fit to the “wrong” hierarchy.

for which there are clear differences in hierarchy for both  $\bar{\nu}_e$  and  $\nu_e$  fluxes. Because fluxes with oscillation signatures are at this time only available representing a fraction of the total flux, we cannot evaluate the full statistical sensitivity. Nevertheless we have done the following: we have determined the minimum statistics for which normal hierarchy is distinguishable from inverted hierarchy, for the Duan multi-angle spectrum [63]. Approximately 3500 water Cherenkov events are required to distinguish the hierarchy at  $3\sigma$  for this model; for a 200 kton detector, all core collapse supernovae within the galaxy will produce at least this many events. Figure 8–3 shows examples of observed spectra for the different configurations and hierarchies, for statistics near distinguishability. Although this study was done for a single model, we expect multiple signatures of oscillation physics in the full time and spectral structure of the flux.

As part of the larger LBNE physics study, we also considered LAr in combination with WC. For LAr, the sample represents a nearly-pure  $\nu_e$  sample, even in the absence of tagging using gammas. The WC sample represents a nearly-pure  $\bar{\nu}_e$  sample. Flavor-enhanced samples in WC can be obtained using neutron tagging, or by selecting ES events using the

angular distribution: see section 11.2. Although ES and non- $\bar{\nu}_e$  components can be identified with reasonable statistical significance in WC, spectral information in these samples is weak compared to that from LAr and a clean  $\nu_e$  sample from LAr could be used to help disentangle flavor components in WC. Therefore, for supernova burst physics we prefer a configuration with both WC and LAr detectors.

# 9 Atmospheric Neutrinos

## 9.1 Introduction and Physics Motivation

Atmospheric neutrinos have played a crucial role in the discovery of neutrino oscillations and the measurement of neutrino masses and mixing parameters. Atmospheric neutrinos are sensitive, at least in principle, to all of the physics remaining to be discovered in the PMNS matrix; the flux consists of neutrinos and anti-neutrinos of all flavors, and passes through significant densities of material, introducing modifications due to matter effects. The size of the earth is nearly optimal for the study of the large neutrino mass splitting, with large oscillation probabilities in the dominant channel. Three-flavor matter-enhanced atmospheric neutrino mixing is described by a rich phenomenology [99,100,101,102,103,104,105] and offers significant opportunities for discovery. In addition to the precision measurements of the dominant oscillation parameters [106,107], the Super-Kamiokande experiment has already carried out studies searching for tau appearance [108], mixing at the solar mass scale [109], three flavor oscillations [110], as well as more exotic scenarios [111,112,113].

The very high-statistics sample that will be available with the large LBNE detector can provide an important complementary measurement of the oscillation parameters as determined using neutrinos from the accelerator beam.

### 9.1.1 Confirmatory Role

Atmospheric neutrinos have the potential to play a vital role in the context of a comprehensive program to study the lepton sector because all of the physics that one might hope to examine with beam neutrinos can also be explored (albeit with reduced precision) using atmospheric neutrinos. This includes oscillations at the large  $\Delta m^2$ , tau appearance,  $\nu_\mu \rightarrow \nu_e$  mixing in the presence of a non-zero  $\theta_{13}$ , the CP-violating phase, and the study of the mass hierarchy. Because these phenomena play out over a wide range of energy and path lengths, atmospheric neutrinos are very sensitive to alternative explanations or subdominant new physics effects that predict something other than the characteristic (L/E) dependence predicted by oscillations in the presence of matter. This power has already been exploited

by Super-Kamiokande in fits that compare their data binned in terms of energy and zenith angle to a host of new physics including CPT violation [116,117], Lorentz invariance violation [118,119], non-standard interactions [120], Mass Varying Neutrinos (MaVaNs) [121], and sterile neutrinos [111,112,113]. In numerous cases the best limits on exotic scenarios come from atmospheric neutrino analyses.

The breadth of physics available with atmospheric neutrinos make them an important part of the overall physics mission of LBNE. One concrete example is the study of  $\nu_\tau$  appearance in the atmospheric neutrino flux. While a large fraction of the muon neutrinos are thought to oscillate to tau neutrinos, the overall rate of tau interactions is small due to the energy threshold for tau production. Tau events are expected at a rate of around 1 event per kiloton-year in the oscillated atmospheric flux. These events can be identified on a statistical basis in water Cherenkov detectors [108]. A recent paper estimates that with a set of simple cuts on visible energy, reconstructed zenith angle, and energy of the highest energy pion in events lacking a charged lepton, a  $4.3 \sigma$  excess over background can be identified in a 100 kt-yr exposure [122], or 6 months of running with the LBNE water Cherenkov detector. Confirmation of the appearance of tau neutrinos at the expected level in the atmospheric flux will be an important consistency check on our overall oscillation picture.

### 9.1.2 PMNS Matrix Measurements

The key observable for atmospheric neutrinos will be the data binned in (energy,zenith angle) for events separated by flavor, and ideally by neutrino/anti-neutrino. For upgoing neutrinos ( $\cos(\theta) < 0$ ), oscillations at the atmospheric mass splitting introduce large effects and matter effects introduce significant distortions of the spectrum, particularly for neutrinos which pass through the Earth's core. Mixing involving electron neutrinos is enhanced for non-zero  $\theta_{13}$  for neutrinos (anti-neutrinos) due to matter effects if the hierarchy is normal (inverted).

The two key measurements, and the data samples that would be used to study them, are:

- Octant of  $\theta_{23}$ : Upward-going, sub-GeV electron neutrinos are affected by sub-dominant oscillations at the solar mass scale. This may allow the ability to determine whether  $\theta_{23}$  is less than or greater than 45 degrees, even if  $\theta_{13}$  is zero. Recent work suggests that the effects for  $\sim$  sub-GeV ( $E < 100$  MeV) neutrinos may be as large as 10-15% [99].
- Mass hierarchy and  $\theta_{13}$ : A non-zero  $\theta_{13}$ , combined with matter effects, leads to a complicated structure of oscillation peaks for upgoing, roughly 1-10 GeV electron and muon neutrinos. Matter effects lead to an enhancement for electron neutrinos if the hierarchy is normal, and anti-neutrinos if the hierarchy is inverted.

Many of the possible signatures in the atmospheric neutrino flux appear in the few hundred MeV to few GeV energy range. Key performance characteristics for the detector include being able to distinguish  $\nu_\mu$  CC,  $\nu_e$  CC, and NC events at these energies, as well as being able to accurately determine the energy and direction of the incoming neutrino.

Atmospheric neutrinos, when combined with beam neutrinos in a global analysis, may help to resolve some degeneracies. In particular if  $\theta_{23}$  is not  $45^\circ$ , and  $\theta_{13}$  is small, the analysis of atmospheric neutrinos may contribute significantly to resolving degeneracies present in the analysis of beam data alone [123].

## 9.2 Evaluation of Physics Sensitivities

In this section we will evaluate atmospheric neutrino physics sensitivities for water Cherenkov and liquid argon detectors. We will begin by describing the key detector performance characteristics, describe the tools developed for carrying out these studies, and present results on two key measurements: the octant of  $\theta_{23}$  and resolution of the mass hierarchy.

Due to the success of the Super-Kamiokande experiment, the performance of water Cherenkov detectors for measurements of atmospheric neutrinos, and the ways in which the data are to be analyzed, are well understood.

### 9.2.1 Method and Tools

For sensitivity studies we have developed a fast, four-vector level simulation tool that performs event classification, measurement, binning, and statistical analysis. This is done with a set of software based on the MINOS atmospheric analysis framework.

The simulation proceeds in several steps:

**Event Generation:** Four-vector level events are generated using the GENIE neutrino event generator [127]. For this purpose new flux drivers were developed which implement both the Bartol [128] and FLUKA 3-d [129] flux calculations at the Soudan, MN site, which is a reasonable approximation for the geomagnetic latitude of DUSEL. Figure 9–1 shows the two inputs to the event rate calculation and event generation, the Bartol flux and the GENIE cross sections. The event rate on water varies over the solar cycle, from a minimum of 288 (275) events/kton-yr to a maximum of 331 (303) events/kton-yr as calculated using the Bartol (FLUKA) flux. Predicted event rates in liquid argon differ from these values by less than 2%.

GENIE is then used to generate large samples of interactions. These simulations include

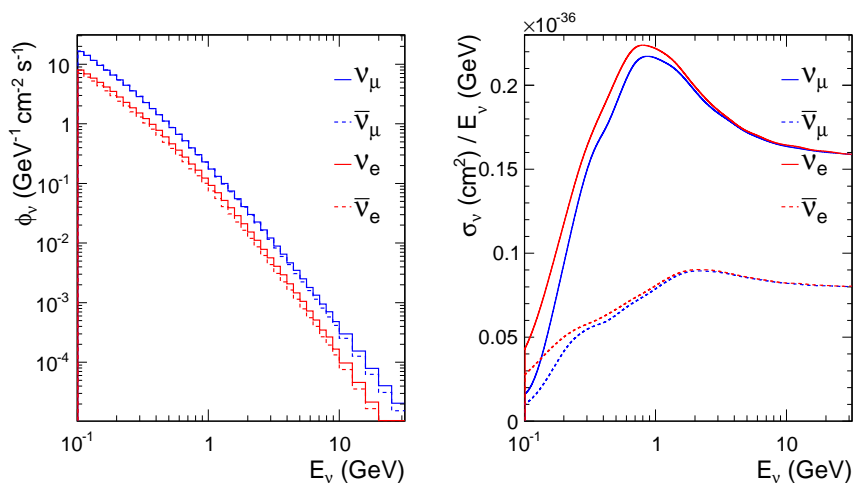


Figure 9–1: The Bartol 3d atmospheric flux (left) and the GENIE neutrino-water cross sections (right).

all known scattering mechanisms of relevance in this energy range as well as a simulation of nuclear effects including fermi motion, Pauli blocking, and intranuclear rescattering. The output of these events are a set of 4-vector for particles emerging from the struck nucleus. These can either be input to a detector simulation or to a fast parametrized simulation of detector response. Figure 9–2 shows such an event input to the WCSim detector simulation described in Section 5.2.

Pseudo-Reconstruction Events are passed through a fast parametrized ‘pseudo-reconstruction’. In atmospheric neutrino analyses events are categorized in a number of ways: containment (fully/partially contained), flavor (e-like/mu-like/NC-like), energy (sub/Multi-GeV), topology (single/multi-ring, QEL/non-QEL), and neutrino/antineutrino tag. The classification is made based on truth level characteristics, accounting for detection thresholds and misidentification via the following steps:

1. Classify containment by simulating vertex and end points for each event using a toy detector geometry. For a 100 kton fiducial mass WC detector the geometry is a cylinder with 26.5m radius and 60m height. A fiducial volume cut is then placed on the vertex (2 m) and track end positions (0.5 m) to determine if the event is fully or partially contained.
2. Simulate trigger by selecting those events containing particles above threshold (‘visible’ particles), here taken to be 50 MeV. Charged particles in are required to be above Cerenkov threshold.
3. Assign neutrino flavor to events using true  $\rightarrow$  reconstructed classification matrices, giving probabilities for different reconstructed event types. These matrices are adapted

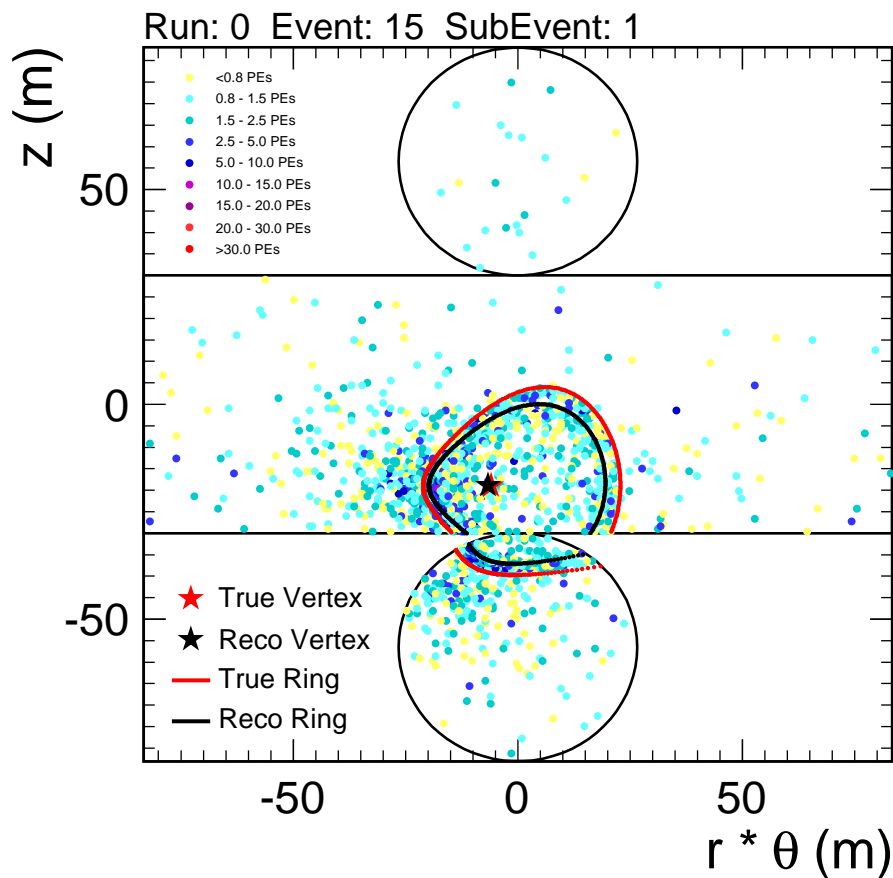


Figure 9-2: A simulated 1 GeV  $\nu_\mu$  CC interaction in a water Cherenkov detector. This event was produced using the GENIE atmospheric neutrino flux driver to produce final state four-vectors, which were converted into Nuance tracker format for input into the WCSim detector simulation and reconstruction.

from versions in the literatur [131].

4. Smear energy and angle of leptons and hadronic final states, using the resolution functions given in Table 9-1.
5. Apply minimum energy cuts of 100 MeV for selected FC and 300 MeV for PC events.

Figure 9-3 shows the simulated zenith angle distributions for the analysis categories defined above, for five years of data taking.

Sensitivity Evaluation: Binned pseudo-reconstructed data are then compared to oscillation hypotheses and relevant statistics are calculated. Three-flavor oscillation probabilities

Resolution	WC
FC Lepton	
Energy:	$2\% + 2\%/\sqrt{E}$
Angle:	$2^\circ$
PC Lepton	
Energy:	50%
Angle:	$2^\circ$
Hadronic System	
Energy:	$30\% + 30\%/\sqrt{E}$
Angle:	$45^\circ + 15^\circ/\sqrt{E}$

Table 9-1: Summary of resolution functions taken from, or tuned to, Super-Kamiokande resolution plots [134].

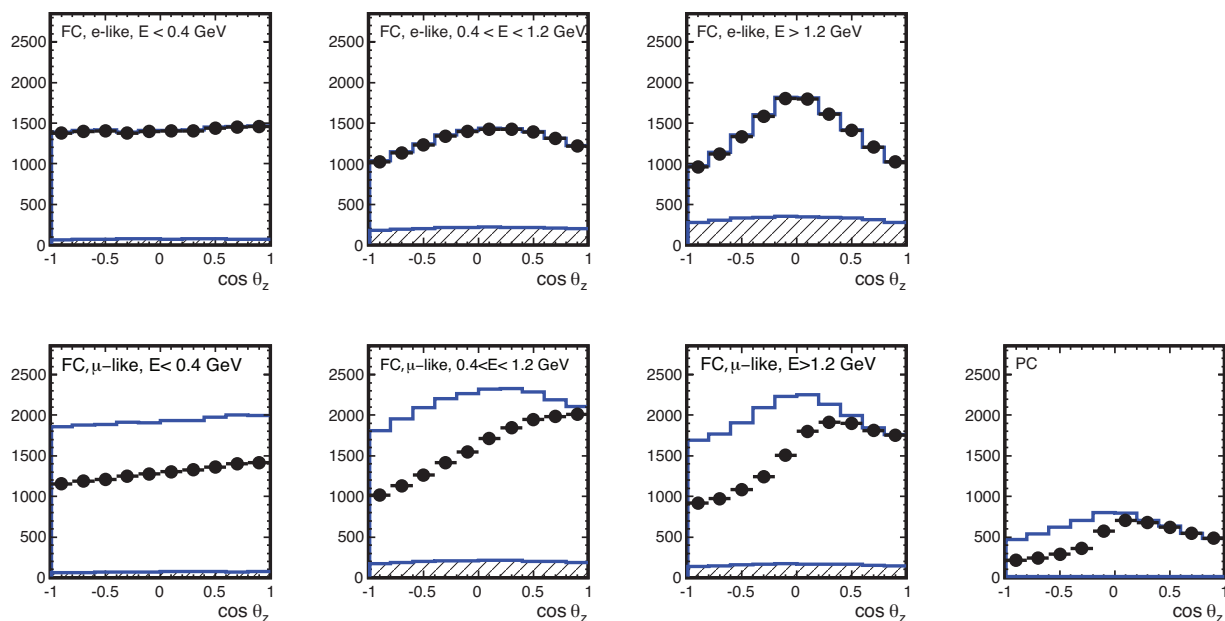


Figure 9-3: Simulated zenith angle distributions for 500 kTon-yr of atmospheric neutrino data in a water Cherenkov detector. No oscillations (solid blue), with oscillations (black), NC contribution (dashed blue).

including matter effects [135] incorporating the PREM earth model are calculated using code provided by Mark Messier [136]. Neutrino production heights as a function of energy and zenith angle are calculated using parametrizations and code developed by the MINOS and Soudan 2 experiments [137].

The effect that oscillations would have on the experimental distributions in a water Cherenkov detector are shown in Figure 9-4. The low energy ( $0 < E_\nu < 1$  GeV) sample (left

figure in each plot) is sensitive to the octant of  $\theta_{23}$  in changes in the rate of upward-going electron like events. The high energy ( $4 < E_\nu < 12$  GeV) sample is sensitive to the mass hierarchy and non-zero  $\theta_{13}$  via changes in the rate of upward-going electron-like events. In all of these plots, the default values for oscillation parameters are  $\Delta m_{32}^2 = 2.3 \times 10^{-3}$  eV<sup>2</sup>,  $\sin^2 \theta_{23} = 0.5$ ,  $\Delta m_{12}^2 = 7.5 \times 10^{-5}$  eV<sup>2</sup>,  $\sin^2 \theta_{12} = 0.31$ ,  $\sin^2 \theta_{13} = 0$ ,  $\delta_{CP} = 0$ , and normal hierarchy. The changes from these default values are shown on each plot.

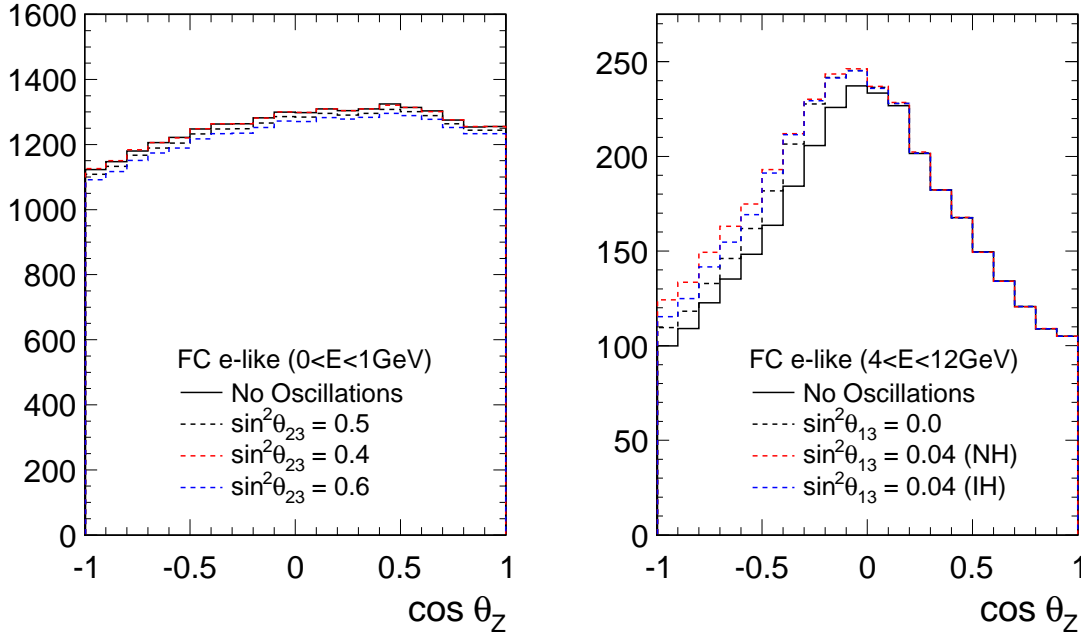


Figure 9–4: Zenith angle distributions for a low energy (left) and high energy (right) WC e-like data sample. Oscillation parameter values are given in the text.

Data in each of the analysis categories (FC/PC, e-like/mu-like/NC-like) are binned in energy and zenith angle with  $\Delta \log_{10}(E) = 0.2$  and  $\Delta \cos \theta = 0.1$ . For some input true value of the oscillation parameter, the log-likelihood difference is computed between this ‘expected’ data and data for any other set of oscillation parameters. For the sensitivities computed here, log-likelihood curves were generated in this way for a single parameter, using statistical errors only for the chosen exposure.

To validate the method as well as the misidentification matrix and resolution functions for WC, a simulation was done of the Super-Kamiokande detector geometry for a 7.68 year exposure, in order to compare with published results [138]. Even with perfect parametrizations of detector performance one would not expect complete agreement, in part because we are comparing an expected sensitivity to a result derived from actual data. This comparison does yield results in reasonable agreement, giving us confidence in our ability to accurately calculate WC sensitivities for larger detectors and exposures.

### 9.2.2 Physics Sensitivities

Figure 9-5 shows the sensitivity to the octant of  $\theta_{23}$  for 500kt-years of a water Cherenkov detector, compared to 5 years of running for a 17 kton LAr detector. In this case the likelihood difference is calculated between the value of  $\theta_{23}$  in the correct octant to that in the wrong octant. As this plot indicates, the large mass of the water Cherenkov detector outweighs the advantages in purity and directional resolution of the liquid argon detector for this measurement.

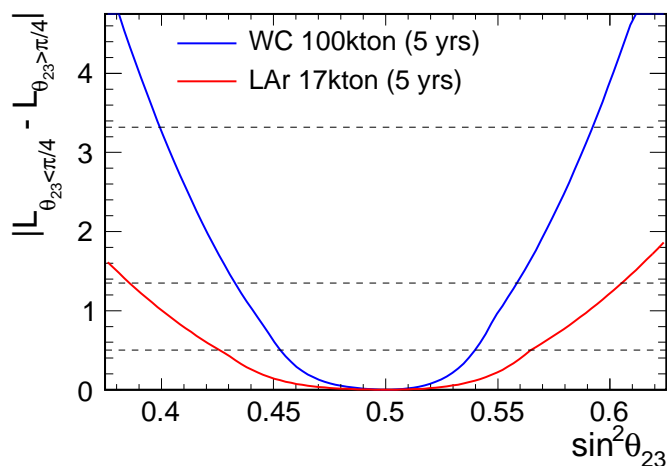


Figure 9-5: Sensitivity to the octant of  $\theta_{23}$  for five years of running with a 100 kTon fiducial mass water Cerenkov detector (blue) or a 17 kton fiducial mass liquid argon detector (red).

## 9.3 Comments on Configuration Options

Configuration options that are designed primarily to improve capabilities for lower energy neutrinos are not expected to have a significant effect on the study of atmospheric neutrinos, for example by loading the water Cherenkov detector with gadolinium.

We have included the data taken during the reduced coverage of Super-K II, and thus find that this coverage is good enough to accomplish the atmospheric neutrino physics goals. Studies [134] of the comparisons between Super-K II's reduced coverage and that of the other phases indicate that the differences are small as far as atmospheric neutrino analyses are concerned, and for the conclusions here we are considering them to be a relatively small perturbation.

## 10 Detector Enhancements

A remarkably rich physics program is made possible by locating a large water Cherenkov detector underground. We have already outlined much of this physics in the preceding sections, but an enhanced design could extend this program further. Such enhancements range from increasing the photocathode coverage in order to better separate low-energy events from backgrounds, to ‘loading’ the detector with a high-neutron capture nucleus such as gadolinium, to replacing some part of the water volume with contained (“bagged”) liquid scintillator. We briefly discuss some of the technical aspects of these enhancements below, along with possible costs, and in the next chapter discuss the long-range physics program that each might enable.

### 10.1 High Coverage/Low Threshold

The energy threshold of a water Cherenkov detector is ultimately determined by its energy resolution, which in turn depends on the number of detected PMT hits/MeV. Observing events in the energy regime of 4-5 MeV, which corresponds to the higher-energy solar neutrinos ( $^8\text{B}$  and *hep*) and to the observed energy from neutron captures on gadolinium, requires an energy resolution narrow enough to separate the events from ‘supported’ uranium and thorium chain daughters (particularly  $^{214}\text{Bi}$  and  $^{208}\text{Tl}$ ), daughters that come from ‘unsupported’ radon decays, from PMT  $\beta$ - $\gamma$  decays within the photomultiplier tube glass, and  $\gamma$ s from the rock wall. It also requires enough PMT hits to reliably reconstruct the position of an event, to impose a reasonable fiducial volume cut (getting away from the PMT radioactivity) or to correlate a neutron capture event with its primary.

We anticipate that with the nominal Super-K II level of PMT coverage discussed in the previous sections, the number of hits/MeV at low energies is roughly 3, resulting in an energy resolution of about 1 MeV near the 3 MeV endpoint of the  $^{214}\text{Bi}$  spectrum or at the energy of the primary  $\gamma$  ray from the decay of  $^{208}\text{Tl}$ . We have performed a Monte Carlo simulation-based study of the trigger rates due to radioactivity in the water, PMT glass, and surrounding rock, as a function of the concentration of the higher-radioactivity rhyolite. With a photocathode coverage like that of Super-K II, the detector trigger rates are already

above 2 kHz at an energy threshold of 7 MeV, even in optimistic scenarios. At 2 kHz, even a solar neutrino day/night measurement for which the asymmetry grows with energy (but the number of events rapidly drops) would be difficult. We therefore feel that to have a viable solar neutrino program, the PMT coverage needs to be increased, likely by at least 50% or so, to 43,500 12” HQE PMTs, for the 200 kt detector.

The energy threshold requirements for observing events associated with gadolinium capture are more strict, as half of the capture events occur below 4 MeV (where we would observe fewer than 12 hits and thus have a hard time distinguishing the capture events from accidental coincidences). On the other hand, the coincidence tag for these events means that a higher background rate can be tolerated compared to the solar neutrino measurements. Our Monte Carlo radioactivity study shows that we can get down to a threshold of 4-5 MeV with a doubling of the PMT coverage compared to the nominal Super-K II levels, with a trigger rate slightly in excess of 10 kHz—small enough compared to the  $\sim 180\mu\text{s}$  neutron capture time that accidentals should not be a major problem when position reconstruction cuts are applied.

The photomultiplier tube costs are dominated by the PMT costs themselves, and we therefore scale these costs with the number of PMTs—doubling the coverage would cost an additional \$100 M.

## 10.2 Gadolinium Loading

Adding 0.2% by mass of a soluble gadolinium compound like  $\text{GdCl}_3$  or  $\text{Gd}_2(\text{SO}_4)_3$  to water Cherenkov detectors has been suggested [86]. The neutrons produced by inverse beta reactions would thermalize in the water and then be captured on gadolinium, emitting an 8 MeV gamma cascade in the process. In coincidence with the prompt positron signal, this delayed neutron capture signal would serve to dramatically lower backgrounds from spallation and atmospheric neutrinos, at the same time allowing an enlarged energy window for detection of the relic neutrinos. Another advantage of the capture on gadolinium is that the isotropy of the  $\gamma$ -ray cascade distinguishes these events from typical Cherenkov events. As the SNO collaboration has shown [89], measures of ‘isotropy’ of the hit distribution can provide excellent discrimination between neutron capture events and single-electron or  $\gamma$ -ray Cherenkov events, even for the much less isotropic capture signal on NaCl.

As discussed in the next chapter, being able to detect neutrons in a water Cherenkov experiment opens up the possibility for tagging  $\bar{\nu}_e$  events, which is useful in observations of supernova bursts or in searches for relic supernova antineutrinos. It can also help tag antineutrino events from stopped pion beams. The SNO Collaboration has successfully tagged neutron events using capture on chlorine; the neutron ID is expected to be much better for gadolinium because of the higher isotropy of the consequent  $\gamma$  cascade.

To be able to load the detector with gadolinium, we need to ensure that all materials (PMTs and their mounting assemblies, vessel liner, cables, etc.) are compatible with gadolinium. In addition, a way of purifying Gd-loaded water, and the ability to re-capture waste is needed. Lastly, a Gd-load requires additional calibrations of the neutron capture efficiency. We expect that the total marginal cost of gadolinium loading would be  $\sim$  \$20M, but this has not had the benefit of full project-costing that the rest of the detector has had. We do not anticipate any special veto requirements for running with Gd.

### 10.2.1 Low Energy Reconstruction and Neutron Tagging

The performance of water Cherenkov detectors to neutron capture on gadolinium has been measured in Super-Kamiokande [88] and was found to be consistent with the SK detector simulation, which was used to tune WCSim for a 100 kton LBNE detector. Performance of the 200 kton version is expected to be similar, if light collection is increased to account for the longer attenuation distances.

The test source deployed in Super-Kamiokande was an AmBe source encased in a BGO crystal. The BGO allows tagging of a neutron event by observing the associated 4.4 MeV  $\gamma$ -ray created by the  $(\alpha, n)$  reaction on  $^9\text{Be}$ . Figure 10-1 shows the reconstructed effective energy spectrum from the Compton-scattered capture gamma cascade after a neutron capture on gadolinium. Although the cascade energy is around 8 MeV, the visible energy is 4.3 MeV due to below Cherenkov threshold electrons. The figure also shows the predicted spectrum from the SK detector simulation, which agrees very well with the data. The overall SK efficiency was 67%, which included a 10% loss due to capture on hydrogen.

The response of the LBNE water detector to neutron capture on gadolinium has been simulated, taking into account background gammas from measured U/Th/K concentrations in the Homestake rock, measured radioactivity of PMT glass, expected radon concentration in the water, U/Th/K levels in typical shotcrete and expected dark noise. In this study, we assumed “worst case” rock based on local measurements from core samples and the Davis cavern: 40% rhyolite and 60% amphibolite. Radon levels are assumed controlled to SK levels ( $2 \text{ mBq/m}^3$ ), and PMT glass U/Th/K is assumed the same as measured for Hamamatsu 7081 10 inch PMTs used in Double Chooz, which were standard off-the-shelf items. Dark noise is the measured dark noise of the 7081 PMTs at the expected 13 degrees C.

The basic idea is that the initial neutrino event (e.g. those from supernovae, atmospheric neutrino interactions, relic SN) would deposit enough prompt energy to be easily detected and the vertex fit. Therefore one can look for later coincident light pulses that are consistent with origin at the prompt vertex and with energy (4.3 MeV) and timing ( $\tau \sim 30 \mu\text{sec}$ ) consistent with capture on gadolinium. It is not necessary to actually trigger separately on the neutron capture events. In the simulation, a vertex resolution of 50 cm is assumed - typical of that expected for SN neutrino events.

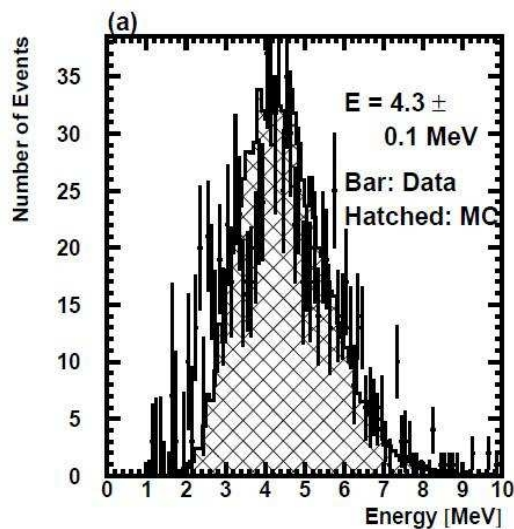


Figure 10–1: The measured visible energy spectrum of the gamma cascade from neutron capture on gadolinium in Super-Kamiokande.

We determined the rejection and the background of false neutron captures by using two sets of simulated events. The first set includes only gammas from the various radioactive materials listed above plus dark noise, and the second adds to this background sample a neutron capture near the primary event vertex. A likelihood fit is done to both sets of data, looking for events consistent with the timing and angular hit distribution of a neutron capture event, and a cut is placed on this likelihood to reject accidental backgrounds. From this we determine (a) how often the “no neutron” set is fit as having a neutron capture, and (b) how often a data set with a neutron capture is missed. Note: these likelihood cuts look at the visible energy spectrum, the time after the prompt event, and the isotropy of the in-time light (actual cascades are fairly isotropic due to multiple gammas, while background events from a single gamma are more directional). This type of likelihood variable was first used by SNO [160] to detect neutron capture, whereas the energy/timing part is original to LBNE.

Figure 10–2 shows a typical case of the stream of vertex corrected PMT hit times. There is a “floor” of dark noise with occasional gammas from the rock, PMT glass, or radon in the water (e.g. the peak at  $55 \mu\text{sec}$ ). Actual neutron capture events tend to occur early in the window and have a number of hits consistent with the 4.3 MeV effective energy. In this case the 13 hit peak at  $8 \mu\text{sec}$  is a neutron capture on gadolinium.

Figure 10–3 shows the gadolinium detection efficiency and expected background as a function of coverage for HQE PMTs. For an assumed 2m fiducial volume cut, This is moderately dependent on the shielding buffer space between the liner and black sheet of the PMT plane. Two values are shown: 50cm (left) and 80cm (right). The current design has the 80cm value. The results are presented in two ways. The top plots show background levels

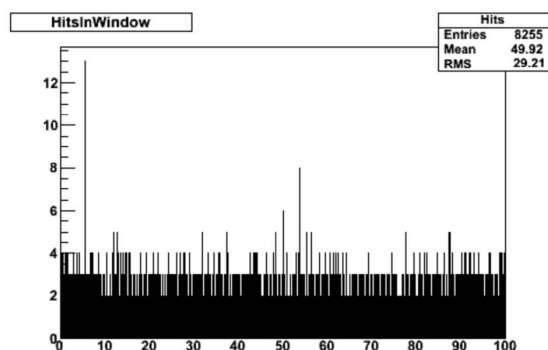


Figure 10-2: Example of a typical simulated timing stream of PMT hits for LBNE.

for a fixed tagging efficiency, which would be relevant for proton decay candidate rejection (low signal). The bottom plots show a fixed background acceptance, which would be relevant for SN event validation (high signal). As an example, if one desired 5% background at 12% coverage, then the tagging efficiency would be 54%. This would be the case for the current detector nominal coverage. If PMT coverage were doubled, efficiency would rise to 74%, which is consistent with the efficiency measured by SK. Studies done with Super-Kamiokande data have shown that the background can be as low as  $10^{-4}$ , as is discussed in the next chapter.

Note that the likelihood does not actually fit the vertex of the neutron capture event or make a cut on distance from a wall. Further work in this area will improve the preliminary results presented here and should allow background rates much less than 0.1%, which is more than sufficient for the supernova and proton decay physics. This has yet to be definitively show with hit-level simulations, but work on this is proceeding. Since doubling the HQE coverage would provide us with roughly SK light collection, there is confidence that  $< 0.1\%$  levels would certainly be achieved in that case. It should be noted that the major (13%) background after the likelihood cut is dark noise, so lowering the detector temperature might turn out to be an effective option to be optimized against just increased coverage. After dark noise the next most dominant backgrounds are gammas from shotcrete (9%) and the surrounding rock (4%). Gammas from PMT glass and radon are insignificant.

### 10.3 Scintillator Fill

Although the LBNE water Cherenkov detector will run as a water Cherenkov detector for at least a decade, it is possible that a new program of physics could be achieved by deploying a scintillator volume within the detector. As the SNO+ collaboration has shown, a scintillator volume within a water volume is a viable technical option, if a suitable containment (such as a bag like that used by KamLAND or Borexino) can be designed. Other than the scintillator process systems, the bag, and any associated safety precautions, the detector

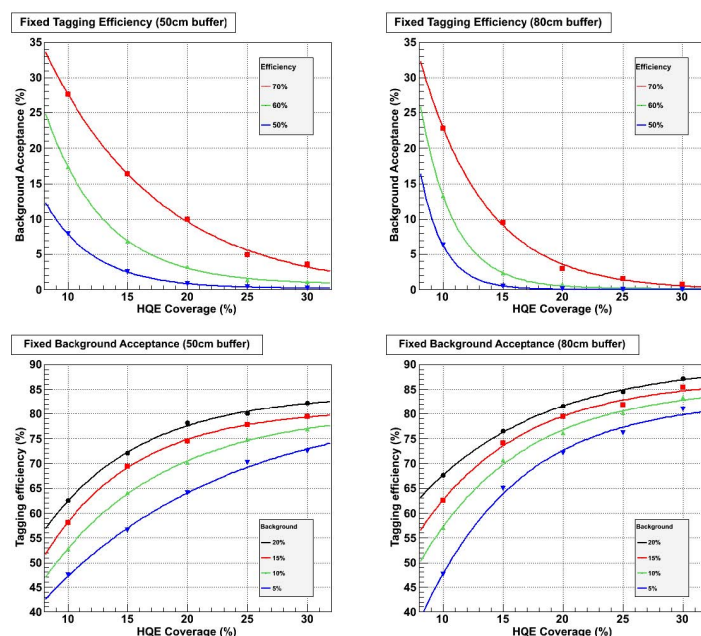


Figure 10–3: Results of gadolinium tagging study, showing hte background acceptance (top) and trigger efficiency (bottom) as a function of the photocathode coverage, assuming high quantum efficiency tubes.

would not need to be changed—the same cavity, the same PMTs, and the same electronics (perhaps with minor upgrades) could be used. The physics program with scintillator could include the kinds of geo-neutrino measurements already made by KamLAND or Borexino, the low-energy solar neutrinos that have been measured by Borexino and which will be studied by SNO+, or, given the depth and enormous shielding available in the LBNE cavity, a neutrinoless double beta-decay search like that planned for SNO+ and KamLAND-Zen. Scintillator could also provide enhanced sensitivity to the proton decay mode  $p \rightarrow K^+ \bar{\nu} u$ , as discussed in Section 11.5. A scintillator fill, were it to happen, would occur after the primary LBNE physics program has concluded—at the earliest, probably in 2030.

# 11 Physics with Enhanced Scenarios

## 11.1 High PMT Coverage and Solar Day/Night

Neutrinos from  $^8\text{B}$  decay within the Sun have been studied in great detail over the past decade by the Sudbury Neutrino Observatory (SNO) and the Super-Kamiokande Collaborations. With the additional reactor antineutrino disappearance measurements by the KamLAND collaboration, it has become clear that at energies above  $\sim 3$  MeV, solar neutrino flavor transformation is dominated by the Mikheyev-Smirnov-Wolfenstein (MSW) mechanism or ‘matter effect’. Nevertheless, some of the most interesting predictions of the MSW mechanism have remained elusive, because the mixing parameters are in a region that makes much of the phenomenology unobservable by existing detectors.

The most direct and convincing demonstration of the matter effect would be the observation of a change in the flavor content of a neutrino beam with and without intervening matter. The solar  $^8\text{B}$  neutrino beam provides us with just such a possibility: neutrinos from the Sun pass through the dense core of the Earth at night, and the difference between the forward scattering amplitude of  $\nu_e$ s and the other flavors leads to a flavor transformation similar to that which occurs within the Sun. As the beam from the Sun arrives at the Earth, it is nearly a pure  $\nu_2$  state and therefore its flavor content is only  $\sim 1/3 \nu_e$ . The flavor transformation within the Earth thus leads to a net gain in  $\nu_e$  content – the Sun ‘shines brighter’ in  $\nu_e$ s at night than during the day.

Fortunately, for the best fit values of the mixing parameters, the Day-Night  $\nu_e$  flux asymmetry is largest at energies higher than 5 MeV. These energies are accessible by a large detector with reasonable light collection coverage—roughly 1.5 times the light collection of Super-K II, when the large detector (and consequent light attenuation) is included—and no special requirements on the purity of detector materials. At the nominal coverage for LBNE, it will be very difficult to see events below about 7 MeV, because of the amount of background leakage. We thus have not investigated this scenario here.

Figure 11–1 shows the solar  $\nu_e$  survival probability as a function of energy, for both ‘day’ and ‘night’ neutrinos, for the central LMA region. For the discussion here, we will

assume that there will be an analysis cut at 7 MeV, above which radioactive backgrounds become unimportant and only spallation events remain as important backgrounds. We note that the flat shape of  $d\sigma/dT_e$  for the reaction  $\nu_e + e \rightarrow \nu_e + e$  smears out much of shape difference seen in the (neutrino energy) plot of Figure 11–1.

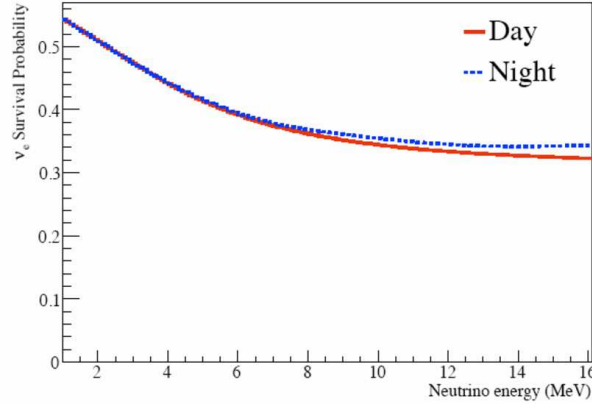


Figure 11–1: Electron neutrino survival probability as a function of energy, for day and night [159].

A measurement of the day-night asymmetry can take several forms. At its simplest, an integral asymmetry measurement can be made:

$$A = \frac{2(\phi_{\nu_e}^{night} - \phi_{\nu_e}^{day})}{\phi_{\nu_e}^{night} + \phi_{\nu_e}^{day}} \quad (11.1)$$

Currently, the measurements by the Super-Kamiokande and SNO Collaborations on this integral asymmetry have found  $A = 0.021 \pm 0.02_{-0.012}^{+0.013}$  [162] and  $A = -0.037 \pm 0.063 \pm 0.032$  [160], respectively, each within  $1\sigma$  of  $A = 0$  when both statistics and systematics are included. A more recent analysis by Super-Kamiokande [161] combining all results has reduced the uncertainties to 1.6%, and a recent analysis for SNO using the energy-dependence of the day-night survival probability [89], had a 4.0% uncertainty on the ‘constant’ (non-energy varying term) of the day-night asymmetry, still larger than the central value of 3.2%. Note that the SNO data should show a larger asymmetry because of the  $\nu_e$  ‘purity’ of the CC reaction on deuterons, compared to the neutral-current dilution of the asymmetry in the ES reaction used by Super-K and eventually by LBNE.

For a 200 kton water Cherenkov detector, the event rate in the detector with all efficiencies included is roughly 86 events/day, and consequently the statistical precision on this asymmetry after 10 years should be  $\sim 0.5\%$ , depending on the achievable analysis energy threshold and the size of systematic uncertainties. For the current best fit LMA parameters,

the integral asymmetry is expected to be near 0.02. More sophisticated analyses, involving fits to the energy and zenith-angle dependent survival probabilities, have already provided noticeably better measurements of the asymmetries in both Super-Kamiokande and SNO, and could be applied in a larger detector as well.

## 11.2 Gadolinium and Supernova Bursts

The addition of Gd to a water detector will not substantially change supernova burst event rates, but will enhance ability to determine the flavor composition of an observed signal by allowing tagging of IBD events (although note that interactions on  $^{16}\text{O}$  may produce ejected neutrons as well). To get some general idea of the value of neutron tagging of  $\bar{\nu}_e$  we performed a simple study: we looked at flavor composition for tagged and untagged events. We assume that 67% of the true IBD events will be tagged; we also assume that no events without a neutron will be falsely tagged as having a neutron (the false tagging rate should be  $\sim 10^{-4}$  according to reference [87]). We also take into account CC and NC reactions of neutrinos on  $^{16}\text{O}$ , for which some final states have neutrons; to estimate this contribution we use tables II, III and IV from reference [65]. Figure 11–2 shows the contributions of the different interaction channels for tagged and untagged events, for the GKVM flux. The neutron-tagged event rate is a nearly-pure IBD sample. The untagged event rate has contributions from elastic scattering (ES), and from CC and NC interactions on  $^{16}\text{O}$ , but is dominated by untagged IBD.

We point out that the SNO collaboration did very successful neutron tagging in their antineutrino searches, using neutron captures on chlorine. Studies many years ago by SNO also showed that gadolinium captures are easier to tag because the event isotropy—due to the higher-multiplicity of the  $\gamma$  cascade—was much higher than for chlorine.

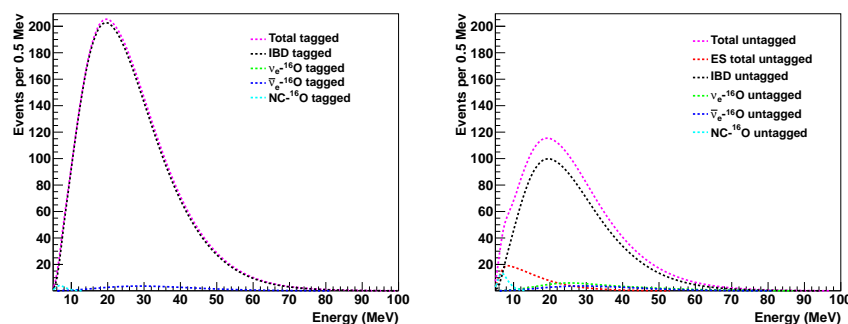


Figure 11–2: Total events in 100 kton of water showing contributions from the different interaction channels, for neutron-tagged (left) and untagged (right) events.

Figure 11–3 shows the contributions of the different neutrino flavors for tagged and untagged events. The tagged sample is nearly pure  $\bar{\nu}_e$ . The untagged sample has contributions

from other flavors, and large contamination from untagged IBD  $\bar{\nu}_e$ .

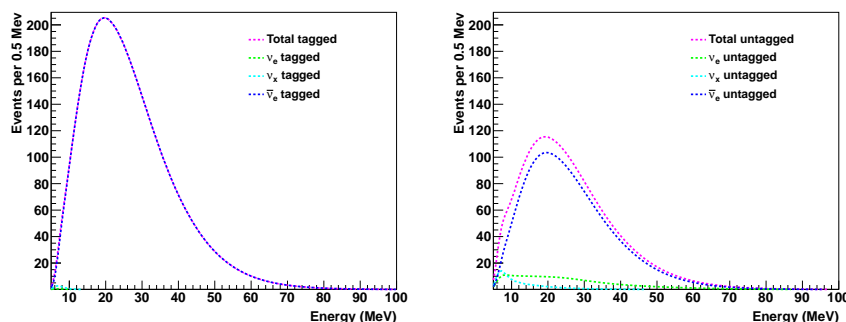


Figure 11–3: Total events in 100 kton of water showing contributions from the different flavors, for neutron-tagged (left) and untagged (right).

As noted earlier, neutron-tagging will also improve the quality of information obtained from ES events (pointing and flavor content) by suppression of isotropic IBD background.

As briefly mentioned in Section 8, the additional  $\nu_e$  flux information from LAr or another  $\nu_e$ -sensitive detector would allow disentangling of all flavor components of the flux, which will be crucial for learning about oscillation parameters from the supernova signal.

### 11.3 Gadolinium and Relic Supernova Neutrinos

Galactic supernovas are relatively rare, occurring somewhere between once and four times a century (Section 8.1). However, while nearby supernovas are rare, supernovas themselves are not—there are tens of thousands of neutrino-producing explosions every hour in the universe as a whole.

All of the neutrinos which have been emitted by every supernova since the onset of stellar formation suffuse the universe. These supernova relic neutrinos [SRN], also known as the diffuse supernova neutrino background [DSNB], have not yet been observed. However, with the appropriate technology—a very large water Cherenkov detector with good PMT coverage and gadolinium loading—the relic neutrinos can play a unique and powerful role in the physics output that can be expected from LBNE.

In particular, such a physics program could yield

- Understanding supernovas, central to understanding many aspects of the present physical universe, requires the detection of their neutrino emissions. More supernova neutrino data is strongly needed, but galactic supernova explosions are rare; the SRN will provide a continuous stream of input to theoretical and computational models.

- The shape of the SRN spectrum will provide a test of the uniformity of neutrino emissions in core-collapse supernovas, determining both the total and average neutrino energy emitted.
- Was SN1987A a “normal” explosion or not? The sparse, 23-year-old data concerning a single neutrino burst cannot say, but the SRN data can.
- How common are optically dark explosions? No one knows. Comparing the SRN rate with optical data of distant supernovas can tell us, and is probably the only way to get this information.

The only significant competition for relic antineutrino discovery comes from the Super-Kamiokande experiment. As a light water Cherenkov detector, Super-K’s sensitivity to the SRN is strictly to antineutrinos, through the inverse beta reaction,  $\bar{\nu}_e + p \rightarrow e^+ + n$ .

The most stringent limit on the relic neutrino flux comes from the SNO experiment, which observed  $\nu_e$ s through the charged-current reaction on deuterons,  $\nu_e + d \rightarrow e^- + p + p$ . The SNO analysis was limited not by spallation backgrounds but by the tail of the  $^8\text{B}$  and hep solar neutrino spectrum from charged-current reactions. The SNO limit, in the energy range  $21 \text{ MeV} < T_\nu < 35 \text{ MeV}$ , is  $< 70 \text{ cm}^{-2}\text{s}^{-1}$ . It is unlikely that LBNE or any another water Cherenkov detector will be able to repeat such a measurement, without a nucleus with a high charged-current cross section for  $\nu_e$ s.

Super-Kamiokande currently has the world’s most stringent upper limits on the relic antineutrino flux, published in 2003:  $< 1.2 \bar{\nu}_e \text{ cm}^{-2} \text{ s}^{-1}$  for  $E_\nu > 19.3 \text{ MeV}$ , based on 92 kt-years of data. The measurement is limited by spallation backgrounds. The limit is close to many predictions for the expected flux, but after eight more years of Super-K data-taking and intensive efforts to improve the relic analysis, it now appears unlikely that any existing, unmodified detector will be able to make this discovery.

Fifteen years from now, Super-K will have only roughly doubled its present (as yet largely unpublished) statistics. In the useful energy range shown on the left in Fig. 11–4 one expects between 0.25 and 2.8 signal events per year depending on the model [78,79,82,85], as compared to a measured 14 background events. In the most optimistic models, Super-K could have a  $3.3\sigma$  effect, but in the more pessimistic models, then, data taking periods of many decades would be required to see this kind of significance.

Photon detection is critical to this search, even in the absence of neutron capture with dissolved gadolinium. The right panel of Figure 11–4 shows the data for the reduced ( $\sim 15\%$ ) coverage Super-K II data set, compared to that for the 40% coverage in SK-I. The figure shows how much lower quality this data set was for the SK–II phase relic search as compared to the SK–I data. Due to impaired energy resolution, spallation events with true energies below 19 MeV can be seen leaking into the signal region, reflected in the poorer upper limit on the SRN flux:  $< 3.7 \bar{\nu}_e \text{ cm}^{-2} \text{ s}^{-1}$  for  $E_\nu > 19.3 \text{ MeV}$ .

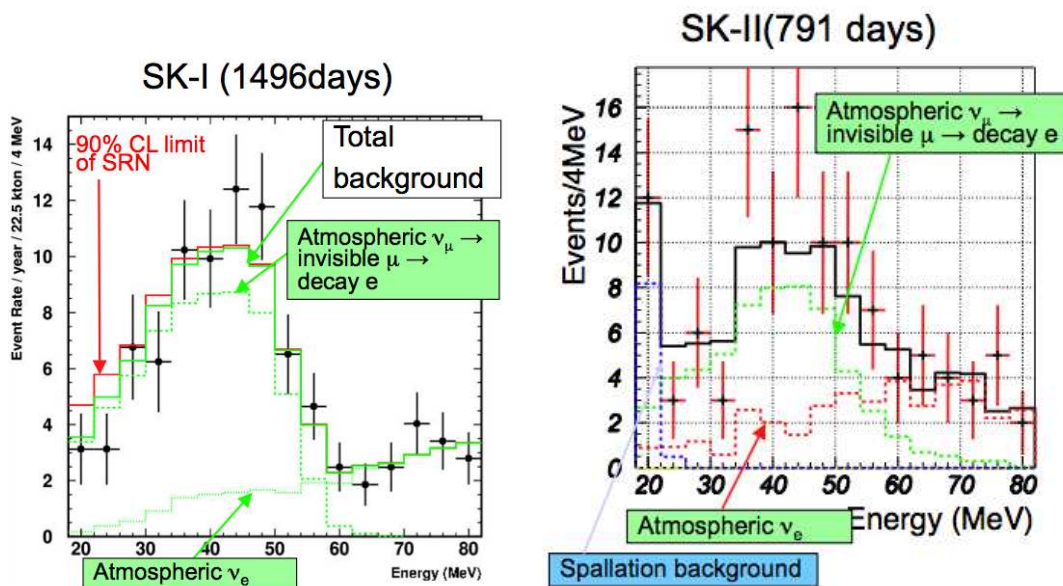


Figure 11-4: (Left) The data (points) from the 2003 Super-Kamiokande relic search. The dashed histogram peak centered around 42 MeV is that expected from decays of sub-Cherenkov muons into electrons, while the dotted line slanting down from right to left is that expected to be produced by atmospheric electron neutrinos and antineutrinos. The (green) lower solid line is the sum of these two backgrounds, while the (red) upper solid line represents the 90% upper limit on potential excess caused by the relic neutrinos. (Right) The Super-Kamiokande-II relic search. The reduced photocathode coverage of SK-II (19% vs. SK-I's 40%) and shorter running time makes this a much less useful data set than that seen on the left.

Moving from Kamioka to Homestake means that there will be about a factor of 15 less spallation, but a factor of 1.5 more atmospheric neutrinos (see Wurm et al). This will serve to make the baseline configuration's performance very similar to Super-K-I's. The spallation leakage in Fig. 11-4 will be nearly eliminated, but the backgrounds per unit volume seen in Fig. 11-4 are increased by 50%.

Doubling the number of PMTs, to 58,000 12" HQE PMTs, combined with the lower expected spallation rates at the deep site in the Homestake mine, mean that the energy window for a relic search can be extended 2.5 MeV below that used in SK-I and shown in Fig. 11-4. The higher atmospheric backgrounds are nonetheless troublesome. The enlarged energy window means that we should expect 214 background events per year in 200 kt, while at the same time increasing the expected relic flux by a factor of 1.4, making the predicted range of relic events per year fall between 3 and 35. In the best case, a 3.0- $\sigma$  discovery level would take 2.0 years of running at 80% livetime, but at the bottom of the predicted SRN range, getting to 3.0- $\sigma$  would take two and a half centuries of data.

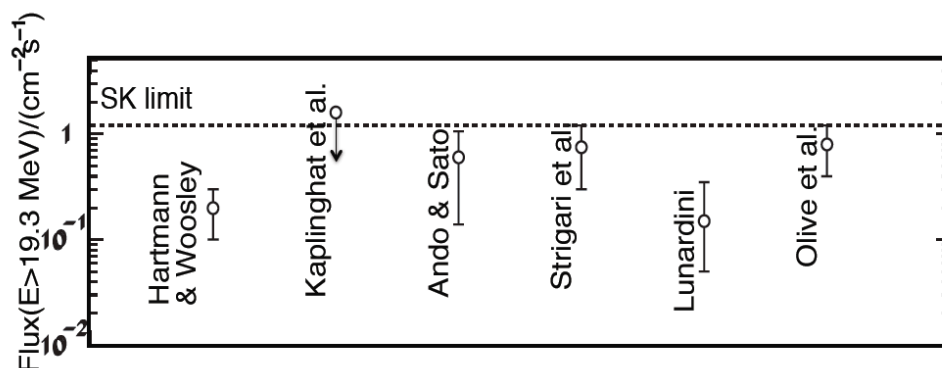


Figure 11–5: Super–K relic flux limit from 2003 compared with some theoretically predicted ranges.

Inspired by the 2003 Super–K SRN limit, adding 0.2% by mass of a soluble gadolinium compound like  $\text{GdCl}_3$  or  $\text{Gd}_2(\text{SO}_4)_3$  to water Cherenkov detectors has been suggested [86]. The neutrons produced by inverse beta reactions would thermalize in the water and then be captured on gadolinium, emitting an 8 MeV gamma cascade in the process. In coincidence with the prompt position signal, this delayed neutron capture signal would serve to dramatically lower backgrounds from spallation and atmospheric neutrinos, at the same time allowing an enlarged energy window for detection of the relic neutrinos. Figure 11–7 shows the expected signals in a gadolinium-loaded Super–K. Such a 22.5 kt detector would expect to see between 1 and 5.6 relic events a year, with about 4 background events.

The coincident detection made possible by gadolinium greatly reduces backgrounds from spallation, which is rarely accompanied by a neutron within the expected timing window [90]. This allows the SRN window to be opened all the way down to the irreducible wall formed by the antineutrinos from nuclear power reactors around the United States. Note that, primarily due to the remoteness of its South Dakota location, this reactor flux is a factor of 24 times lower in Homestake than it is in Kamioka [91]. An energy window for LBNE down to 11.3 MeV means that we would expect between 9 and 50 SRN events per year in 200 kilotons of Gd-loaded detector. The coincident technique reduces the atmospheric neutrino background by about a factor of five, and so we would expect 43 background events a year across the entire energy spectrum, with 87% of this background in the bins above 19 MeV. For the most favorable models of the relic flux, a 3.0- $\sigma$  signal could be observed in just 0.19 years (71 days) of running at 80% livetime. Even in the most pessimistic case it would still only take LBNE 6.0 years to reach the 3.0- $\sigma$  level.

In addition to observing a relic supernova signal, this enhanced configuration would be able to extract spectral information in addition to a simple flux measurement. The spectrum is a necessary input for the supernova modelers as it encodes the total neutrino energy and the average neutrino energy of bursts. In concert with astronomical observations it also provides

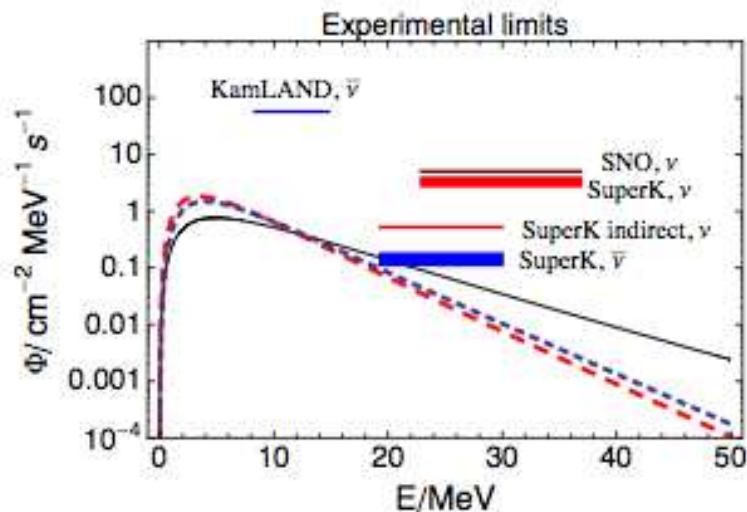


Figure 11-6: Experimental SRN limits are approaching theoretical curves. The Super-K  $\nu_e$  lines have been theoretically extracted based on the measured  $\bar{\nu}_e$  results.

a way to determine the rate of invisible explosions. On the other hand, a non-observation could indicate the existence of new physics, such as neutrino decay.

From Table 11-1 one can see that if the actual relic flux in the universe is at the high end of predictions we could observe the relic flux with any configuration. However, it should be noted that if the flux is very high then a long-running Super-K could make the discovery before LBNE is fully operational. This risk is even greater if the initial LBNE configuration has modest SRN sensitivity, extending the time needed for discovery.

Therefore, the best option for timely supernova relic neutrino flux discovery requires

Reference Configuration Number	Expected Annual SRN Signal (events/year)	Expected Annual Background (events/year)	Years of LBNE Data Needed for a 3.0- $\sigma$ Signal Assuming Maximum SRN Flux	Years of LBNE Data Needed for a 3.0- $\sigma$ Signal Assuming Minimum SRN Flux
Baseline	2 – 27	187	2.9	526
+ PMTs	3 – 35	214	2.0	268
+ PMTs + Gd	9 – 50	43	0.19	1.3

Table 11-1: Summary of sensitivities to detecting the supernova relic neutrino flux for different possible LBNE water Cherenkov detector configurations.

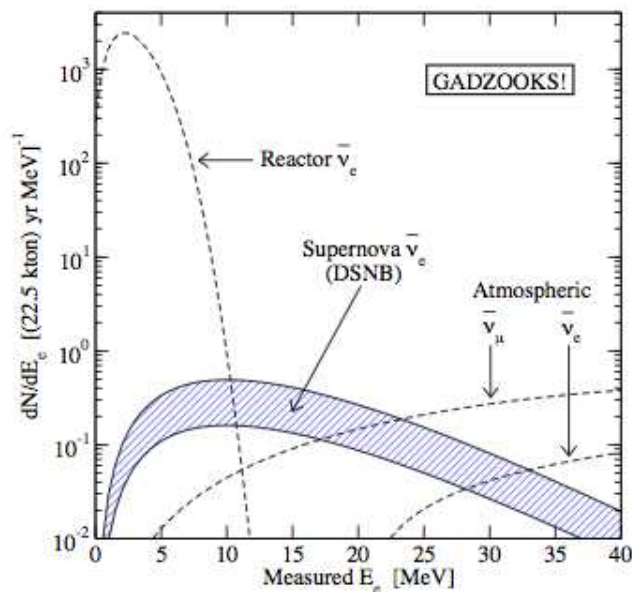


Figure 11-7: Expected spectrum of positrons seen in coincidence with neutron capture signals in a gadolinium-loaded Super-Kamiokande detector. The band shows the theoretical range of predictions for the diffuse supernova neutrino background (relic) flux. GADZOOKS! stands for Gadolinium Antineutrino Detector Zealously Outperforming Old Kamiokande, Super!.

increased PMT density and gadolinium loading. No matter where in the range of model predictions the true SRN flux lies, this configuration would need no more than a year and a half, and in most cases much less, to make a  $3.0\text{-}\sigma$  discovery. Furthermore, only this configuration will allow us to extract useful physics data in the form of spectral information.

## 11.4 DAE $\delta$ ALUS

The DAE $\delta$ ALUS (Decay At rest Experiment for  $\delta_{CP}$  studies At the Laboratory for Underground Science) proposal [1] describes a complementary approach to the LBNE science goal to measure CP violation in the neutrino sector. Where LBNE has a fixed source of neutrinos at Fermilab, and near and far detectors between which neutrino oscillations are measured, DAE $\delta$ ALUS uses an ensemble of near (1.5 km), mid (8 km) and far (20 km) cyclotrons on the surface to produce neutrinos from pion decay at rest that are detected in the LBNE Water Cherenkov detector at DUSEL (see Figure 11–8). Timing between the accelerator beam batches allows the experiment to determine the neutrino source among the near, mid and far cyclotrons.

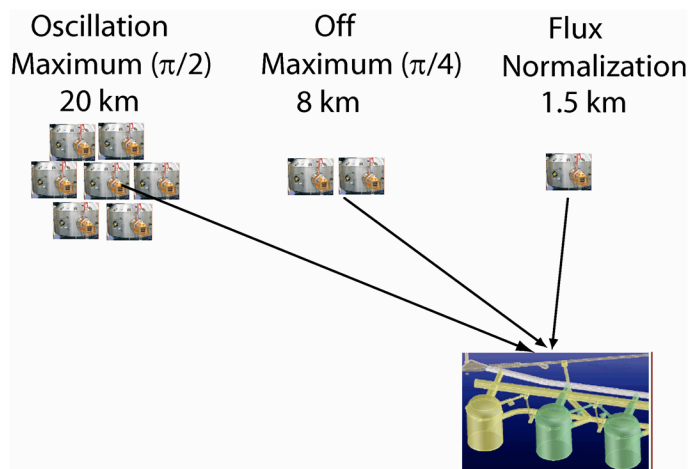


Figure 11–8: Schematic diagram showing the relationship of the LBNE water Cherenkov detectors to three complexes of cyclotrons at 1.5 km, 8 km and 20 km. The oscillation maximum refers to a  $\bar{\nu}_\mu$  energy of 40 MeV. The flux is determined from the near accelerator on the surface at 1.5 km from the detector. In this cartoon, the mid and far neutrino flux is increased by adding accelerators, where each cyclotron drawn indicates  $\sim 1$  MW of beam power. The actual experiment would be phased, and the ultimate design would depend on cost, sensitivity and choice of cyclotron technology.

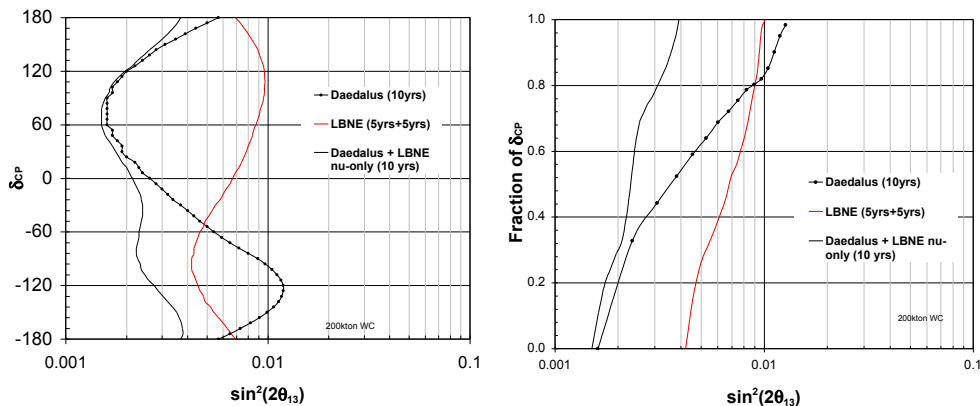
Oscillations of the  $\bar{\nu}_\mu$  to  $\bar{\nu}_e$  are detected in the water Cherenkov detector via inverse beta decay:  $\bar{\nu}_e + p \rightarrow n + e^+$ . Because  $\pi^-$  are mostly captured before decay, the fraction of  $\bar{\nu}_e$  background in the beam is less than  $\sim 4 \times 10^{-4}$ . Since the neutrino source is near the detector, there is no interference between the CP violation and matter effects. Hence, DAE $\delta$ ALUS is sensitive only to CP violation, and not the mass hierarchy. As in the case of electron anti-neutrinos from supernova, the products of the inverse beta decay for this experiment are also detected as a double delayed-coincidence signal, with the prompt positron detected through its Cherenkov radiation, and the neutron via delayed capture after  $\sim 30 \mu\text{sec}$  on Gd in the water, releasing a cascade of photons with total energy  $\sim 8$  MeV of energy of which  $\sim 4$ -5 MeV

is detected by the PMTs.

The CP measurement sensitivity of DAE $\delta$ ALUS running alone as a function of exposure and for a large water Cherenkov detector can be found in [1]. Perhaps more relevant is the combined DAE $\delta$ ALUS and LBNE sensitivities. The DAE $\delta$ ALUS results can be combined with LBNE measurements to improve the sensitivity for LBNE measurements of  $\sin^2 2\theta_{13}$  and  $\delta_{CP}$  by statistically combining the results for both neutrino and anti-neutrino running. However, this may not be the best way to optimize the combined sensitivity. Since DAE $\delta$ ALUS uses anti-neutrinos only, better sensitivity can be realized by running the LBNE experiment with a neutrino beam only. The combined  $3\sigma$  sensitivity limits of the two experiments are shown in Figure 11–9 for three different running scenarios: DAE $\delta$ ALUS alone for 10 years, LBNE for 5 years of neutrino running and 5 years of anti-neutrino running ( $3 \times 10^{21}$  POT each), and 10 years of combined running, where LBNE runs using neutrino beam only ( $6 \times 10^{21}$  POT). As can be seen, this last case has much improved sensitivity over either experiment alone, with a factor of 2–3 in the  $3\sigma$  limits on  $\sin^2 2\theta_{13} \neq 0$ , and a roughly equivalent improvement in the limit on  $\delta_{CP}$  than either experiment alone.

The neutrinos from the DAE $\delta$ ALUS targets are in the same energy range and use the same inverse beta decay detection method (water with gadolinium doping) as diffuse neutrinos from relic supernova. Whether DAE $\delta$ ALUS operations are compatible with this measurement in LBNE is under intense investigation; indeed many members of the DAE $\delta$ ALUS collaboration are also LBNE members.

Figure 11–9: Combined sensitivity limits for DAE $\delta$ ALUS and LBNE for  $\sin^2 2\theta_{13} \neq 0$  [1]. (left) Combined  $3\sigma$  sensitivity limits for DAE $\delta$ ALUS plus LBNE running, assuming 200 kt water Cherenkov fiducial mass for three running scenarios. (right) Combined  $3\sigma$  sensitivity for  $\delta_{CP}$  for DAE $\delta$ ALUS and LBNE in three different running scenarios. [Courtesy DAE $\delta$ ALUS]



Other physics topics are described in Reference [1]. The DAE $\delta$ ALUS collaboration proposes to construct the experiment in a phased approach, with Phase 0 defined as installation of a cyclotron at the near location only. Other than observing the resultant beam at LBNE,

and understanding the cyclotron operations at high intensity, the proton source can be used to detect hitherto unobserved coherent neutrino-nucleus scattering, measure  $\sin^2\theta_W$  in neutrino scattering, and search for non-standard neutrino-nucleus interactions as well as other processes. With a neutrino detector near the cyclotron, the LBNE + DAE $\delta$ ALUS collaborations will be able to study the full spectrum of neutrino physics, from the oscillation parameters of the mixing matrix through to a consistent picture that accepts or rejects the LSND result.

## 11.5 Physics in a Scintillator Fill

The existence of a large cavity deep underground would allow the possibility of a scintillator fill for the detector to address additional physics topics. Such a fill could take place after the conclusion of the beam physics program, or perhaps during an interim time between the 700 kW fill and Project X. Additionally, it might be the discovery of SUSY at the LHC might motivate an early sensitive search for SUSY-motivated proton decay at a higher priority than is currently planned.

Studies of large scintillator detectors have been carried out by the Low Energy Neutrino Astrophysics (LENA) collaboration [164] and by the HanoHano collaboration [165]. The 100-200 kton scale of the cavity considered here is comparable to the 50 kton size being considered for LENA. Currently, the largest underground monolithic scintillator detector is KamLAND [166], with a fiducial volume of only 1 kton.

Photomultiplier coverage for use in a scintillator fill can be estimated from running experiments. For reactor antineutrinos, Double Chooz has a coverage ( $\sim 12\%$ ) comparable to that being considered for our baseline design, and thus no further enhancement is likely to be needed. For proton decay sensitivity for  $p \rightarrow \bar{\nu}K^+$  no additional light collection is needed, since the  $K^+$  deposits 105 MeV/c in kinetic energy. For geoneutrinos, coverage must be similar to Borexino, at least 30%. In this case, perhaps a factor of three increase in light collection would have to be added. The development of large, inexpensive microchannel plates as envisioned by the LAPPD Project would be a crucial step towards making this affordable.

### 11.5.1 Proton Decay in a Scintillator Fill

The signal for  $p \rightarrow \bar{\nu}K^+$  in a scintillating detector is a triple coincidence signal. Initially there is a near-monoenergetic  $K^+$  of kinetic energy 105 MeV, smeared only by Fermi motion for those protons inside the nucleus. This kaon will come to rest roughly 90% of the time,

detector	background events expected	background events seen	90% c.l. limit ( $\times 10^{34} yr$ )
200 ktons WC	42	42	1.5
34 ktons LAr	0	0	5.8
200 ktons LS	1	1	19

Table 11–2: Sensitivity to  $p \rightarrow \bar{\nu}K^+$  for 200 ktons water Cherenkov, 34 ktons Liquid Argon, and 200 ktons Liquid Scintillator.

and then decay with a mean lifetime of 12.8 ns, then 64% of the time the decay is to  $\mu^+\nu_\mu$ , and for this decay muon will be monoenergetic with an energy of 152 MeV. Finally, the  $\mu^+$  will decay 100% of the time via  $\mu^+ \rightarrow e^+\nu_e\bar{\nu}_\mu$  with a mean lifetime of 2.2  $\mu s$ . Due to the fact that in scintillator detectors, the light yield is typically several hundred photoelectrons per MeV, these are all very large signals.

Including a 21% branching ratio for  $K^+ \rightarrow \pi^+\pi^0$ , published studies overall efficiency of 65% can be reached with an expected background rate of 0.1/100ktons/year. Due to the large mass and good efficiency, this option offers the highest sensitivity to this proton decay mode of any proposed technology. Table 11–2 show the sensitivity after ten years of 200 ktons of water, 34 ktons of liquid argon, and 200 ktons of liquid scintillator (assuming 0 or 1 background events are seen from an expected background of 1).

### 11.5.2 Reactor Antineutrinos

The 1 kton KamLAND detector is located in one of the highest reactor antineutrino areas of the world, with an expected rate of 160 events/year (including the effects of neutrino oscillations). Although the reactor flux at Homestake is exceptionally low (only 7% that of KamLAND) the detector size is more than 100 times larger, even with a substantial fiducial volume cut of 50% of detector mass. Therefore in one year more than 2000 reactor events would be expected from distant reactors (mostly in Illinois and Minnesota). Although not well-studied, there is the potential for a very long-baseline reactor neutrino experiment in addition to a beam experiment. Figure 11–10 shows the spectrum of reactor neutrino events expected. The periodic wiggles are due to the solar neutrino oscillation parameters.

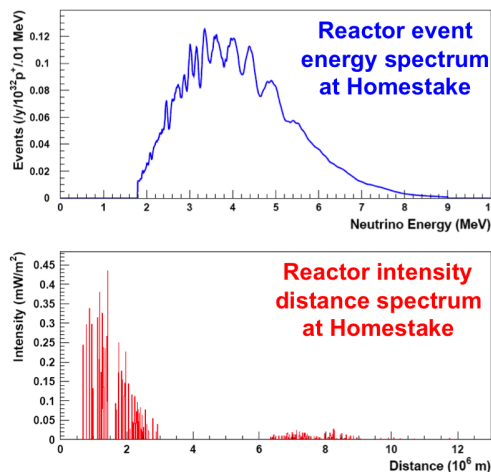


Figure 11–10: The spectrum (top) of reactor neutrino events at Homestake. A 200 kton detector would have  $170 \times 10^{32}$  free protons, so even with a substantial cut on the fiducial volume the expected rate is quite high. The distance-intensity spectrum shows that the periodic wiggles are caused by clustering of reactor distances around 500-1000 km distant.

### 11.5.3 Geoneutrinos

The average heat flux out of the earth is measured to be  $0.08 \text{ W/m}^2$ , or about 40 TW total. Due to the difficulties in measuring this average due to local variations, the uncertainty in this number is about 20%. Note that the energy impinging on the earth from the sun is  $10^4$  times larger, requiring that the geothermal outflow be measured from deep boreholes, as satellite and surface measurements are not possible.

The sources of geothermal energy are thought to be:

- radioactive decay, mostly  $^{238}\text{U}$ ,  $^{232}\text{Th}$ , and  $^{40}\text{K}$ .
- residual heat from planetary accretion
- tidal friction from the moon
- gravitational energy from iron settling to the earth's core

There is great uncertainty in the amount of heat coming from radioactive decay, anywhere from 50% to 80% of the total heat budget. This uncertainty translates into uncertainty in the earth's structure and internal chemical composition. Recent studies [91] have shown

detector	free protons ( $\times 10^{32}$ )	geoneutrino events per year	reactor events per year	$S/\sqrt{B}$
KamLAND	0.62	21.4	128	1.9
Borexino	0.18	7.33	5.36	3.2
SNO+	0.57	29.0	24.9	5.8
LBNE100	73.4	3770	661	146

Table 11–3:

that a 10% measurement of the heat from radioactive decay in the crust and mantle would lead to a differentiation between many models. It is possible to make such measurements by detecting the antineutrinos from U/Th decay (antineutrinos from  $^{40}\text{K}$  are all below the 1.8 MeV inverse beta decay threshold) at different locations on earth, thereby getting differing fractions of crust and mantle contributions.

Recently, preliminary measurements have been made by KamLAND and Borexino, but these have uncertainties of roughly 40% and 30%, respectively. This is partially due to statistics and partially due to the reactor neutrino backgrounds. At KamLAND for example, the reactor rate in the energy range of geoneutrinos is six times larger than the geoneutrino rate. Table 11–3 shows the expected geoneutrino rate, the expected reactor background rate in the energy range of geoneutrinos, and the  $S/\sqrt{B}$  for four important sites. It is clear that the DUSEL site and 200 ktons of liquid scintillator would have insignificant systematic uncertainties compared to current measurements. Systematic uncertainty is estimated to be roughly 5%. Therefore a DUSEL large scintillator detector would make a definitive measurement of crustal antineutrinos, plus make a first determination of the component from the crust (factor of two). This measurement would need roughly six months.

What would be needed in addition to scintillator is depth (e.g. KamLAND is at 2200 m.w.e and is not limited by cosmogenic backgrounds), and a radiologically clean environment. This might be achieved by a balloon of scintillator in the water, since even 100 ktons would still lead to a systematics limited result with the time of roughly a year. Studies of geoneutrinos can only be done with detectors at great depth in order to reduce the spallation background.

## Bibliography

- [1] J. Alonso, et al., “ Expression of Interest for a Novel Search for CP Violation in the Neutrino Sector: DAE $\delta$ ALUS” arXiv: 1006.026V1, 1-Jun-2010.
- [2] H. Nishino et al. [Super-Kamiokande Collaboration], Phys. Rev. Lett. 102, 141801 (2009) [arXiv:0903.0676 [hep-ex]].
- [3] <http://www-sk.icrr.u-tokyo.ac.jp/whatsnew/new-20091125-e.html>
- [4] K. Kobayashi et al. [Super-Kamiokande Collaboration], Phys. Rev. D 72, 052007 (2005) [arXiv:hep-ex/0502026].
- [5] Adam Bernstein, et al., “Report on the Depth Requirements for a Massive Detector at Homestake,” Fermilab-TM-2424-E, BNL-81896-2008-IR, LBNL-1348E, arXiv:0907.4183v2 [hep-ex] 9 Aug 2009
- [6] Golder Associates, “EVALUATION OF ALTERNATIVE SHAPES OF LARGE CAVITIES (LCS)”, September 1, 2010 Golder Report 093-81779.
- [7] Evert Hoek, representing the Large Cavity Advisory Board Memorandum: “Review of a Proposal for a 65m Diameter Cavern,” to Dr. Kevin Lesko, DUSEL project office, 7 October 2010.
- [8] J.Felde, J.Klein, C.Walter, J.Prendki, M.Smy, R.Svoboda, “Memorandum on Photomultiplier Coverage,” LBNE internal Document 3321-V2, 30-Jan-2011.
- [9] A. Beck, et al., “Fall 2010 Report from the LBNE Physics Working Group” LBNE-PWG-001 (Rel. 1.4), LBNE internal Doc. 2601-V5, 13-Mar-2011.
- [10] J. Hylen *et al.*, ”Conceptual design for the technical components of the neutrino beam for the main injector (NuMI)”, FERMILAB-TM-2018 (1997).
- [11] P. Adamson et al., Phys. Rev. D 77, 072002 (2008).
- [12] R. Brun *et al.*, CERN-DD-78-2-REV.
- [13] G. Battistoni et al., AIP Conf. Proc. 896, 31 (2007).

- [14] The 2KM Collaboration, “A Proposal to the DOE/NSF Neutrino Scientific Assessment Group”, (2005).
- [15] C. Yanagisawa, C.K. Jung, and P.T. Lee, B. Viren, arXiv:1008.1019 (2010).
- [16] F. Dufour *et al.* Phys. Rev. D 81, 093001 (2010).
- [17] P. Huber, M. Lindner, W. Winter, hep-ph/0407333 (2004). P. Huber, J. Kopp, M. Lindner, M. Rolinec, W. Winter, hep-ph/0701187 (2007).
- [18] EURONU WP6 2009 yearly report, J. Bernabeu *et al.*, arXiv:1005.3146 [hep-ph].
- [19] P. Vahle, presentation at the XXIV International Conference on Neutrino Physics and Astrophysics (Neutrino 2010) in Athens, Greece; slides available at <http://www.neutrino2010.gr/>.
- [20] Project X is a proposed high-intensity proton accelerator complex at Fermi National Lab that could provide beam for a variety of physics projects: <http://projectx.fnal.gov/>
- [21] T. Kobayashi, Neutrino 2010 presentation on the status of T2K.
- [22] J. Wilkes, presentation at XIV International Workshop on Neutrino Telescopes (Neutel11) in Venice, Italy, March 15-18, 2011. Available at <http://neutrino.pd.infn.it/Neutel2011>.
- [23] NOvA technical design report, [http://www-nova.fnal.gov/nova\\_cd2\\_review/tdr\\_oct\\_23/tdr.htm](http://www-nova.fnal.gov/nova_cd2_review/tdr_oct_23/tdr.htm)
- [24] B. Rebel, private communication.
- [25] T. Kobayashi, presentation at the XXIV International Conference on Neutrino Physics and Astrophysics (Neutrino 2010) in Athens, Greece; slides available at <http://www.neutrino2010.gr/>.  
G37, 075021 (2010).
- [26] S. Davidson, C. Pena-Garay, N. Rius, and A. Santamaria, hep-ph/0302093.
- [27] M.C. Gonzalez-Garcia, and M. Maltoni, Phys. Rept. 460, 1 (2008), arXiv:0704.1800 [hep-ph].
- [28] C. Biggio, M. Blennow, and E. Fernandez-Martinez, arXiv:0907.0097 [hep-ph].
- [29] S. Antusch, J.P. Baumann, and E. Fernandez-Martinez, arXiv:0807.1003 [hep-ph].
- [30] M.B. Gavela, D. Hernandez, T. Ota, and W. Winter, arXiv:0809.3451 [hep-ph].
- [31] W.A. Mann, D. Cherdack, W. Musial, and T. Kafka, arXiv:1006.5720 [hep-ph].
- [32] E. Akhmedov and T. Schwetz, arXiv:1007.4171 [hep-ph].

- [33] J. Kopp, P. Machado, and S. Parke, to be published soon, the talk by PANM is available from [http://www.int.washington.edu/talks/WorkShops/int\\_10\\_2b/People/Machado\\_P/Machado.pdf](http://www.int.washington.edu/talks/WorkShops/int_10_2b/People/Machado_P/Machado.pdf).
- [34] A.A. Aguilar-Arevalo *et al.*, arXiv:1007.1150 [hep-ex].
- [35] A. Friedland, Alexander and C. Lunardini Phys. Rev. D72, 053009 (2005), hep-ph/0506143.
- [36] P. Astier *et al.*, Nucl. Phys. B611,
- [37] H. Davoudiasl, H. Lee, and W. Marciano, arXiv:1102.5352
- [38] J. C. Pati and A. Salam, Phys. Rev. Lett. 31, 661 (1973).
- [39] H. Georgi and S. L. Glashow, Phys. Rev. Lett. 32, 438 (1974).
- [40] S. Dimopoulos, S. Raby and F. Wilczek, Phys. Lett. B 112, 133 (1982).
- [41] P. Langacker, Phys. Rept. 72, 185 (1981).
- [42] W. de Boer, Prog. Part. Nucl. Phys. 33, 201 (1994) [arXiv:hep-ph/9402266].
- [43] P. Nath and P. Fileviez Perez, Phys. Rept. 441, 191 (2007) [arXiv:hep-ph/0601023].
- [44] S. Raby *et al.*, arXiv:0810.4551 [hep-ph].
- [45] G. Senjanovic, AIP Conf. Proc. 1200, 131 (2010) [arXiv:0912.5375 [hep-ph]].
- [46] T. Li, D. V. Nanopoulos and J. W. Walker, arXiv:1003.2570 [hep-ph].
- [47] A. Bueno *et al.*, JHEP 0704, 041 (2007) [arXiv:hep-ph/0701101].
- [48] R. M. Barnett *et al.* [Particle Data Group], Phys. Rev. D 54, 1 (1996).
- [49] Y. Hayato *et al.* [Super-Kamiokande Collaboration], Phys. Rev. Lett. 83, 1529 (1999) [arXiv:hep-ex/9904020].
- [50] K. Scholberg, arXiv:astro-ph/0701081.
- [51] A. Dighe, arXiv:0809.2977 [hep-ph].
- [52] R. M. Bionta *et al.*, Phys. Rev. Lett. 58, 1494 (1987).
- [53] K. Hirata *et al.* [KAMIOKANDE-II Collaboration], Phys. Rev. Lett. 58, 1490 (1987).
- [54] A. Mirizzi, G. G. Raffelt and P. D. Serpico, JCAP 0605, 012 (2006) [arXiv:astro-ph/0604300].
- [55] S. Choubey, B. Dasgupta, A. Dighe and A. Mirizzi, arXiv:1008.0308 [hep-ph].

- [56] G. G. Raffelt, arXiv:astro-ph/9707268.
- [57] S. Hannestad and G. Raffelt, Phys. Rev. Lett. 87, 051301 (2001) [arXiv:hep-ph/0103201].
- [58] P. Antonioli et al., New J. Phys. 6, 114 (2004) [arXiv:astro-ph/0406214].
- [59] K. Scholberg, Astron. Nachr. 329, 337 (2008) [arXiv:0803.0531 [astro-ph]].
- [60] K. Scholberg, J. Phys. Conf. Ser. 203, 012079 (2010).
- [61] T. Totani, K. Sato, H. E. Dalhed and J. R. Wilson, Astrophys. J. 496, 216 (1998) [arXiv:astro-ph/9710203].
- [62] J. Gava, J. Kneller, C. Volpe and G. C. McLaughlin, Phys. Rev. Lett. 103, 071101 (2009) [arXiv:0902.0317 [hep-ph]].
- [63] H. Duan and A. Friedland, arXiv:1006.2359 [hep-ph].
- [64] M. T. Keil, G. G. Raffelt and H. T. Janka, Astrophys. J. 590, 971 (2003) [arXiv:astro-ph/0208035].
- [65] E. Kolbe, K. Langanke and P. Vogel, Phys. Rev. D 66, 013007 (2002).
- [66] K. Langanke, P. Vogel and E. Kolbe, Phys. Rev. Lett. 76, 2629 (1996) [arXiv:nucl-th/9511032].
- [67] J. F. Beacom and P. Vogel, Phys. Rev. D 60, 033007 (1999) [arXiv:astro-ph/9811350].
- [68] R. Tomas, D. Semikoz, G. G. Raffelt, M. Kachelriess and A. S. Dighe, Phys. Rev. D 68, 093013 (2003) [arXiv:hep-ph/0307050].
- [69] M. Ikeda, [http://www-sk.icrr.u-tokyo.ac.jp/sk/pub/m\\_ikeda\\_mron.pdf](http://www-sk.icrr.u-tokyo.ac.jp/sk/pub/m_ikeda_mron.pdf)
- [70] M. Ikeda et al. [Super-Kamiokande Collaboration], Astrophys. J. 669, 519 (2007) [arXiv:0706.2283 [astro-ph]].
- [71] I. Gil Botella and A. Rubbia, JCAP 0408, 001 (2004) [arXiv:hep-ph/0404151].
- [72] E. Kolbe, K. Langanke, G. Martinez-Pinedo and P. Vogel, J. Phys. G 29, 2569 (2003) [arXiv:nucl-th/0311022].
- [73] T. Totani, K. Sato and Y. Yoshii, Astrophys. J. 460, 303 (1996) [arXiv:astro-ph/9509130].
- [74] K. Sato, T. Totani and Y. Yoshii, Prepared for 4th SFB-375 Ringberg Workshop on Neutrino Astrophysics, Ringberg Castle, Tegernsee, Germany, 20-24 Oct 1997
- [75] D. H. Hartmann and S. E. Woosley, Astropart. Phys. 7, 137 (1997).

- [76] R. A. Malaney, *Astropart. Phys.* 7, 125 (1997) [arXiv:astro-ph/9612012].
- [77] M. Kaplinghat, G. Steigman and T. P. Walker, *Phys. Rev. D* 62, 043001 (2000) [arXiv:astro-ph/9912391].
- [78] S. Ando, J. F. Beacom and H. Yuksel, *Phys. Rev. Lett.* 95, 171101 (2005) [arXiv:astro-ph/0503321].
- [79] C. Lunardini, *Phys. Rev. D* 75, 073022 (2007) [arXiv:astro-ph/0612701].
- [80] M. Fukugita and M. Kawasaki, *Mon. Not. Roy. Astron. Soc.* 340, L7 (2003) [arXiv:astro-ph/0204376].
- [81] A. Lien, B. D. Fields and J. F. Beacom, *Phys. Rev. D* 81, 083001 (2010) [arXiv:1001.3678 [astro-ph.CO]].
- [82] J. F. Beacom, arXiv:1004.3311 [astro-ph.HE].
- [83] C. Lunardini, arXiv:1007.3252 [astro-ph.CO].
- [84] M. Malek et al. [Super-Kamiokande Collaboration], *Phys. Rev. Lett.* 90, 061101 (2003) [arXiv:hep-ex/0209028].
- [85] L. E. Strigari, M. Kaplinghat, G. Steigman and T. P. Walker, *JCAP* 0403, 007 (2004) [arXiv:astro-ph/0312346].
- [86] J. F. Beacom and M. R. Vagins, *Phys. Rev. Lett.* 93, 171101 (2004) [arXiv:hep-ph/0309300].
- [87] H. Watanabe et al. [Super-Kamiokande Collaboration], arXiv:0811.0735 [hep-ex].
- [88] A. Kibayashi and S. K. Collaboration, arXiv:0909.5528 [astro-ph.IM]. *Phys. Rev. C* 72, 055502 (2005).
- [89] B. Aharmim et al. [SNO Collaboration], *Phys. Rev. C* 81, 055504 (2010).
- [90] Y. Koshio, Ph.D thesis, University of Tokyo (1998)
- [91] <http://www.phys.hawaii.edu/~jgl/post/A~White~Paper~for~Large~Liquid~Scintillation~D.pdf>
- [92] P. Vogel and J. F. Beacom, *Phys. Rev. D* 60, 053003 (1999) [arXiv:hep-ph/9903554].
- [93] A. Strumia and F. Vissani, *Phys. Lett. B* 564, 42 (2003) [arXiv:astro-ph/0302055].
- [94] W. E. Ormand, P. M. Pizzochero, P. F. Bortignon and R. A. Broglia, *Phys. Lett. B* 345, 343 (1995) [arXiv:nucl-th/9405007].
- [95] M. Sajjad Athar and S. K. Singh, *Phys. Lett. B* 591, 69 (2004).

- [96] A. G. Cocco, A. Ereditato, G. Fiorillo, G. Mangano and V. Pettorino, JCAP 0412, 002 (2004) [arXiv:hep-ph/0408031].
- [97] <http://nucleardata.nuclear.lu.se/nucleardata/toi/nuclide.asp?iZA=30011>
- [98] A. Rubbia, J. Phys. Conf. Ser. 171, 012020 (2009) [arXiv:0908.1286 [hep-ph]].
- [99] O.L.G. Peres *et al.*, Phys. Rev. D79, 113002 (2009).
- [100] J. Bernabeu *et al.*, Nucl. Phys. B669, 255 (2003).
- [101] M.C. Gonzalez-Garcia *et al.*, Phys. Rev. D70, 093005 (2004).
- [102] O.L.G. Peres *et al.*, Phys. Lett. B456, 204 (1999).
- [103] Akhmedov *et al.*, JHEP 0806 072 (2008).
- [104] S.T. Petcov *et al.*, Nucl. Phys. B, 740 (2006).
- [105] S. Palomares-Ruiz *et al.*, Nucl. Phys. B712, 392 (2005).
- [106] Y. Ashie *et al.*, Phys. Rev. Lett 93, 101801 (2004).
- [107] Y. Ashie *et al.*, Phys.Rev. D71, 112005 (2005).
- [108] K. Abe *et al.*, Phys. Rev. Lett. 97, 171801 (2006).
- [109] R. Wendell *et al.*, arXiv:1002.3471 (hep-ex) (2010).
- [110] J. Hosaka *et al.*, Phys. Rev. D74, 032002 (2006).
- [111] K. Abe *et al.*, Phys. Rev. D77, 052001 (2008).
- [112] W. Wang, Ph. D Thesis (2007).
- [113] G. Mitsuka Ph. D Thesis (2009).
- [114] P. Adamson *et al.*, Phys. Rev. D75, 092003 (2007).
- [115] D. Indumathi *et al.*, Phys. Rev. D71, 013001 (2005).
- [116] S. Coleman and S. Glashow, Phys. Lett. B405, 249 (1997).
- [117] F. Klinkhamer and G. Volovik, Intl. Jour. of Mod. Phys. A20, 2795 (2005).
- [118] D. Colladay and V. Kostelecky, Phys. Rev. D, 116002 (1998).
- [119] Y. Grossman *et al.*, Phys. Rev. D72, 125001 (2005).
- [120] M. C. Gonzalez-Garcia *et al.*, Nucl. Phys. B573, 3 (2000).
- [121] D. Kaplan *et al.*, Phys. Rev. Lett. 93, 091801 (2004).

- [122] J. Conrad *et al.*, arXiv:1008.2984/hep-ph (2010).
- [123] P. Huber *et al.*, arXiv:0501037/hep-ph (2005).
- [124] A. Rubbia, NNN99 Proceedings, arXiv:0001052/hep-ex (2001).
- [125] M. Fechner *et al.*, Phys. Rev. D79, 112010 (2009).
- [126] S. Petcov and T. Schwetz, arXiv:0511277/hep-ph (2005).
- [127] C. Andreopoulos *et al.*, Nucl. Instrum. Meth. A614, 87 (2010).
- [128] G. Barr *et al.*, Phys. Rev. D70, 023006 (2004).
- [129] G. Battistoni *et al.*, Astropart. Phys. 19, 269 (2003).
- [130] T. Kajita, Talk at NOON2004 (Tokyo), 2004.
- [131] M. Ishitsuka, Ph. D Thesis (2004).
- [132] A. Bueno *et al.*, arXiv:0701101/hep-ph (2007).
- [133] R. Gandhi *et al.*, Phys. Rev. D78:073001 (2008).
- [134] F. Dufour, Ph. D Thesis (2009).
- [135] V. Barger *et al.*, Phys. Rev. D22, 2718 (1980).
- [136] M. Messier, private communication (2010).
- [137] M. Sanchez *et al.*, Phys. Rev. D68, 113004 (2003).
- [138] C. Ishihara, Ph. D Thesis (2010).
- [139] J.G. Learned and K. Mannheim, Ann. Rev. Nucl. Part. Sci. 50 679 (2000)
- [140] Bahcall, J., Waxmann, E., 2001, Physical Review D, 64 023002 (2001)
- [141] Gueta, *et al.*, Astropart.Phys. 20 429-455 (2004)
- [142] M. Drees and M. M. Nojiri, Phys. Rev. D 47, 376 (1993)
- [143] DeYoung, T., *et al.* et al. (IceCube Collaboration), 2008. J. of Phys. Conf. Ser. 136 022046 (2008)
- [144] V. Aynutdinov, *et al.* (BAIKAL Collaboration), Astropart.Phys.25:140-150,2006
- [145] The Antares Collaboration Internal Report CPPM-P-1999-02 (1999), arXiv:astro-ph/9907432v1
- [146] IceCube collaboration, in preparation.

- [147] R. Abbasi, *et al.*, *Astrophys.J* 701 L47-L51 (2009)
- [148] M. Ackermann, *et al.*, *Astrophys.J* 675 1014 (2008)
- [149] R. Abbasi, *et al.*, *Astrophys.J.* 710 346-359 (2010)
- [150] R. Abbasi, *et al.*, *Phys. Rev. Lett.* 102 201302 (2009), arXiv:0910.4480
- [151] S. Desai, *et al.*, *Phys.Rev.D* 70 083523 (2004)
- [152] E. Thrane, *et al.*, *Astrophys.J* 704 503-512 (2009)
- [153] M.E.C Swanson, *et al.*, *Astrophys.J* 652 206-215 (2006)
- [154] Private collaboration document DUSEL/LBNE R&D Document 994,  
<http://nwg.phy.bnl.gov/DDRD/cgi-bin/private/ShowDocument?docid=994>
- [155] E. Presani, *et al.*, *Nuclear Physics B Proceedings Supplements* 188 270-272 (2009)
- [156] H. Yuksel, S. Horiuchi, J. Beacom, S. Ando, *Phys.Rev.D* 76 123506 (2007)
- [157] B. T. Cleveland et al. *Astrophys. J.* 496: 505 (1998).
- [158] S. Fukuda et al., *Phys. Rev. Lett.* 86, 5651 (2001); Q. R. Ahmad et al., *Phys. Rev. Lett.* 87), 071301(2001).
- [159] S.R. Seibert, Ph.D thesis, University of Texas (2008)
- [160] B. Aharmim et al. [ SNO Collaboration ], *Phys. Rev. C*72, 055502 (2005).
- [161] K. Abe et al. [ Super-Kamiokande Collaboration ], [arXiv:1010.0118 [hep-ex]].
- [162] *Phys.Rev. D*69, 011104 (2004). Athens, Greece (June 2010).  
August 2010.
- [163] J. Hosaka et al. [Super-Kamiokande Collaboration], *Phys. Rev. D* 73, 112001 (2006) [arXiv:hep-ex/0508053].
- [164] Michael Wurm, et al. [LENA Collaboration], "The Physics Potential of the LENA Detector," arXiv:1004.3474v1
- [165] J. Learned, S. Dye, S. Pakvasa, "Hanohano: A Deep Ocean Anti-Neutrino Detector for Unique Neutrino Physics and Geophysics Studies," Published in the Proceedings of the Twelfth International Workshop on Neutrino Telescopes, Venice, March 2007, arXiv:0810.4975v1
- [166] S. Abe, et al., [KamLAND Collaboration] *Phys. Rev. C*, 81 025807 (2010) and the KamLAND website: <http://www.awa.tohoku.ac.jp/kamlande/?cat=3>